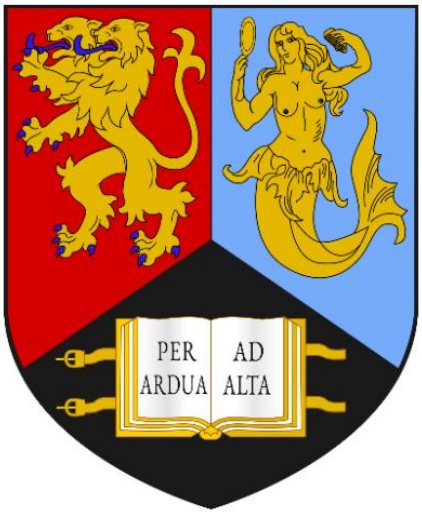

Deformation of Ti-6Al-4V Micro-pillars with Different β Phase Contents

by

Zhaoxuan Wu

A thesis submitted to University of Birmingham for the degree of

DOCTOR OF PHILOSOPHY

School of Metallurgy and Materials

College of Engineering and Physical Sciences

University of Birmingham

November 2022

Preface

The work in this thesis was carried out by Zhaoxuan Wu in School of Metallurgy and Materials, University of Birmingham (from February 2018 to November 2022), under the supervision of Prof. Yu-Lung Chiu and Dr. William Griffiths.

The present work is original, and no part of the work has been submitted for another degree at any other university. Wherever the work from other researchers has been cited or drawn on, it is acknowledged in the text and the references are listed.

Acknowledgements

I would like to greatly thank my supervisor Prof. Yu-Lung Chiu and Dr. William Griffiths for their patience, support, supervision and encourage. Prof. Yu-Lung Chiu is the one I should give a big thank for providing the chance of this project and understanding of my health situation. I thank you for the great help when meeting toughness and getting confused.

I sincerely thank Dr. Feng Wang and Dr. Minshi Wang, who share experience and knowledge with me a lot. Their supports give me great help to finish the project.

I gratefully thank Dr. Jing Wu, Dr. Bo Pang, Dr. Subash Rai, and Dr. Yang Lyv for their academic and facility support.

Many thanks to Dr. Manmath, Dr. Xinyu Lu and Dr. Ubaid Ur Rehman Ghori for their valuable discussion about experiments.

I appreciate the financial support from China Scholarship Council (CSC) and School of Metallurgy and Materials of University of Birmingham.

Lastly, my appreciation goes to my family for their support of studying and care for my health.

Abstract

Compressions of Ti-6Al-4V micro-pillars with increasing number of α/β interfaces or β fillets, orientated for prismatic <a_2>, prismatic<a_3>, pyramidal <a_3>, basal <a_1> and basal <a_3> slips have been carried out to study the role of α/β interface and its number in the plastic deformation of the alloy.

Micro-compression has been used to quantify the effect of the number of interfaces on CRSS for different slip systems. Following that, SEM was used to observe the distribution of shear bands across the pillars while TEM has been used to examine the interaction between dislocations and interfaces assisted with FIB sample preparation.

The strengthening effect of α/β interface has been considered in light of the lattice parameter mismatch τ_{misfit}, Koehler stress τ_k due to shear modulus mismatch, interface stress τ_f related to the interface energy and interface strain tensor, and w interaction τ_w that is slip system change from one phase to another. The total CRSS of micropillars was estimated by considering the contributions from α and β phases based on their volume fractions and α/β interface strengthening effect.

The interface strengthening estimated for prismatic <a_2> and <a_3> slips are 46 MPa and 18 MPa respectively, close to the experimental determined values of 49 MPa and 20 MPa. There is a significant strengthening effect of α/β interface on the CRSS values.

Slip band nucleation, formation and distribution are strongly affected by the number of α/β interfaces or β fillets. More shear bands nucleate and form, and their distribution becomes more homogeneous with increasing the number of interfaces. Likely caused by stress and strain localization as well as the dislocation pile-up at interfaces.

For the micropillars containing 2 β fillets, the CRSS of prismatic $<a_3>$ slip is 7-9% higher than that of prismatic $<a_2>$ slip.

For the pillars containing multiple (~10) β fillets, the CRSS value for basal $<a_3>$ slip, which reaches 699 MPa, is higher than that for basal $<a_1>$ and $<a_3>$ slips which are all much higher than the those reported for the micro-pillars without the α/β interface.

Pillar size effect on the CRSS value is sensitive to the number of α/β interfaces. The percentage increment of CRSS values from 10 μm to 5 μm sized pillars drops significantly from 14.2% to 3.4% with increasing the number of β fillets in the current work.

Table of contents

Chapter 1 Introduction

Ti-based alloys are well-known for their wide variety of applications, particularly in aerospace industry, such as aerostructures and engines, because of their excellent corrosion resistance and high strength-to-weight ratio, as well as a relatively good performance at high temperatures.

A large number of Ti alloys have been well developed, which are classified into three groups, namely α, β and α+β alloys. Ti-6Al-4V alloys are dual-phase, containing α phase that is hexagonal closed-packed (hcp) and β phase that is a body centred cubic (bcc). α phase is transformed from β phase while cooling down and thin layers of residual β are untransformed. This microstructure takes advantage of a high strength and a good ductility as its combination, which is commonly utilized in structural applications. The Burgers orientation relationship (OR) between two phases is approximately $\{0001\}[1, 2]\alpha \| \{110\}\beta$, $<11\bar{2}0>\alpha \| <1\bar{1}1>\beta$[3], as a consequence of the lowest interfacial energy by maximising interface coherency and minimising the interface strain. In dual-phase Ti-6Al-4V, the nucleation with α phase as the plate happens at pre-existing α or β grain boundaries[4]. Fully-lamellar-structure Ti-6Al-4V can be obtained through proper heat treatment with a low cooling rate[5].

However, it is difficult to understand the fatigue crack nucleation and predict the lifetime of components in service, because of the plasticity anisotropy [6] and also the fact that grain boundaries can significantly affect the crack initiation and propagation [7]. The initiation of small cracks is likely to happen at grain boundaries, slip bands, voids and inclusion-particle clusters [8]. The heterogeneous micro-structure, such as the introduction of interfaces, leads

to the strain localization which is the main cause for crack initiation and fatigue failure. It has reported that the difference of elastic modulus across twin boundaries (TBs) could result in strain localization and crack initiation [9]. Additionally, Brochu et al. [10] found that grain boundaries were regarded as strong barriers to the crack growth and propagation. Whereas small cracks can also grow along the shear bands. In this work, the strain localization at the α /β interface boundaries and slip bands were observed which could act as the crack initiation sites in fatigue failures.

The recent development on the plasticity of Ti alloys is focused on deformation mechanisms of α phase[11-13]. Researchers reported that slip behaviour and the corresponding gliding of dislocations are a function of crystallographic orientation, temperature and Al content. But there are relatively few studies on the deformation mechanism of dual-phase Ti alloys, due to the complexity of microstructure and the interaction between α and β phase [1, 14].

Chan et al.[15] found in dual-phase Ti-8Al-1Mo-1V alloys that the yield stress varied significantly when differing the angle between the normal to the α/β interface along the slip direction. Additionally, when the angle between the loading direction and the slip plane varied from 15° to 63°, the Schmid's law was observed to fail. Experimental investigation was completed on the effect of α/β interfaces on Ti-6Al-2Sn-4Zr-2Mo-0.1Si and Ti-5Al-2.5Sn-0.5Fe by Suri et al.[16] and Savage et al.[1], who revealed that Burgers orientation relationship (BOR) contributed to the anisotropy of slip transmission caused by the misalignment between α and β phase in basal slips a_1, a_2 and a_3 as well as the prismatic slip systems. Furthermore, Sandala and his co-workers[17] studied the morphological effect of β phase with different widths in Ti-6Al-4V and found that the plastic deformation behaviour was significantly affected by the morphology.

Ashton et al.[18] combined their experimental observation with strain gradient crystal plasticity modelling using Ti-6242 to show the presence of α/β interfaces could enhance dwell fatigue resistance compared to commercial pure (CP) α-Ti. Specifically, an increased β-phase volume fraction results in an increased strength.

In this work, to study the role of α/β interfaces in plastic deformation, we compare the plastic behaviour of single α and dual α/β colonies in Ti-6Al-4V using micropillar compression. Also, size effect is significant and will be discussed in this work. We found that strength is highly relevant to three different morphologies and sizes. More specifically, the movement of dislocations with and without interface transmission is studied to illustrate the relationship between strength and morphological microstructure. This work gives an instance to study the role of multiple α/β interfaces by fabricating and compressing micropillars of different sizes with three different morphologies at the micro scale.

In Chapter Two, the current understanding of Ti alloys is reviewed, including the slip systems, microstructures, deformation mechanisms, size effect and mechanical performance. Also, the development of micropillar fabrication and testing is presented.

The aims and objectives of this project are raised in Chapter Two.

Chapter Three covers materials used, experimental methodologies and procedures, which are heat treatment, mechanical polishing, SEM, EDS, EBSD, micropillar milling and TEM foil preparation through focused ion beams (FIB), nano-indentation and TEM.

The results of micro-mechanical properties are summarized in Chapter Four after compression with different loading directions in Ti-6Al-4V. This chapter includes stress-strain curves, the morphology of micro-pillars before and after compression, slip systems and

dislocation determination through TEM observation, shear band nucleation, formation and distribution as well as the interaction between dislocations and interfaces.

The strengthening effect of α/β-phase interface on CRSS, as well as the shear band dependence and size effect sensitivity dependence on the number α/β-interfaces, is discussed in Chapter Five.

The conclusions gained throughout this research is drawn in Chapter Six, and perspectives as well as objectives are suggested for the future work.

Chapter 2 Literature review

2.1 Basis of Ti Alloys

2.1.1 Applications

As high strength-to-weight-ratio traditional structural materials with an easy formability, good mechanical properties at high temperatures as well as a great corrosion and fatigue resistance (Figure 2.1), Ti alloys are commonly used in aerospace and medical fields, industrial and architectural applications, chemical processes and industries as well as marine and offshore applications[19]. Moreover, the operating temperature of Ti alloys is higher than that of aluminium alloys. At 150°C and above, the strength of Al alloys drops dramatically, whereas Ti alloys maintain a high strength at a temperature range of 450-500°C.[20] In addition, Ti alloys can even keep the same mechanical properties at low or super-low temperatures. Compared to stainless steel, Ti alloys have a better corrosion resistance in sea water and wet atmospheres.[21]

Resulted from their easy formability, fatigue resistance and high strength-to-weight ratio, Ti alloys can be applied to fuel tanks, gas bottles and rocket engine parts, etc. Specifically, the combination of low creep rates with a high strength at high temperatures makes Ti alloys favourable for jet engine components such as compressor discs and blades. Apart from jet engines, titanium is also used for automobile engines like engine valves and springs.

Another important application of Ti alloys, usually CP titanium and Ti-6Al-4V, is their biomedical application as heart valves, bones as well as dental and joint implants, based on their corrosion and fatigue resistance, easy formability, high specific strength and non-

magnetism as a poor conductor of electricity and heat. Additionally, Ti alloys are nontoxic with a lower coefficient of thermal expansion than aluminium and steel, which contributes to their compatibility with human beings.

In the field of application of chemical processes and industries, the excellent corrosion resistance of Ti alloys to most mineral chlorides and acids makes them a good choice in many environments, like petrochemical industry, seawater and sour hydrocarbon atmospheres. In detail, CP titanium satisfies the low-stress demand, whereas Ti-6Al-4V and Ti-13Nb-12Zr satisfy the high-stress demand[19].

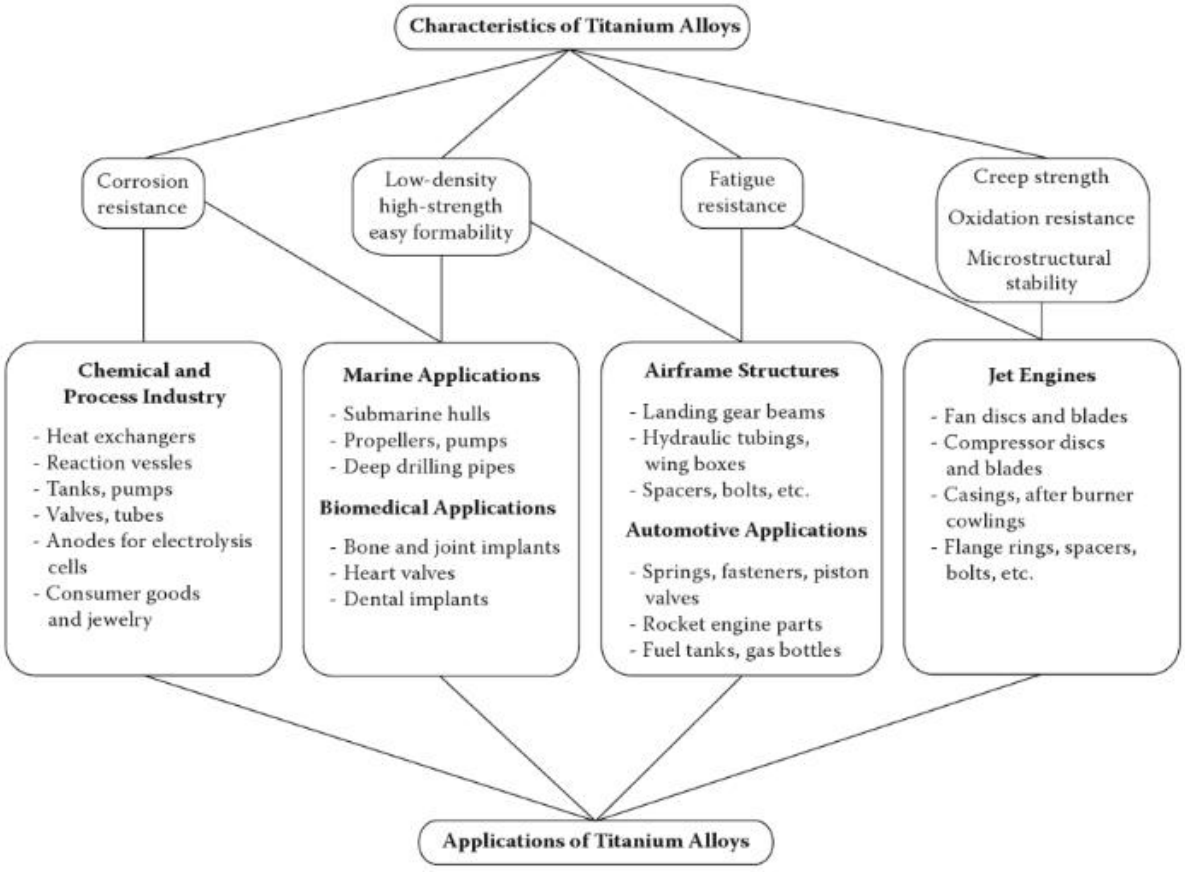

Figure 2.1 Typical application and general characteristics of Ti alloys[19].

2.1.2 Chemical Composition and Microstructure of Ti-6Al-4V

As a dual-phase alloy, α phase of Ti-6Al-4V is more stable at room temperature whereas β phase has a higher stabilization over phase transus temperature. The overall chemical composition of typical commercial Ti-6Al-4V is listed in Table 2.1:

Table 2.1 The chemical composition in weight percentage of Ti-6Al-4V alloy.[22]

Materials	Ti	Al	V	Fe	O	C	N	H
Ti-6Al-4V	Bal.	5.5-6.5	3.5-4.5	<0.25	<0.2	<0.08	<0.07	<0.0125

Al can stabilize and enrich in α phase, while elements V and Fe have a higher concentration in β phase.

There are three different microstructures of Ti-6Al-4V, greatly influencing its mechanical properties, which (Figure 2.2) are fully lamellar, fully-equiaxed and bi-modal microstructures obtained via different thermo-mechanical processing routes. This study is focused on the lamellar microstructure, which satisfies the demands including a high fracture toughness, creep resistance and fatigue crack propagation resistance.[23]

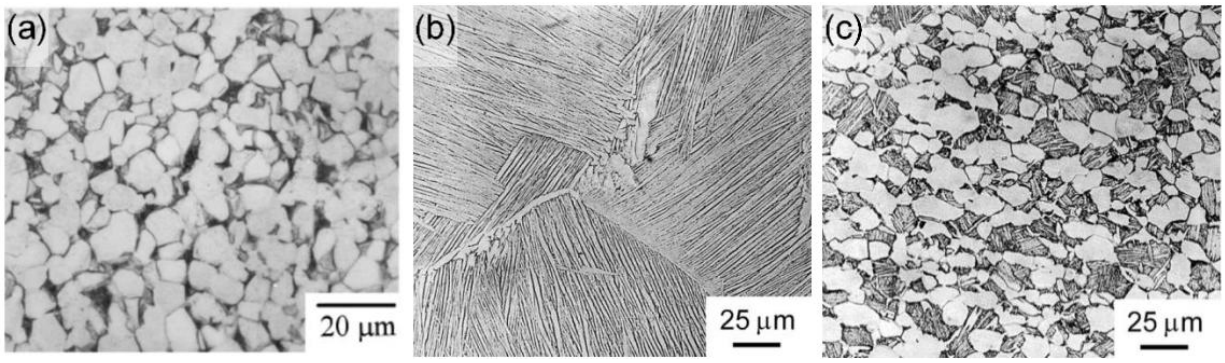

Figure 2.2 The microstructures of Ti-6Al-4V alloy for three different types: (a) fully equiaxed,[24] (b) fully lamellar[25] and (c) bi-modal microstructures[25].

α phase occurs during nucleation and growth when cooling down at the transus temperature from the parent β phase.

2.1.3 Crystallography of Ti-6Al-4V

The density of titanium alloys whose strength-to-weight ratio is much larger than that of other metal structural materials is generally around 4.51g/cm^3, only 60% of that of steel[26]. At low temperatures, titanium generally exists in α phase, while β phase exists at high temperatures. The unit cells of the α and β phase are shown in Figure 2.3. α phase has a hexagonal close-packed (hcp) structure, while β phase has a body-centred cubic (bcc) structure. α phase constitutes the majority of titanium alloys due to its better stability than β phase at room temperature, with an axial ratio c/a of 1.587, which is smaller than 1.63,[27] the ideal ratio for hexagonal close-packed structures. For pure Ti, its α/β-phase transformation temperature is 882°C, but alloying elements can greatly influence the exact phase transformation temperature of titanium alloys.[28]

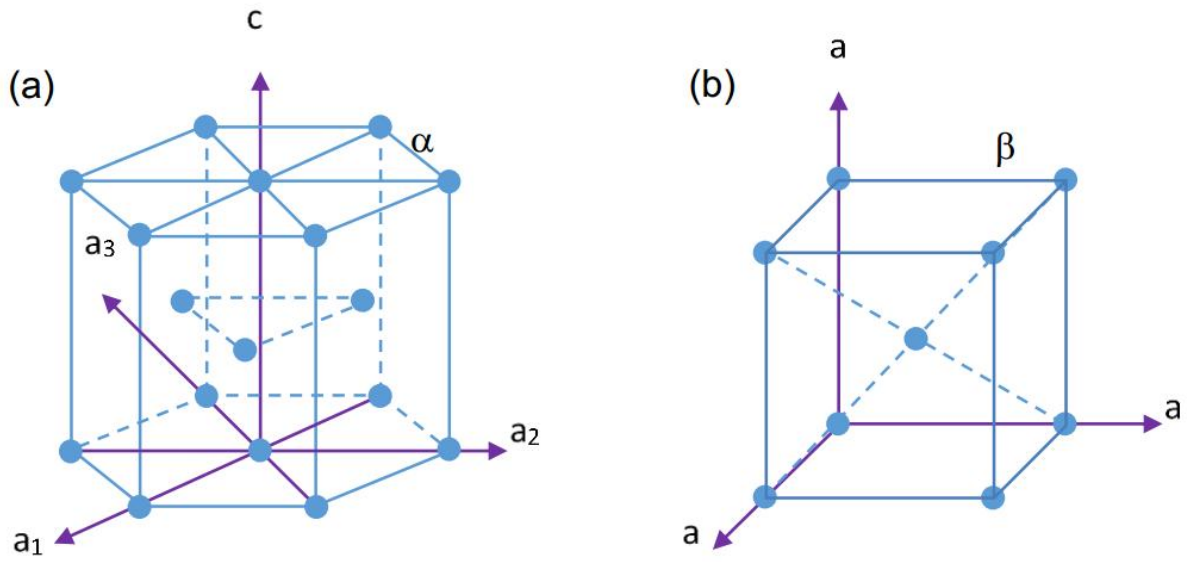

Figure 2.3 Unit cells of Ti-6Al-4V alloy: (a) α phase and (b) β phase.[27]

As the first titanium alloy developed, Ti-6Al-4V has two phases, α and β, reflecting the strength of α phase and the ductility of β phase. At room temperature, the α phase of Ti-6Al-4V has a lattice parameter of a= 0.295 nm and c= 0.468 nm,[19] and the c/a ratio is 1.59. Additionally, the phase transus ($\beta \rightarrow \alpha$) point of Ti-6Al-4V is 996°C[20]. In a h.c.p.-structured α phase, the three groups of most densely-packed planes are well defined: the basal plane (the (0002) plane), the three prismatic planes (the three $\{10\bar{1}0\}$ planes), and the six pyramidal planes (the six $\{10\bar{1}1\}$ planes).[29] In addition, the most densely-packed direction is direction <a> $<11\bar{2}0>$.[29] The b.c.c.-structured β phase has a lattice parameter of a= 0.332 nm. In β phase, the most densely-packed planes and directions are {111} planes and direction <111> respectively.[29]

Thus, the orientation relationship (OR) is determined as follows[3]:

$(0001)_\alpha // (110)_\beta$

$<11\bar{2}0>_\alpha // <1\bar{1}1>_\beta$

The α/β interface plane is oriented near one of the prismatic planes, resulting from the specific orientation relationship (OR).[30] This plane slightly varies due to its exact chemical composition, minimizing the interfacial dislocation energy. The Burgers-OR-based crystallographic relationship between α and β phase is shown in Figure 2.4.

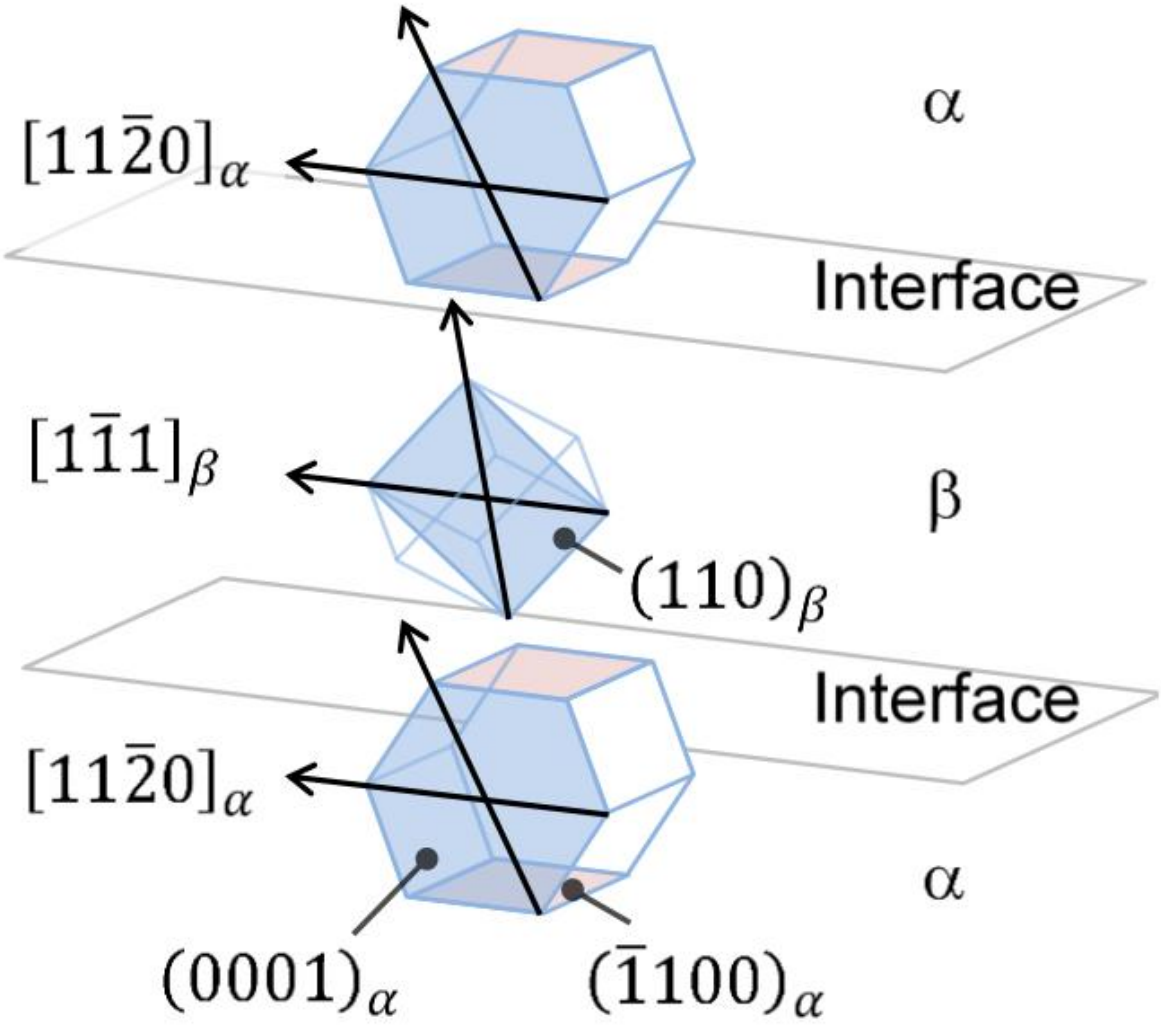

Figure 2.4 Burgers orientation relationship between α and β phases and their crystallographic relationship.[27]

2.2 Deformation of Ti Alloys

2.2.1 Slip System of Ti Alloys

Extensive research on the deformation of Ti alloys has been reported.[31] Briefly, slips can occur on basal, prismatic and pyramidal planes along three types of directions, <a>, <c> and <c+a>, in hcp-structured α phase, which are caused by three types of dislocations <a>, <c> and <c+a>. <a>-type dislocations with Burgers vector a/3<11$\bar{2}$0> are very common, which can glide on basal, prismatic and pyramidal planes, while the <c+a>-type dislocations with a Burgers vector a/3<11$\bar{2}$3> can only occur on pyramidal planes. The <c>-type dislocations are restricted to prismatic planes, which can't ever take place.[20] For α phase, prismatic slips are investigated and identified as the principal deformation mode of titanium, whose main slip directions are the close-packed directions of <a> type.[32]

The common slip planes and directions of single titanium crystals in α phase are listed in Table 2.2 and indicated in Figure 2.5.

As the β phase is a bcc structure, only slip <111> on planes {110}, {112} and {123} exists. Three different slip systems are shown in Figure. 2.6.[33, 34]

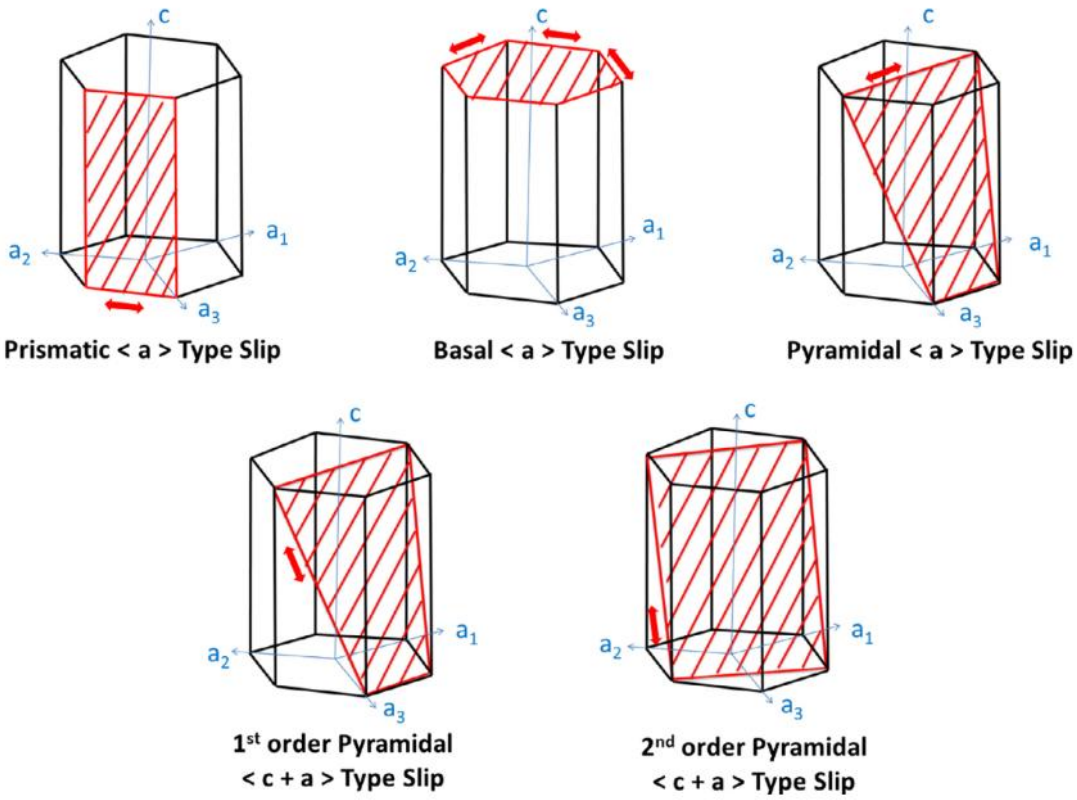

Figure 2.5 Common slip systems in α-Ti single crystals: prismatic <a>, basal <a>, 1th pyramidal <a>, 1th pyramidal <c+a> and 2nd pyramidal <c+a> slip.[18, 35]

Table 2.2 Possible slip systems in Ti alloy for α phase.[32, 36]

Slip system type	Burgers vector type	Slip direction	Slip plane	No. of slip systems	
				total	independent
1	a	<11$\bar{2}$0>	(0001)	3	2
2	a	<11$\bar{2}$0>	{10$\bar{1}$0}	3	2
3	a	<11$\bar{2}$0>	{10$\bar{1}$1}	6	4
4	c+a	<11$\bar{2}$3>	{$\bar{1}\bar{1}$22}	6	5

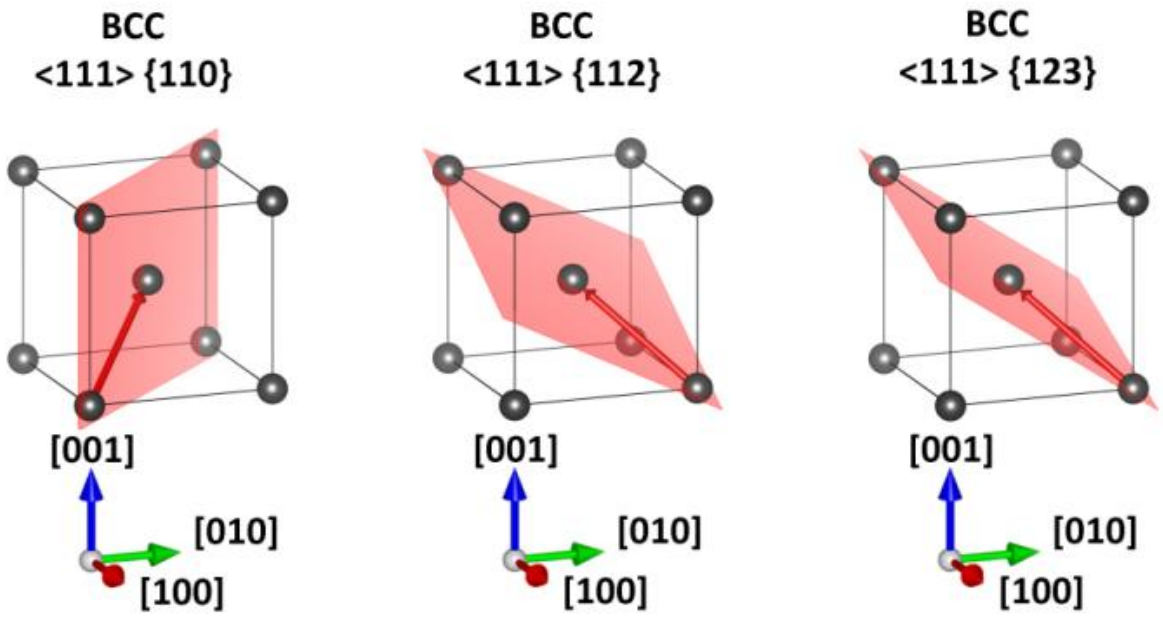

Figure 2.6 Common slip systems in β phase of Ti-6Al-4V: <111>{110}, <111>{112}, and <111>{123}.

2.2.2 Schmid Factor and CRSS

The difficulty level for slips to be activated on basal, prismatic or pyramidal planes is determined by the Schmid factors and critical resolved shear stress (CRSS), influencing the activation of slips. The most favourably-oriented slip system can be activated when its CRSS is reached, as a response to an applied stress. CRSS refers to the value needed for activating slips in a slip direction on a slip plane. The motion of dislocations is stress-activated and thermally-assisted, thus CRSS is a temperature-dependent parameter. Besides, the size of specimens, chemical composition and crystallographic texture can strongly influence CRSS[32]. CRSS and Schmid factors are written as:

$$\tau_{CRSS} = \sigma m \qquad (2\text{-}1)$$

$$m = \cos\varphi \cos\lambda \qquad (2\text{-}2)$$

where τ_{CRSS} is the CRSS value, σ is the applied stress, m is the Schmid factor, φ is the angle between the slip direction and applied stress, and λ is the angle between the normal of slip plane and the applied stress. Obviously, a higher Schmid factor makes the slip system more easily activated with the same CRSS. Materials with a lower CRSS are more easily activated than those with a higher CRSS. The schematic diagram of slip directions and planes is shown in Figure 2.7.

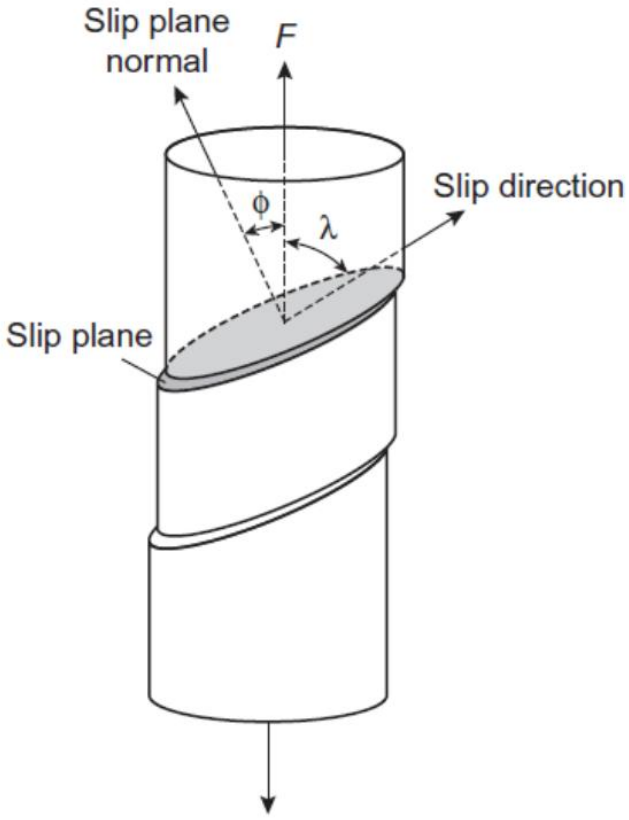

Figure 2.7. A schematic diagram of slip plane and slip direction.

2.2.3 Anisotropy of the Deformation of Ti Alloys: The Anisotropy of Slip System and Different Directions of Slip <a>

For the less symmetric hcp structure of α phase in single Ti crystals, CRSS differs in various slip systems. CRSS reflects the possibility of the activation of certain slip systems. A lower CRSS means that slip systems are activated more easily. In order to determine the precise value of CRSS of α-Ti, a library of deformation research on Ti-Al binary alloys subjected to a variety of strain rates and temperatures has been studied. Generally, the CRSS value of <a>-type slips is much smaller than that of <c+a> slips. More specifically, it is easier to activate basal and prismatic <a>-type slips according to their lower CRSS. It has been reported that

the large CRSS values of <c+a>-type slips on pyramidal planes are mainly because of their large Burgers vectors.[37] Therefore, in α-Ti polycrystals, just a small percentage of <c+a> slips can be achieved. Only in situations with the minimum mobility of <a>-type dislocations, such as when the loading direction is parallel to the c-axis, when there is a high strain rate or a low temperature, can <c+a>-type dislocations be activated.[30] Additionally, the CRSS value is also dependent on the chemical composition of alloys.

Most slips in Ti-Al binary alloys happen on prismatic planes when the weight percentage of Al is less than 2.9%, but with the increase of Al concentration, basal slips become more significant.[13] Salem and co-workers carried out the measurement of CRSS value on a lamellar Ti-6Al-4V structure at 815°C.[38] The measured CRSS of $<a_l>$-type slips was only approximately 42 MPa, one fifth of 210 MPa at room temperature (measured by Savage et.al[39] in Ti-6246Si). At room temperature, there is difference in the CRSS of <a>-type basal, prismatic and pyramidal slips, whose relationship is $\{10\bar{1}0\} \leq (0002) \leq \{10\bar{1}1\}$. Furtherly, Table 2.3 shows the relative CRSS values of prismatic slips in α-Ti and α/β Ti alloys, summarized by Mayeur et.al.[40] Also, the range of CRSS value of different slip systems is listed in Table 2.4.

Table 2.3 Relative room temperature CRSS values of different slip systems, normalized to prismatic <a> slip, for single α phase Ti and dual phase Ti-Al alloys.

$\tau_{CRSS}^{basal<a>}/\tau_{CRSS}^{prism<a>}$	$\tau_{CRSS}^{pyr<a>}/\tau_{CRSS}^{prism<a>}$	$\tau_{CRSS}^{pyr<c+a>}/\tau_{CRSS}^{prism<a>}$	References
1.25	-	2.625	[41]
0.9-1.3	1	1.1-1.6	[42]
1.5	1	3	[43]
5	5	8-15	[44]
1	-	8	[45]
1.43	-	4.23	[46]
1	2	3	[40]

Table 2.4 The summary of CRSS values of different slip systems for single α phase Ti and dual phase Ti-Al alloys at room temperature.

	CRSS values (MPa)	References
$\tau_{CRSS}^{prism<a>}$	300-392	[40] [47]
$\tau_{CRSS}^{basal<a>}$	340-444	[43] [47]
$\tau_{CRSS}^{pyr<a>}$	404-680	[40] [47]
$\tau_{CRSS}^{pyr<c+a>}$	631-1035	[40] [47]

Apart from the anisotropy of slip planes in Ti alloys, that of different <a>-type slips on the same slip plane in dual-phase Ti alloys is reported. [1, 16, 39] It is shown in Table 2.5 that on the same prismatic or basal plane, $CRSS_{a1} < CRSS_{a2} < CRSS_{a3}$. Since there are corresponding β-phase $<b_1>$ slips in $<a_1>$ slips, $<a_2>$ slips involve slight mis-orientated $<b_2>$ slips in β phase, there are no corresponding β-phase slips in $<a_3>$ slips, and there is a trend of an increasing CRSS when changing $<a_1>$, $<a_2>$ to $<a_3>$. This indicates that with the misorientation of slip systems in two phases becoming larger, the deformation impeded by interfaces of Ti alloys becomes stronger.

Table 2.5. Anisotropy of the CRSS for slips <a_1>, <a_2>, and <a_3> on basal and prismatic plane, summarized based on the macro-compression and micro-tension testing of Ti alloys. 0.2% offset yield strength was used to calculated CRSS.[1, 16, 39]

Slip direction	CRSS (MPa)		
	Basal plane	Prismatic plane	Prismatic plane
	Ti-6Al-4V microscale tensile	Ti-6Al-2Sn-4Zr-2Mo microscale tensile	Ti-5Al-2.5Sn microscale compression
a_1	341	208	267
a_2	357	215	293
a_3	366	230	-

The anisotropy of slip systems can be illustrated based on the Peierls-Nabarro (P-N) model[48-50], which reflects the lattice resistance when moving a dislocation. The critical stress is expressed as:

$$\tau = \frac{2\mu}{1-v}\exp\left[-\frac{2\pi d}{b(1-v)}\right] \qquad (2\text{-}3)$$

Where τ is the critical stress, μ is the shear modulus, v is the Poisson's ratio, b is the Burgers vector, and d is the interplanar spacing. Based on this equation, the critical stress can increase with a larger magnitude of Burgers vector or a smaller interplanar spacing.

2.2.4 Size Effect on the Yield Stress

The size effect on mechanical properties of Ti alloys is commonly investigated, which includes intrinsic and extrinsic size effect[51, 52]. The intrinsic size effect involves the key factors of the properties of the targeted materials inside themselves. As an example, the strength of polycrystalline metals can be affected by their grain size, or the distance between two neighbouring boundaries. The yield stress σ_y has a relationship with the grain size d, following the Hall-Petch equation[53, 54]:

$$\sigma_y = \sigma_0 + kd^{-n} \qquad (2\text{-}4)$$

Where σ_y is the yield stress, σ_0 is the lattice friction of the constituting single crystals, k is a constant related to materials, d is the grain size inside materials, and n is a constant number 0.5[55, 56], which can vary among different materials. As is descried in the equation above, the grain size d is a key parameter that can be adjusted to determine the yield stress. With the grain size d decreasing, the yield stress grows. However, the application of the normal Hall-Patch equation[57] to polycrystalline materials is limited when the grain size reaches the critical value, which is about 40nm, as is shown in Figure 2.8. Within this small scale, when grain size is smaller than 40nm, grain boundary sliding and dislocation absorption at grain boundaries dominate the deformation process. Thus, the plastic deformation mechanisms change from mediated dislocations to mediated grain boundaries, leading to softening[58, 59].

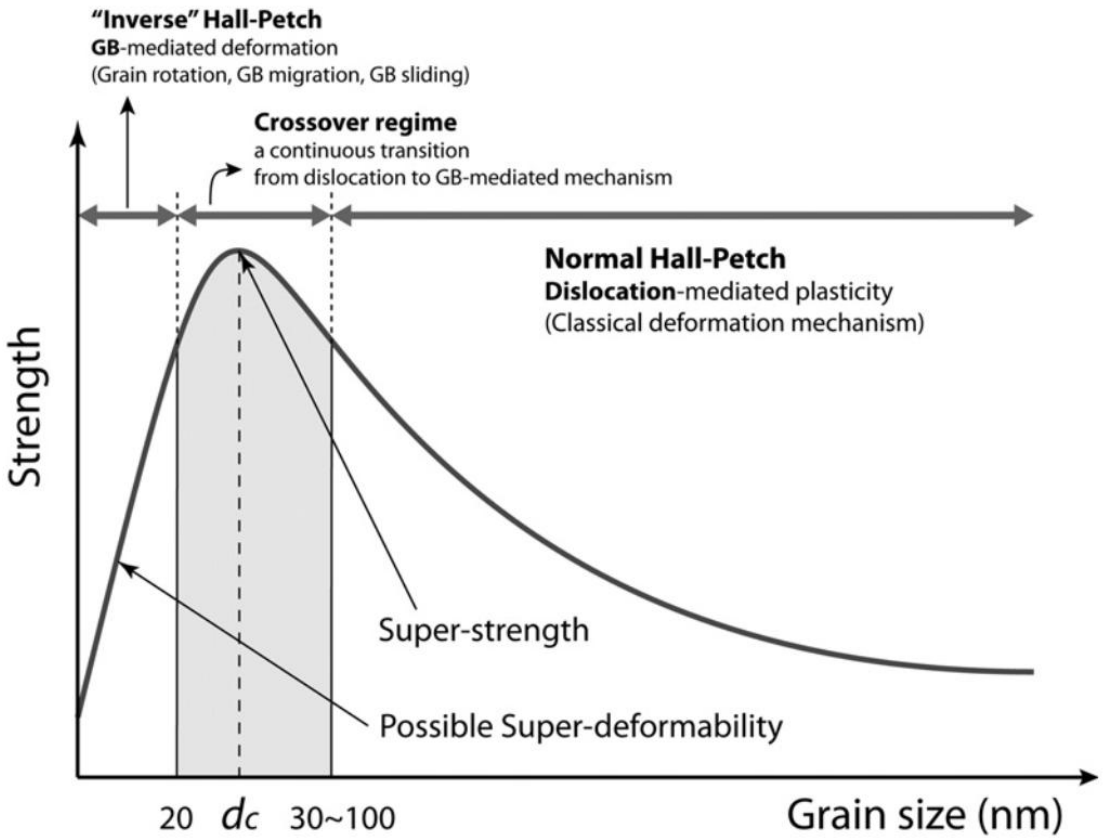

Figure 2.8 Hall-Petch relationship for polycrystalline materials. When the grain size decreases below dc, the normal Hall-Petch relation changes to inverse Hall-Petch relation[57].

Extrinsic size effect means that external dimensions are able to contribute to the strength of a material. In order to explain the extrinsic size effect on strength, three principal mechanisms have been proposed, which are geometrically-necessary dislocations (GND)[2, 60-62], dislocation starvation[63, 64] and dislocation source truncation[65-68]. The mechanism of geometrically necessary dislocations (GND) is, for instance, practical in non-uniform plastic deformation, micro-bending and nano-indentation, while the strain changes in the micro-compression tests are much more homogeneous. Thus, the mechanisms of dislocation starvation and dislocation source truncation are reasonable for the explanation in micro- and

submicro-compression tests. Within micro scale, dislocation source truncation dominates the mechanisms; however, within an even smaller scale, e.g., a submicro scale, dislocation starvation and surface nucleation contribute to the mechanisms[69].

2.3 Strain Localization in Ti

2.3.1 Introduction to Strain Localization and Slip Band Relationship

Strain localization is very important for understanding the mechanical properties and material failure. The initiation of cracks is highly dependent on the degree of strain localization resulted from the slip mode and microstructure.[70] With a strain localization in few slip bands, cracks are initiated. In other words, a persistent slip band (PSB) mechanism indicates that the strain must be carried out in limited regions and that strain concentration is highly related to crack nucleation. Therefore, the increase of slip bands leads to the reduction of strain concentration at slip bands, the delocalization of strain and the delay of crack initiation. Grain refinement like grain boundaries can largely increase the number of slip bands and reduce local strain concentration. After the deformation starts, subsequent deformation must happen in regions with strain concentration because the stress for a continuous deformation is lower.[71, 72]

2.3.2 Strain Localization through Dislocation Pile-up

Micro-structural inhomogeneity, such as phase and dislocation substructures, leads to strain inhomogeneity and localization. Micro-structural inhomogeneity dominates the mechanical behaviour of materials.

Shear band formation is more associated with a low ductility or energy fracture. Also, under conditions with a high loading rate, shear bands are more easily formed.[73] At barriers, dislocations are accumulated and piled up, then the large strain localization caused by dislocation avalanches leads to shear band formation.[70]

2.3.3 Strain Localization in Ti-6Al-4V Alloys with a Widimanstatten Microstructure

Widimanstatten microstructure of Ti64 alloys is obtained with a high cooling rate. Sangid et al.[74] investigated the strain localization of Ti-6Al-4V alloys. It was observed that interfaces played a significant role in strain localization, which was observed at interfaces.

2.4 Strengthening Mechanisms in Ti Alloys

2.4.1 Precipitate Strengthening

The mechanical properties of Ti alloys can be strengthened by existing precipitates.[75-78] Sun and co-workers[79] reported the effect of Ti_2Cu precipitates on the mechanical properties of Ti-2.5 Al alloys. The precipitate strengthening mechanism is caused by the resistance of dislocation movement. Two types of strengthening mechanisms can be summarized, the first is in the condition of small precipitates with coherent interfaces, which can be cut- off by the dislocations, often occurring in Al-Cu[80] and Al-Zn[81] alloys. In comparison, the second precipitate strengthening mechanism applied for large precipitates with non-coherent interfaces need to be bypassed by dislocations.

Normally, it is difficult to investigate the cut-off of small precipitates. Thus, strengthening mechanisms can be attributed to the bypassing of dislocations. The Orowan equation[82] can be introduced to describe the strengthening, which is:

$$\tau_p = \frac{Gb}{2\pi\lambda\sqrt{1-v}} \ln \frac{d_p}{r_0} \quad (2\text{-}5)$$

Where τ_p is the Orowan stress of precipitates, G is the shear modulus, b is the Burgers vector, λ is the effective planar inter-obstacle spacing, v is the Poisson's ratio, d_p is the mean particle spacing on the slip plane, and r_0 is the cut-off radius. r_0 is taken as the dislocation core radius.

2.4.2 Solid Solution Strengthening

Through the introduction of solute atoms into Ti alloys, the alloys can be strengthened due to the lattice distortion or collective atomic displacement caused by solute atoms[83-86], which is called solid solution strengthening. Larger lattice distortions lead to higher solid solution strengthening. For instance, higher strengthening is resulted from interstitial solute atoms rather than substitutional solute atoms. Solute elements with high strengthening also lead to a high Young's modulus.

According to the Labusch model [87], the solid solution strengthening can be evaluated by calculating the lattice distortion, which is expressed as:

$$\tau = M\tau_0 \quad (2\text{-}6)$$

Where M is the Taylor factor and τ_0 is the critical shear stress, which is described as:

$$\tau_0 = \left(\frac{F_m^4 c^2 w}{4Gb^9}\right)^{\frac{1}{3}} \quad (2\text{-}7)$$

Where F_m is the maximum energy when a solute atom interacts with a dislocation, c is the solute element concentration, w is the interaction range between a solute atom and a dislocation, G is the shear modulus, and b is the Burgers vector magnitude. The estimation of w is 5b[88].

2.4.3 Interface Strengthening

Grain boundaries, twin boundaries and interfaces are all interfaces, resulting in lattice misfit.

Slips can transmit through interfaces in polycrystalline and single-crystalline materials.[49, 89-91] The slip behaviour through interfaces within the micro scale is found to be different from that within the macro scale,[89] where the main criterion for slip activation is the Schmid factor, while other factors can influence the slip activation at local interfaces. The interfaces can be regarded as barriers to dislocation motions during plastic deformation, resulting in dislocation piling-up and stress concentration. Usually, the initiation of plastic deformation happens on one side of an interface with significant work-hardening. Then plastic flow begins on the other side of the interface.

There are several mechanisms useful for explaining slip transfer through interfaces, such as the absorption and desorption of dislocations at and from interfaces, the direct transmission of dislocations through interfaces and the nucleation of new dislocations on the side of an interface with fewer dislocations.[92]

Regarding the interfaces as barriers for dislocation movement, dislocation pile-up appears at interfaces. Eshelby, Frank and Nabarro (EFN)[93, 94] gave a well-known formula to describe interface strengthening, which is expressed as,

$$\tau_y = \tau_0 + \left[\frac{Gb(1-v)\tau_a}{\pi L}\right]^{\frac{1}{2}} \quad (2\text{-}8)$$

where τ_y is the yielding stress, σ_0 is the Peierls stress or lattice friction stress, G is the shear modulus, b is the dislocation magnitude, v is the Poisson's ratio, L is the length of pile-up, and τ_a is the stress for dislocations to overcome interface barriers or the nature of interface strengthening.

In this equation, the second term on the right-hand side can be given as,

$$kL^{-\frac{1}{2}} = \left[\frac{Gb(1-v)\tau_a}{\pi L}\right]^{\frac{1}{2}} \quad (2\text{-}9)$$

Where k is the Hall-Petch coefficient.

Interface strengthening τ_a is contributed from several factors, which are lattice parameter mismatch, shear modulus mismatch or Koehler interaction, stacking fault mismatch between two phases caused by changes in chemical composition, interface stress and w interaction of slip system mismatch.[94-100]

Lattice parameter mismatch is caused by lattice distortions resulted from lattice parameter differences. Thus, a local strain field exists at an interface. Dislocations need to go over the local strain field for propagation, and extra stress should be applied.

Koehler interaction is caused by the difference in the shear modulus of adjacent phases on two sides of an interface. Therefore, strain energy, besides the interface changes, makes dislocation gliding more difficult from the soft side to the hard side.

Chemical interaction or stacking fault mismatch results from chemical composition differences. When dislocations glide through interfaces, the dislocation core energy changes and then the materials are strengthened.

Interface stress is the stress required to elastically deform an interface, resulted from its tensor. Interface stress is negative under compression testing, which is related to interface energy and interface strain tensor.

w interaction refers to the change of dislocation slip direction and slip plane when going through interfaces, leading to the misfit of a slip system on both sides of an interface. Commonly, two geometric criteria should be met to achieve a favourable slip transference: a minimum angle (θ in Figure 2.9) between the incoming and outgoing slip plane as well as (φ in Figure 2.9) between the two Burgers vectors.

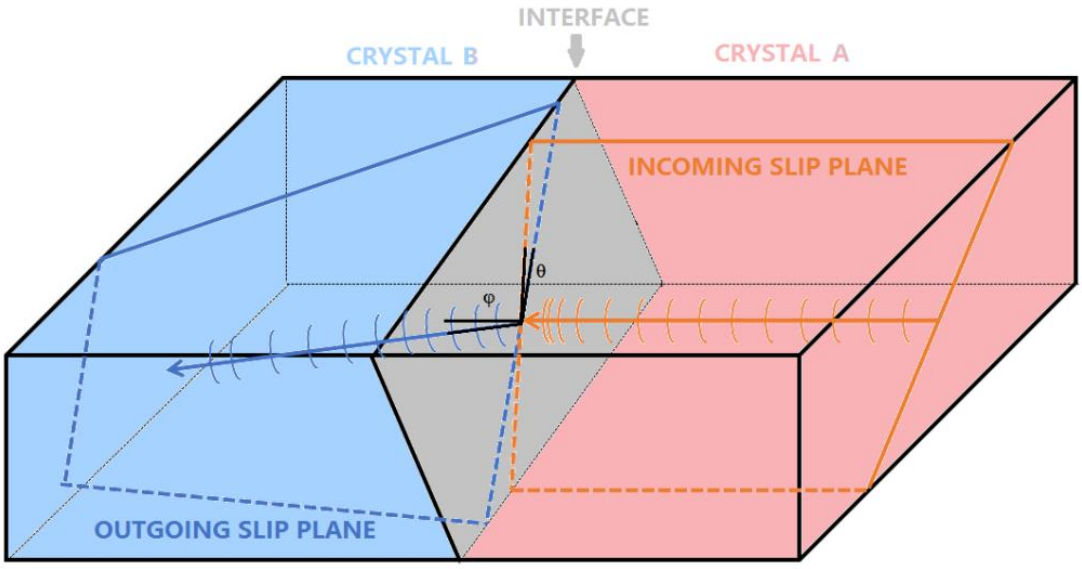

Figure 2.9 A scheme shows angle φ change between incoming and outgoing Burgers vectors and another angle θ change between incoming and outgoing planes when the slip transfers through an interface.[101]

In Ti alloys, the Burgers vectors between the two phases are not aligned in parallel. The magnitude of the angle between the two Burgers vectors has a strong effect on the slip

transfer through an interface. Creep studies on Ti-5Al-2.5Sn-0.5Fe bulk samples containing α/β interfaces at room temperature were reported by Suri et al.[16] The investigation of distinct <a> prismatic slip transfer behaviour in different colonies came up. When a_1= 1/3[$2\bar{1}\bar{1}0$], prismatic slips were activated inα phase, and the corresponding slip system activated in the β phase was 1/2[$11\bar{1}$]($\bar{1}21$). However, in a situation with the activation of a_2= 1/3[$\bar{1}2\bar{1}0$] prismatic slips in α phase, edge dislocations encountered each other at α/β interfaces and piled up, suggesting a stronger resistance to slip transfer through interfaces. The anisotropy of slip activation along different directions is supposed to be a consequence of the misalignment of Burgers vectors inα and β phase. The misorientation between a_1= 1/3[$2\bar{1}\bar{1}0$] and b_1= 1/2[$11\bar{1}$] is only 0.7°, much smaller than the 11.1° between a_2 and b_2.[102] So, a_1 dislocations easily go through α/β interfaces, corresponding to the lowest CRSS and strain hardening rate, and a_2 dislocations are accumulated near interfaces inβ phase, piled up when slips are supposed to transmit fromβ phase toα phase. For a_3 dislocations, there is no corresponding b_3 dislocation inβ phase, which can be activated for slip transfer, thus a huge number of a_3 dislocations are piled up near interfaces in α phase in this case.

Additionally, the misorientation of slip planes in Ti alloys is another factor which influences slip transfer besides the misorientation of the slip direction. The basal slip plane (0001) for <a>-type dislocations inα phase is parallel to the corresponding {101} slip plane inβ phase due to the orientation relationship among α and β phases (0001)α//(101)β, [$2\bar{1}\bar{1}0$]α// [$11\bar{1}$]β and [$0\bar{1}10$]α// [$\bar{1}21$]β.

Since <c+a>-type slip transmission is more difficultly activated through α/β interfaces, it has only been reported in a few publications [103, 104], compared with the most widely studied <a>-type slip transmission. However, when the loading direction is along the c-axis in α phase, <c+a> slips become significant. Transmission modes of <c+a>-type slips can be

classified into three types: (1) direct transmission[1, 104]; (2) slip transmission with the generation of residual dislocations near interfaces;[104] (3) indirect slip transmission, in which the incoming dislocations are not able to go through interfaces, but at the other side of them new dislocations are generated.

2.5 Models of Interface Strengthening Calculation

In order to quantitively calculate interface strengthening, several models are studied in this project. As is discussed above, several factors contribute to interface strengthening, which are

τ_{misfit}, which is determined by lattice parameter mismatch;

τ_k, Koehler stress caused by shear modulus mismatch;

τ_{ch} , chemical interaction caused by the stacking fault mismatch resulted from chemical differences;

τ_f, interface stress related to interface energy and interface strain tensor;

τ_w, *w* interaction based on the change of slip direction and slip plane.

$$\tau_{misfit} = 0.3\overline{G}\sqrt{\frac{2b(\delta-\varepsilon)}{\lambda}} \qquad (2\text{-}10)$$

Where $\overline{G}$ is the average shear modulus, b is the magnitude of the Burgers vector, δ is the misfit of lattice parameters, ε = 0.76 δ is the residual elastic strain of major heterointerfaces[98], and λ is the layer thickness.

$$\tau_k = \frac{G_A(G_B-G_A)}{4\pi(G_B+G_A)} \times \frac{b}{h} \qquad (2\text{-}11)$$

Where G_A and G_B are the shear modulus of two phases, b is the magnitude of Burgers vector, h is the distance between the interface and dislocation, and the minimum distance is the dislocation core distance of 2b.

$$\tau_{ch} = \frac{\Delta\gamma}{b} \qquad (2\text{-}12)$$

Where $\Delta\gamma$ is the stacking fault energy difference, and b is Burgers vector.

$$\tau_f = f/h \qquad (2\text{-}13)$$

Where f is the interface energy, and h is the interface strain.

$$\tau_w = \tau_A - \tau_B \qquad (2\text{-}14)$$

τ_A and τ_B are the Peierls stress of slips in two phases. The Peierls stress is,

$$\tau = \frac{2\mu}{1-v}\exp[-\frac{2\pi d}{b(1-v)}] \qquad (2\text{-}3)$$

Where τ is the critical stress, μ is the shear modulus, v is the Poisson's ratio, b is the Burgers vector, and d is the interplanar spacing.

Rao and co-workers[95] reported the atomistic simulation of interface strengthening based on the dislocation-interface interaction within a Cu-Ni nanolayered composite, which was found to be dramatic while reducing the layer thickness. The interface strengthening is given as,

$$\tau_{int} = \tau_{misfit} + \tau_k + \tau_{ch} + \tau_w \qquad (2\text{-}15)$$

In this equation, the lattice mismatch, shear modulus mismatch, stacking fault mismatch and misorientation of slip systems are involved.

Another research group of Bufford and et al.[96] studied the strength of Ag/Al multilayer films. In both Ag and Al layers, stacking faults were investigated, which increased rapidly

with the reduction of individual layer thickness. Definitely, the interfaces of multilayers are barriers for the dislocation movement. In their research, only three factors, namely Koehler stress, chemical interaction and *w* interaction, are considered, and interface strengthening is expressed as,

$$\tau_{int} = \tau_k + \tau_{ch} + \tau_w \qquad (2\text{-}16)$$

In a BCC-FCC multilayer system, Hosson's group[94] observed that interfaces strengthened the high-entropy-alloy (HEA) $Al_{0.7}CoCrFeNi$ due to the small-scale deformation through BCC-FCC interfaces. Lattice parameter mismatch, shear modulus mismatch and stacking fault mismatch contribute to interface strengthening, which is expressed as,

$$\tau_{int} = \tau_{misfit} + \tau_k + \tau_{ch} \qquad (2\text{-}17)$$

Additionally, Huang et al.[97] studied interface strengthening in a FCC-BCC multilayer system, such as Cu/Al and Cu/W. A small lattice mismatch, τ_{coh}, which represents the effect of coherent interfaces, is introduced into the formula. Also, the interface stress is considered. Therefore, interface strengthening consists of five components, which is given as,

$$\tau_{int} = \tau_k + + \tau_{coh} + \tau_{misfit} + \tau_{ch} + \tau_f \qquad (2\text{-}18)$$

The τ_{coh} derived from coherency stress is described as,

$$\tau_{coh} = m\sqrt{\frac{1}{6}}AE\delta\frac{h_c}{h} \qquad (2\text{-}29)$$

Where *m* is the number of multilayers, *A* is the composition modulation amplitude, *E* is the elastic modulus average, δ is the misfit of lattice parameters, h_c is the critical coherent thickness of layers, and *h* is the average layer thickness.

The summary of factors contributing to interface strengthening and different models of interface strength is concluded in Table 2.6 and Table 2.7.

Table2.6. Summary of several factors contributing to the interface strengthening.

factors	equation	Ref.
lattice parameter mismatch	$\tau_{misfit} = 0.3\overline{G}\sqrt{\frac{2b(\delta-\varepsilon)}{\lambda}}$	[94, 97]
Koehler stress	$\tau_k = \frac{G_A(G_B-G_A)}{4\pi(G_B+G_A)} \times \frac{b}{h}$	[94, 96, 97]
chemical interaction	$\tau_{ch} = \frac{\Delta\gamma}{b}$	[94, 96, 97]
interface stress	$\tau_f = f/h$	[97]
w interaction	$\tau_w = \tau_A - \tau_B$ $\tau = \frac{2\mu}{1-v}\exp[-\frac{2\pi d}{b(1-v)}]$	[99]

Table2.7. Summary of different models of the interface strengthening.

Model of interface strengthening	Ref.
$\tau_{int} = \tau_{misfit} + \tau_k + \tau_{ch} + \tau_w$	[95]
$\tau_{int} = \tau_k + \tau_{ch} + \tau_w$	[96]
$\tau_{int} = \tau_{misfit} + \tau_k + \tau_{ch}$	[94]
$\tau_{int} = \tau_k ++ \tau_{coh} + \tau_{misfit} + \tau_{ch} + \tau_f$	[105]

2.6 Aims and Objectives

This project aims to study the effect of α/β interfaces number on CRSS values, shear band formation and pillar size effect sensitivity during the plastic deformation of the Ti-6Al-4V alloy, and to understand the function of α/β interfaces on dislocation movement. In order to achieve this aim, several objectives are identified:

- To investigate the morphology of micro-pillars before and after compression.
- To compare the CRSS values among compressed pillars containing various number of β fillets.
- To observe the shear band nucleation, formation and distribution with SEM in micropillars containing various number of β fillets.
- To estimate interface strengthening by theoretical calculation in considerations of lattice parameter mismatch, Koehler stress, interface stress, and *w* interaction.
- To investigate the interaction between dislocations and interfaces using TEM.
- To compare the percentage increments of CRSS values base on size effect on CRSS in micro-pillars containing various numbers of β fillets, assessing size effect sensitivity.

Chapter 3 Materials and Experimental Methods

In these studies, the commercial Ti-6Al-4V alloy is provided by Timet (Titanium Metals Cooperation) in the form of a billet. To better understand the role of the β phase in dual phase Ti alloys during plastic deformation, the following methods have been developed. Firstly, two heat-treatments (furnace-cooling and air-cooling) have been performed to obtain fully lamellar micro-structures with different β spacings, allowing a single micropillar to contain multiple β fillets. The widths of β phase and β spacing range from 0.1 μm to 2 μm and 1 μm to 8 μm, respectively. Also, in order to obtain enough number of micro-pillars, the size of each grain should be large enough for further pillar milling. With a suitable finish after mechanical polishing, the grain orientations of the specimen were identified by electron back-scattered diffraction (EBSD) with an Oxford Instrument system in the TESCAN MIRA-3 microscope. Desired grains were identified which would make prismatic <a>, pyramidal <a> and basal <a> slips activated. Following this, the dual beam focused ion beam (FEI-PFIB) was used for micropillar fabrication with the pillar size ranging from 2-10 μm in diamter. Then, the Alemnis system was applied with displacement control to carry out micro-compression, and the TEM foils were prepared by FEI-PFIB. Finally, a FEI Talos 200F TEM was utilised for dislocation analysis and slip system identification.

3.1 Heat Treatment and Polishing

In order to study the role of the interface during deformation, a suitable heat treatment is required to achieve the dual phase fully lamellar microstructure. Large ingots were cut into small specimens of 10 mm × 10 mm × 20 mm from the as-received commercial Ti64 alloy.

The Ti64 alloys were encapsulated in quartz tubes with Mo/Ta foil as an additional oxygen getter to avoid oxygen penetration into the alloy, which can affect the strength dramatically. The tube was evacuated into a vacuum and backfilled with pure argon 3 times to remove all the present air.

The specimen was placed in the furnace at room temperature and ramped up at 10°C/min to 200°C. At this temperature, samples were held for 30 min, aiming to be rid of any remaining hydrogen and oxygen. The temperature was raised to 1100°C at the same rate of 10°C/min and held for 3 hrs to give enough time to ensure complete transformation to the β phase. Thereafter, two kinds of cooling rates were applied to obtain fully lamellar microstructures with different β spacings and sizes – namely, air cooling and furnace cooling, producing small and relatively large β spacing and fillets, respectively. The heat treatment process is summarised in **Figure 3.1**.

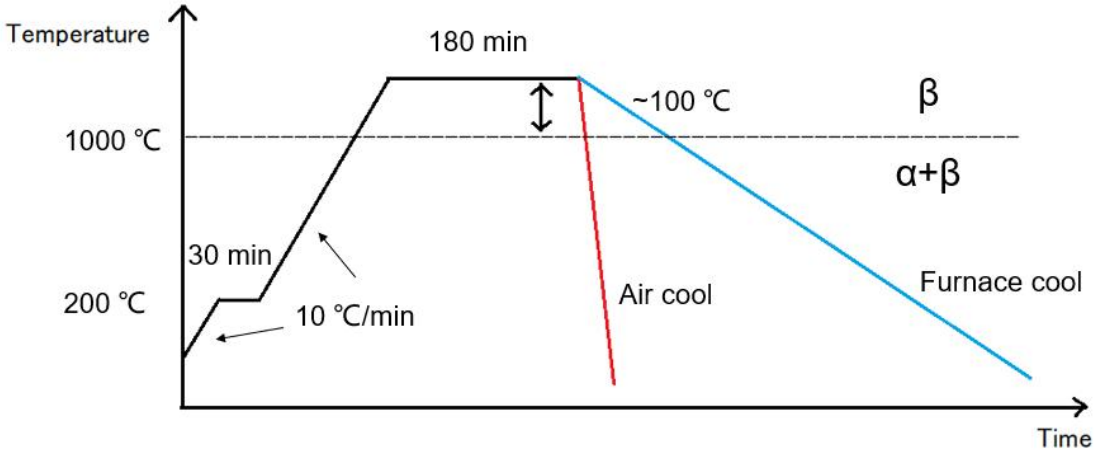

Figure 3.1. The procedure of Ti-6Al-4V alloy heat treatment with two different cooling rate of furnace cooling (blue) and air cooling (red).

After the heat treatment, the specimen was cut into smaller pieces and mounted into a conductive Bakelite matrix via 7 min heating and 7 min water cooling for mechanical polishing. In order to obtain a “mirror-like” surface finish for EBSD mapping, the mounted specimen was first ground with silicon carbide paper 200, 400, 800, 1200 grits with water lubrication for 5 min at a rotating speed of 300 rpm. The specimen was polished with a series of polishing cloth with diamond abrasives. A mixture of hydrogen peroxide (30%) and colloidal silica (OP-S) for about 1 hr concluded the sample preparation.

Finally, the specimen was cleaned with water and immersed in methanol for 10 min ultrasonic cleaning. Thus, the “mirror-like” finish was achieved for SEM and EBSD mapping in order to observe the microstructure and distinguish the orientation of grains.

3.2 Orientation Selection by EBSD Mapping

In order to obtain a basic crystal orientation mapping, the electron backscattered diffraction (EBSD) technique was utilized. In this study, a Tescan Mira-3 with an Oxford Instruments EBSD detector with accompanying Aztec software were used to acquire the EBSD mapping. The specimen was pre-tiled at 70° from the horizontal axis to let the EBSD detector capture information. The working distance between the gun and specimen surface was about 15 mm. After the electron beam hits the specimen under the accelerating voltage of 20 kV, backscattered electrons are generated and captured to create a Kikuchi pattern on a phosphor screen. The Kikuchi bands represents the diffracted crystal planes of the specimen. Thus, different orientations of grains define the different crystal lattice reflections, and results in certain geometrical arrangement of Kikuchi patterns. The step size of scanning the region of interest depends on the magnification, ranging from 0.2 μm to 10 μm. The OI Channel 5 software was used to analyse the data to identify the orientation of various phases, Euler

angles and grain boundaries. The Aztec software can not only generate an orientation map based on the EBSD data, but also pole figures or inverse pole figures for viewing the crystal misorientation.

In this study, five orientations (e.g $[11\bar{2}0]$) were selected to activate prismatic $<a_2>$ and $<a_3>$, pyramidal $<a_3>$ and basal $<a_1>$ and $<a_3>$ slips. For instance, EBSD analysis gives selected orientation with Euler angles of 41.1°, 87.1° and 51.4°, which is 8.9° away from the exact $[1\bar{2}10]$ direction. This is an acceptable misorientation at which prismatic <a> slip will be activated.

3.3 Calculation of Schmid Factor and Resolved Shear Stress (RSS)

In the dual phase Ti-6Al-4V alloy, there existing h.c.p. α phase and b.c.c β phase, which are of 4 index and 3 index systems, respectively.

In b.c.c. structured β phase, the calculation of the Schmid factor is:

$$m = cos\varphi cos\lambda = \cos(r_1 \cdot r_2) = \frac{r_1}{|r_1|} \cdot \frac{r_2}{|r_2|}$$
$$= \frac{u_1u_2 + v_1v_2 + w_1w_2}{\sqrt{(u_1^2 + v_1^2 + w_1^2)(u_2^2 + v_2^2 + w_2^2)}} \frac{u_1u_3 + v_1v_3 + w_1w_3}{\sqrt{(u_1^2 + v_1^2 + w_1^2)(u_3^2 + v_3^2 + w_3^2)}}$$

(4-1)

Where $[u_1v_1w_1]$, $[u_2v_2w_2]$ and $[u_3v_3w_3]$ are respectively the loading direction, the slip direction and the slip plane normal. φ represents the angle between the loading direction and slip direction, and λ represents the angle between the loading direction and slip plane normal.

Since the h.c.p structure is more complicate due to its 4 Miller-indices system, the calculation of Schmid factors for Ti-6Al-4V alloy becomes difficult when introducing the c/a ratio when

compared to BCC and FCC structures. The arbitrary crystal vector can be defined by 4 indices of a_1, a_2, a_3, and c, where the $a_3 = -(a_1 + a_2)$:

$$r = ua_1 + va_2 + ta_3 + wc$$

with the constraint

$$u + v + t = 0$$

Usually, [*uvtw*] and (hkil) describe line directions and planes. A line direction and its parallel direction to a plane normal in hcp structures have the relationships:

$[uvtw] = [hkil]^* = [hki\lambda^{-2}l]$,

$\lambda^2 = \frac{2c^2}{3a^2}$, $w = \lambda^{-2}l$

$$m = cos\varphi cos\lambda = \cos(r_1 \cdot r_2) = \frac{r_1}{|r_1|} \cdot \frac{r_2}{|r_2|}$$

$$= \frac{\boldsymbol{u_1u_2 + v_1v_2 + t_1t_2 + \frac{2c^2}{3a^2}w_1w_2}}{\sqrt{(\boldsymbol{u_1^2 + v_1^2 + t_1^2 + \frac{2c^2}{3a^2}w_1^2})(\boldsymbol{u_2^2 + v_2^2 + t_2^2 + \frac{2c^2}{3a^2}w_2^2})}} \frac{\boldsymbol{u_1u_3 + v_1v_3 + t_1t_3 + \frac{2c^2}{3a^2}w_1w_3}}{\sqrt{(\boldsymbol{u_1^2 + v_1^2 + t_1^2 + \frac{2c^2}{3a^2}w_1^2})(\boldsymbol{u_3^2 + v_3^2 + t_3^2 + \frac{2c^2}{3a^2}w_3^2})}}$$

$$= \frac{u_1u_2 + v_1v_2 + t_1t_2 + \frac{2c^2}{3a^2}w_1w_2}{\sqrt{(u_1^2 + v_1^2 + t_1^2 + \frac{2c^2}{3a^2}w_1^2)(u_2^2 + v_2^2 + t_2^2 + \frac{2c^2}{3a^2}w_2^2)}} \frac{u_1h + v_1k + t_1i + \frac{2c^2}{3a^2}w_1\lambda^{-2}l}{\sqrt{(u_1^2 + v_1^2 + t_1^2 + \frac{2c^2}{3a^2}w_1^2)(h^2 + k^2 + i^2 + \frac{2c^2}{3a^2}(\lambda^{-2}l)^2)}}$$

$$= \frac{u_1u_2 + v_1v_2 + t_1t_2 + \frac{2c^2}{3a^2}w_1w_2}{\sqrt{(u_1^2 + v_1^2 + t_1^2 + \frac{2c^2}{3a^2}w_1^2)(u_2^2 + v_2^2 + t_2^2 + \frac{2c^2}{3a^2}w_2^2)}} \frac{u_1h + v_1k + t_1i + w_1l}{\sqrt{(u_1^2 + v_1^2 + t_1^2 + \frac{2c^2}{3a^2}w_1^2)(h^2 + k^2 + i^2 + \frac{3a^2}{2c^2}l^2)}}$$

(4-2)

Where $[u_1v_1w_1]$, $[u_2v_2w_2]$ and $[u_3v_3w_3]$ are respectively the loading direction, the slip direction and the slip plane normal.

Since the h.c.p structure is more complicated due to its 4 Miller-indices system, it has 5 types of slip systems, which are prismatic <a>, basal <a>, pyramidal <a>, first order pyramidal <c+a> and second order pyramidal <c+a>. With the aim of activating one type of slip system, the loading direction should be selected rationally.

The calculation of Schmid factors has been listed in the result section. In Ti-6Al-4V alloy, c=4.68 nm and a=2.95nm with c/a=1.587 for α phase. The Schmid factor is used for slip system analysis in the TEM examination.

3.4 Micro-pillar Fabrication

The cylinder-shaped micro-pillars with aspect ratios of 2:1 were prepared by a FEI-PFIB from the selected colonies at a 30-kV voltage. Here there are some parameters that should be discussed regarding the fabrication. Firstly, the shape of micro-pillar - some researchers select square shapes for pillar milling. A cylindrical shape was chosen in this work, as the majority of Ti-6-4 alloy is α phase (a h.c.p structure not a cubic structure), the stress would concentrate on the sharp edge during compression which may affect the slip system activation. In addition, the square shape is less symmetric than the cylinder such that 6 equivalents pyramidal <c+a> slip systems are much less likely to be activated. Second, the aspect ratio between height and top diameter was selected to be around 2:1 because the ratio should be larger than c/a=1.587 for α phase in Ti-6-4 alloy, and when the aspect ratio is too large the buckling effect would be magnified such that the pillar would bend during compression. Third, the taper angle should be small enough to avoid stress concentration on the top. Due to the milling method (of using an ion beam) the longer exposure under the ion beam, the more materials milled, the material at the top is milled more than the bottom, resulting in smaller top diameter. Larger beam currents lead to more significant taper angle

than smaller currents. Thus, at the final stage of milling, small currents should be selected to reduce the non-uniform stress during the micro-compression. Finally, a big cave should be drilled in order to investigate the whole pillar when it is tilted to a certain angle, otherwise the pillar has been known to be hidden by the surroundings. Larger pillars require larger cave to be dug. Additionally, the cave size should be larger than 20 μm, which is the diameter of the diamond flat punch tip.

About 60 pillars with different orientations, sizes, β sizes and spacing were made in this study with an annular milling method. The nominal top diameter of pillars is 2-10 μm. Different parameters for milling procedures are used for pillar fabrication. A relatively large current of 60 nA was firstly used for quick milling of the cave to save time. Then the current was reduced for the subsequent milling until 1 nA was used at the final milling stage.

3.5 Micro-pillar Compression

Micro-compression is a new approach to investigate the principles of mechanical properties of materials at the micro-scale. Also, for those materials which have difficulty to grow large single crystals, micro-compression offers an opportunity to study the single crystal properties.

Inspired by the great research of Uchic and Dimiduk on micro-compression of Ni-based alloys[106, 107] , a quasi-static study on the single crystal property at the micro-scale of dual phase Ti alloys was carried out. The micro-pillar tests were performed in a FEI-PFIB by using an Alemnis nano-indentation system, equipped with a 20 μm sized diamond flat punch tip.

The constant strain rate was set to $1 \times 10^{-3}\ s^{-1}$. When the strain rate is too small, thermal effects become significant because the compression takes a longer time. However, if the

strain rate is too large, dislocations do not have enough time to interact and move away. The specimen should be mounted with super glue, making the specimen firmly fixed to avoid any displacement during the compression. Silver paint provides conductivity when observing under the electron beam. The nominal strain ranges from 5%-8%, which can produce strain above the elastic limit with limited plastic deformation. Otherwise, if the strain is too large, a significant number of dislocations would be activated, making it difficult to analyse in the TEM. Another unavoidable factor that can influence the stress-strain curve is the contact misfit between the tip underside and the specimen top surface, which means their two faces are not precisely parallel to each other. Thus, at the beginning of the micro-compression, the flat punch tip couldn't fully contact the pillar top surface, resulting a non-linear change in the elastic deformation. Furthermore, the misalignment between the pillar axis and the flat tip axis is a notable issue, leading to a non-uniaxial stress state. In order to minimise the misalignment, the Alemnis micro-compression system was tilted to 20° to locate the tip at the pillar axis.

At least 3 micro-pillars were compressed to guarantee repeatability. The raw data of Load-Displacement was given by the Alemnis software, and the true strain and stress were calculated.

The micro-compression tests are only presented in the form of true stress and strain in the following chapters. Due to the difficulty of determining the yield point, the nominal yield stresses were measured at the 0.2% offset point. The turning point between elastic and plastic deformation is very difficult to be distinguished. Thus, the 0.2% offset point is calculated as the yield strength, which is defined as the stress value, also called proof stress, corresponding to the 0.2% plastic strain. The 0.2% offset point is obtained by constructing a parallel linear line to the elastic line by 0.2% strain, as shown in Figure 3.2.

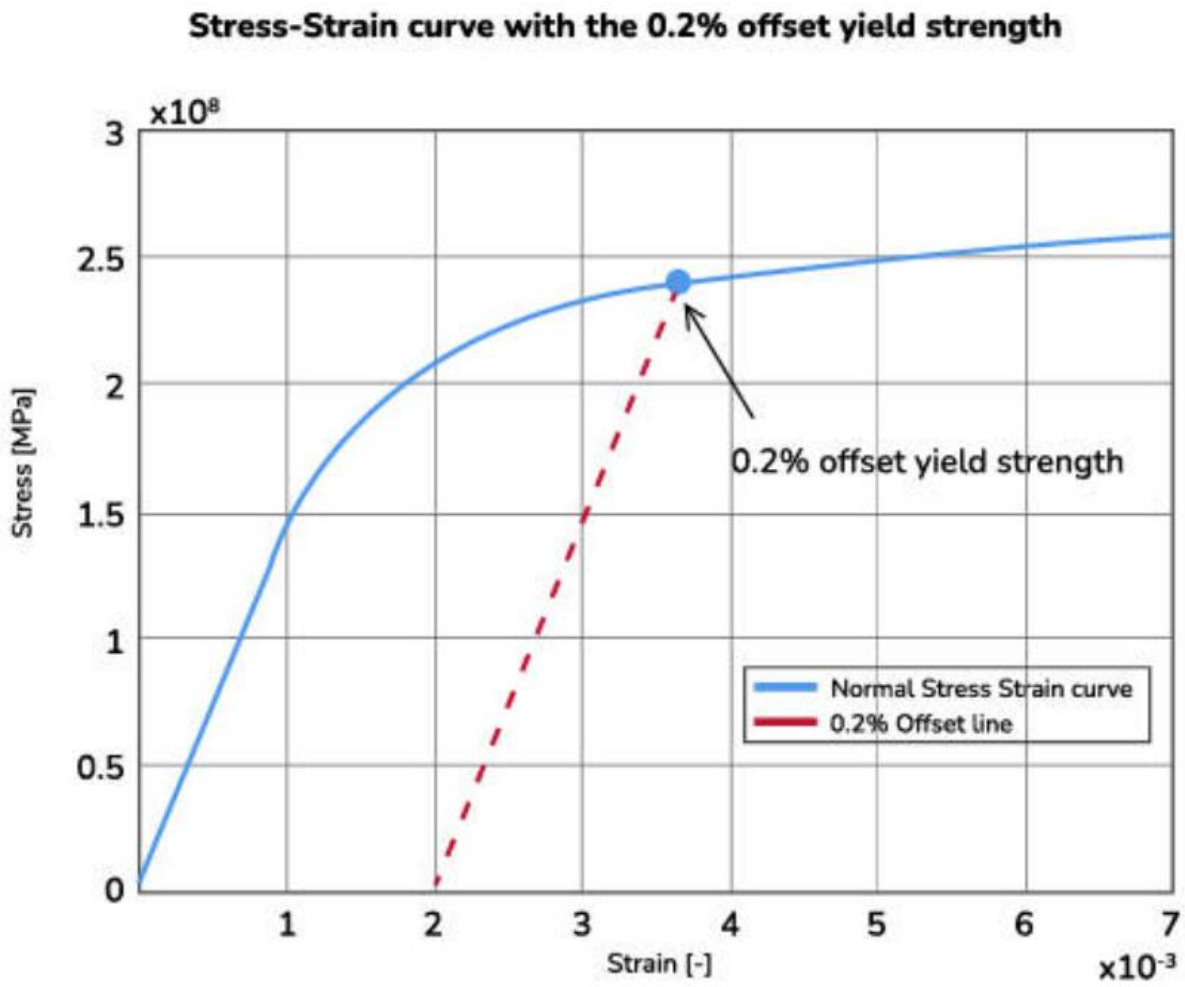

Figure 3.2. The acquirement of 0.2% offset yield stress.

3.6 TEM Foil Preparation

The TEM foils for the next dislocation analysis were extracted from the compressed plastically deformed micro-pillars by using the FEI-PFIB. The extracted TEM foils were perpendicular to the substrate and the slip plane. Therefore, the TEM foils contain the dislocations from the top to the bottom and the foil normal is perpendicular to the

dislocations, which makes further visibility analysis more straightforward. With the well-controlled crystal orientation and TEM foil normal, the dislocation interactions and distribution can be investigated with ease.

It takes caution during the TEM foil preparation procedure to avoid curtaining and re-deposition effects. The preparation steps with details are as follows:

(1) The top surface was tilted to 52°, making it perpendicular to the ion gun. Platinum layer deposition at 0.3 nA and 30 kV was made on the top surface to protect the micro-pillars. The protection layer should be at least 3 μm thick to avoid it being milled out in the subsequent milling steps. (Figure 3.3 (a))

(2) The specimen was tilted to 7° and rotated by $\pm 90°$ for the side surface platinum layer deposition at the same milling condition. These depositions not only protect the pillar itself, but also provide additional anchorage when the TEM foil was welded to the Cu-grid. (Figure 3.3 (b))

(3) After the deposition step, the specimen was again tilted back to $52 \pm 2°$ for rough thinning. The regular cross-section trench was used to mill out the unnecessary material on both sides of the platinum strip and then thin the foil to about 2 μm by using decreasing currents from 60 nA-1 nA. (Figure 3.3 (c))

(4) The specimen was then tilted to 7° to free most of the TEM foil from the substrate by performing a U-cut pattern. The width of pattern is about 1-2 μm to keep most of the pillar, and the depth of milling is 4 μm at 4 nA and 30kV to confirm the cutting is successful (without redeposition). (Figure 3.3 (d))

(5) The attachment between the Omniprobe micromanipulator and the TEM foil was

performed at 0° by Pt deposition. Before the deposition, the Omniprobe approached the foil until it was stable (without notable movement) and they are attached as fast as possible to avoid bending of the foil or probe. Later on, the TEM foil was cut off to fully free it from the bulk sample and lifted out. (Figure 3.3 (e))

(6) The foil is then attached to the Cu-grid at 0°. When the foil approached the Cu-grid, it was attached with the use of Pt deposition. Then the Omniprobe was detached and retracted out. In addition, both sides of the foil need to be attached to reinforce the mechanical fixation and conductivity. (Figure 3.3 (f) and (g))

(7) At the final precision thinning stage, the specimen was tilted to 54°, 2° away from the perpendicular position in order to reduce the non-uniform thickness across the foil. A final cleaning cross-section pattern was applied in this step. The bottom side of the foil was thinned under 1nA and 0.3 nA with an electron beam used to image in-situ. The specimen was tilted +7° away from the perpendicular position and the voltage was decreased from 30 kV to 5 kV for the final cleaning to reduce the excess damage caused by the ion beam.[108] The specimen was rotated by 180° to repeat above step till the foil was thinned to ~200μm, thin enough for the TEM analysis. (Figure 3.3 (h) and (i))

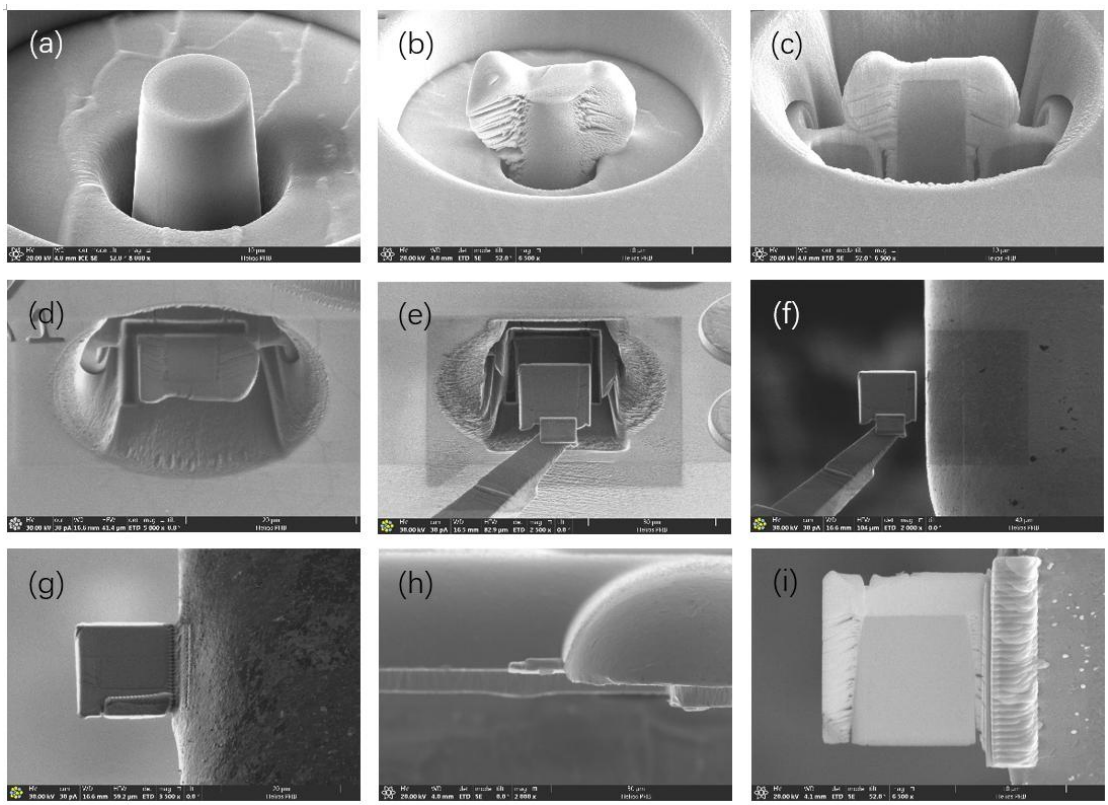

Figure 3.3. Preparation of the TEM foil: (a) a fabricated micro-pillar imaged with the electron beam. (b)Pt coated micro-pillar both on side and top surface, imaged with the electron beam. (c) rough milling of the micro-pillar, in order to reduce the thickness down to 1-2 µm for the further fine, imaged with the electron beam. (d) U-cutting of the micro-pillar, imaged with the electron beam. (e) lifting out of the lamella by using the Omni-probe, imaged with the electron beam. (f) Approaching the TEM lamellae to the copper grid, imaged by ions. (g) Attachment of the TEM lamella onto the copper grid, imaged by ions, and retracting the Omni-probe. (h) The position of the attached lamella on the copper grid, imaged by use of the ion beam. (i) The TEM lamella after fine thinning by small currents, imaged with the electron beam.

3.7 Slip System Analysis

A Tecnai F30 TEM was used to analyse the slip system in the compressed micro-pillars at 300 kV.

The slip system consists of the slip direction (regarded as the dislocation Burgers vector $\boldsymbol{b}$) and the slip plane. At the edge-on condition, the projection of the slip plane becomes a narrow line, combining with the diffraction pattern, the slip plane is parallel to the beam direction and can be determined. The slip direction is parallel to the Burgers vector of dislocations which is on the slip plane, so it can be determined by the invisibility criterion $\boldsymbol{g}\cdot\boldsymbol{b}$ =0.[109] When the TEM condition doesn't reach the invisibility criterion, the dislocations are observed to be dark loops or curves terminating at interfaces (including free surface) in the bright field image. But on the edge-on condition, all dislocations become straight lines, as the slip plane is parallel to the beam direction. The contrast is caused by the bent plane close to the dislocation core, which reduces the intensity of the transmitted beam. At a two-beam condition, only one diffracted beam and transmitted beam are strongly excited, once the diffraction vector $\boldsymbol{g}$ reaches the invisibility criterion $\boldsymbol{g}\cdot\boldsymbol{b}$ =0 ($\boldsymbol{g}$ is perpendicular to the Burgers vector $\boldsymbol{b}$), the dislocations are invisible. If two diffraction vectors $\boldsymbol{g}_1$ and $\boldsymbol{g}_2$ can be found where $\boldsymbol{g}\cdot\boldsymbol{b}$ =0, the Burgers vector $\boldsymbol{b}$ is determined by $\boldsymbol{g}_1 \times \boldsymbol{g}_2$.

3.8 Scanning Electron Microscopy (SEM)

A TESCAN Mira-3 scanning electron microscope (SEM) equipped with a Secondary Electron (SE) detector, Energy Dispersive X-ray (EDX) detector, Back Scattered Electron (BSE) detector, and Electron Back Scattered Diffraction (EBSD) detector is employed for surface morphology characterization, analysis of chemical composition, microstructure characterization, and grain orientation determination, respectively.

Compared to optical microscopy, electron microscopy has a higher resolution due to the very small wavelength of electron beams (~$8.5*10^{-3}$ nm at 20 kV), when comparing with visible light (400-700 nm). The theoretical limitation of electron microscope is determined by the Abbe's equation:

$$d = \lambda/(2nsin\alpha) \qquad (4\text{-}3)$$

Where d is the resolution (the minimum distance between two objects that reveals them as separate entities), λ is the wavelength of imaging radiation, n is the reflective index and α is the half angle of the incident beam which passes through the specimen towards the objective lens. In SEM, the resolution is mainly dependent on the wavelength of the electron beam and higher voltages with higher energies gives a smaller wavelength, resulting in better resolution.

3.9 Energy Dispersive X-ray Spectroscopy (EDX) and Back-scattered Electron (BSE)

The general procedure for preparing the SEM specimens was similar to EBSD mapping. The specimen chemical composition after heat-treatment was analysed by EDX spectroscopy. The electron beam can excite the electrons of the specimen to a higher energy state and then X-rays can be generated when excited electrons lose energy to lower state. The X-rays are collected to plot intensity-x-ray energy curves to determine the elements. For the EDS analyses, an accelerating voltage of 20kV is used to cover x-ray energy for most elements. Furthermore, it is the interaction volume but not the spot size to determine the resolution of EDS.

Back-scattered electron (BSE) imaging is an elastic interaction between electrons and atoms. The atomic number of elements involved in the material affects the intensity of imaging, in

that heavier atoms result in stronger scattering of electrons compared to light atoms. This can help to distinguish different phases. In this project, α phase of Ti-6Al-4V alloy has higher concentration of Al than the β phase, where V is enriched. Thus, the β phase is lighter than the α phase in BSE mode.

3.10 Focus Ion Beam (FIB) and Dual Beam System

The focus ion beam (FIB) system is frequently used for micro- or nano- fabrication, such as micro-pillars, from single crystal or polycrystalline TEM lamellae preparation from the region of interest to micro-sized cross-sectioning or 3-dimensional reconstruction. A dual beam system is combined with a focus ion beam (FIB) and scanning electron beam (SEM) together. In this way, the electron beam is utilized to scan the morphology of the specimen without damaging the sample surface, whereas the ion beam is mainly used to mill micro-pillars from colonies of single crystals for micro-compression, or deposit Pt. In this work, the plasma PFIB/SEM dual beam system with Xe plasma ion source is used to fabricate micro-pillars and prepare TEM foils when the specimen is tilted at 52° that is perpendicular to the ion beam. Comparing to a gallium liquid metal ion source (LMIS), FIB with Xe ion source has a higher milling rate, less implantation, less redeposition, and less lattice defects[110-112]. Normally, high currents like 60 nA at 30kV can rapidly remove materials, and low currents are used to precisely control the details of the geometry and fine polishing of the specimen.

3.11 Transmission Electron Microscopy (TEM)

High energy electrons with a very small wavelength are able to transmit through thin lamellas which are electron transparent, leading to very high resolution. In this approach, the microstructure at micro- or nanoscale can be imaged and analysed. Furthermore, TEM can be used to investigate morphologies, grain boundaries, crystal phases, interfaces, as well as line and planar defects.

In this research, a FEI Tecnai F30 and a FEI Talos F200x TEM are used to study the dislocations after micro-compression and the function of α/β interfaces during the resultant plastic deformation. The investigation of dislocations and α/β interfaces are under two-beam conditions or multiple beam conditions by bright field (BF) or dark field (DF) imaging. In addition, selected area electron diffraction (SAED) is used to determine the zone axis and help to achieve the two-beam conditions, which obey the visibility and invisibility criteria.

Chapter 4 Micro-compression Results

4.1 Introduction

The aim of the present work in this project was to study the effect of the quantity of α/β interfaces (one β fillet has two α/β interfaces) on the mechanical properties during the plastic deformation of micro-compression. In order to achieve it, micro-pillars were prepared using the FIB from a Ti-6Al-4V alloy with two different cooling rates after the heat-treatment. Micro-pillars with various numbers of β fillets, viz. 0 β fillet (single α phase), 1 β fillet (α/β/α sandwich structure), 2 β fillets and ~10 β fillets (multiple β fillets), were prepared. The sizes of micro-pillars are kept at approximate 10μm, 8μm, 5μm and 2μm in diameter with the aspect ratio of 2.

The microstructure, morphology, chemical composition, grain orientation and slip traces after compression were characterised using techniques, including scanning electron microscope (SEM), energy dispersion X-ray spectroscopy (EDX), focus ion beams (FIB), electron back scattered diffraction (EBSD) and a nanoindentation system (Alemnis system).

4.2 Microstructure and Chemical Composition of Ti-6Al-4V

4.2.1 As-received Ti-6Al-4V

SEM-BSE images of the as-received Ti-6Al-4V alloys in Fig. 4.2.1 show a fully-equiaxed microstructure from a low magnification to a high magnification. The α phase is in dark, and the bright area refers to β phase. Because V is a β stabiliser and is heavier than α stabilisers in this alloy.

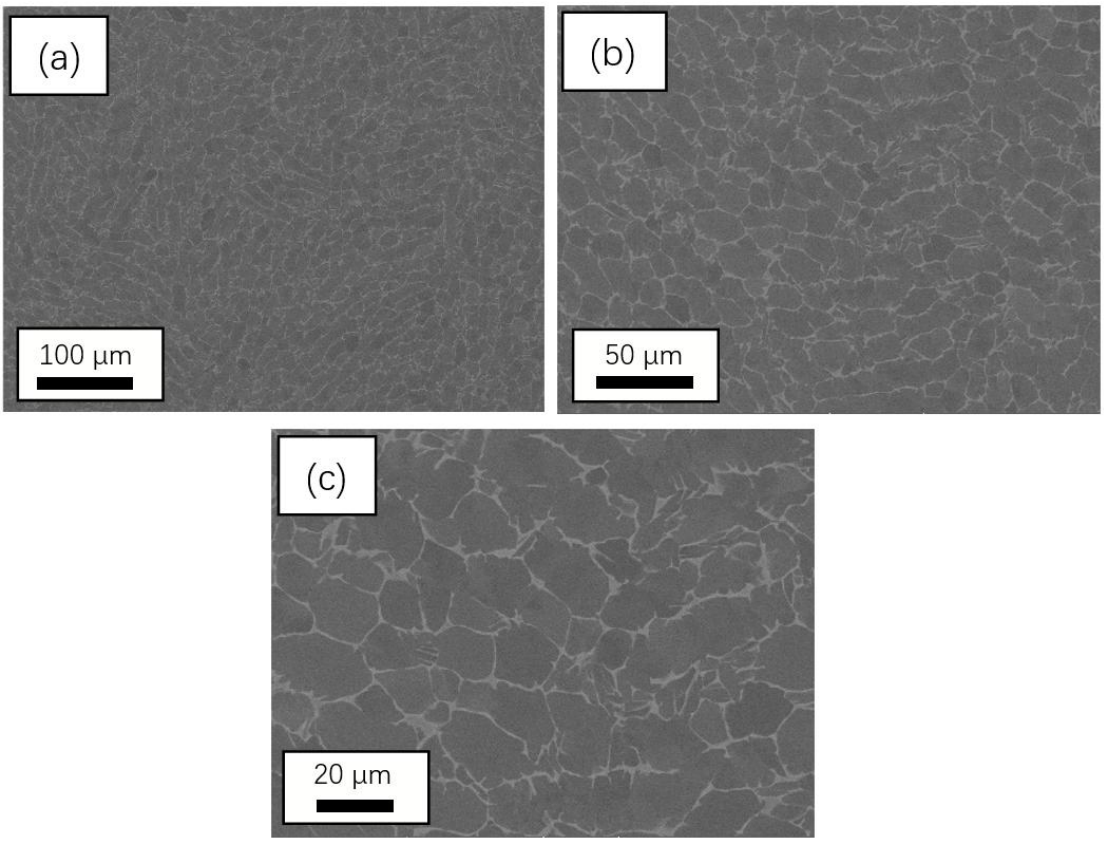

Figure 4.2.1 SEM-BSE images at different magnifications show the morphology of the as-received Ti-6Al-4V with equiaxed microstructure.

4.2.2 Furnace-cooled Ti-6Al-4V Alloys

In Fig. 4.2.2, three SEM-BSE images show the typical fully lamellar micro-structure of the furnace cooled Ti-6Al-4V alloys. Due to the low cooling rate, the β phase has a relatively large spacing (5-10µm).

The chemical composition of furnace-cooled samples is measured through an EDS detector. The results of α phase, β phase and overall materials are recorded in Table 4.2.1. α phase consists of 6.56 (±0.05) % Al, 2.40 (±0.19) % V and 0.22 (±0.16) % Fe in weight percent,

where Al element is enriched. In β phase, there are 1.78 (±0.19)% Al, 23.00 (±0.62)% V and 3.23 (±0.52)% Fe in weight percent. Apparently, V and Fe, which are two kinds of heavy elements, are enriched in β phase. The overall composition of Ti-6Al-4V alloys is 5.8% Al, 4.4% V and 0.4% Fe in weight percent with Ti in balance.

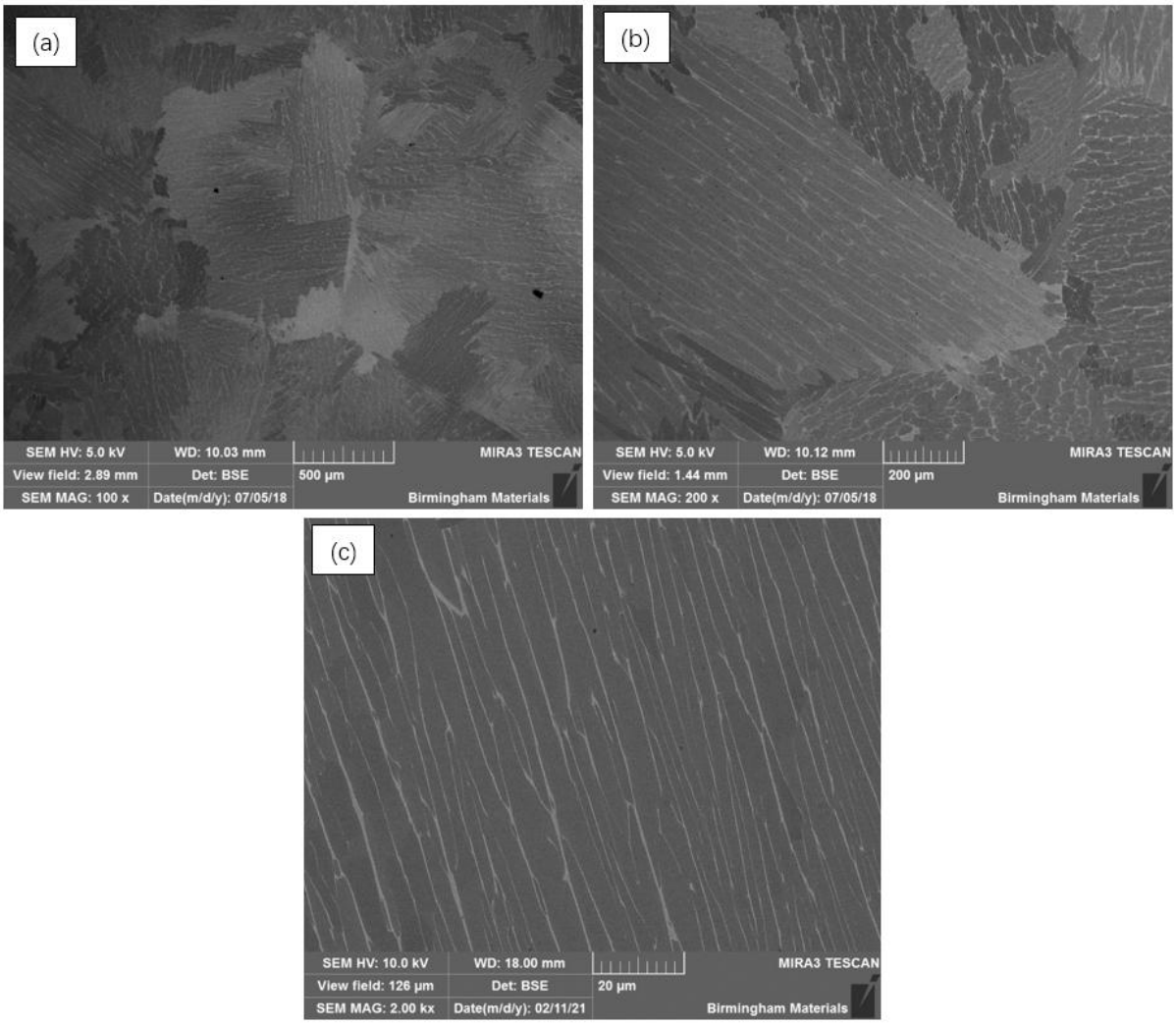

Figure 4.2.2 SEM-BSE images at different magnifications (100x, 200x and 2000x) show the microstructure of the heat-treated Ti-6Al-4V with a furnace cooling method, resulting the fully lamellar microstructure.

4.2.3 Air-cooled Ti-6Al-4V Alloys

Three SEM-BSE images with different magnifications ranging from 200x to 5000x in Fig. 5.2.3 show the microstructure of an air-heat-treated sample during the air-cooling process. With a magnification of 200x in Fig. 4.2.3 (a), it is difficult to observeβ phase due to its narrow shape. With the increase of magnification, β phase in white can be investigated to be 200-300nm in width with spacing of about 1μm among each other in Fig. 4.2.3 (b-c). A clear classical “basketwave” Widmansta¨tten microstructure[113] is shown in Fig. 4.2.3 (c), resulted from a very high cooling rate, in which not enough time is given for either α or β phase to nucleate or grow.

Similar to the furnace-cooled sample, the chemical composition of an air-cooled sample is shown in Table 4.2.1. There are 6.31 (±0.05) % Al, 2.79 (±0.23) % V and 0.17 (±0.12)% Fe in weight percent in α phase. Different from the β phase formed through a furnace-cooling process, β phase of the air-cooled sample has a relative higher concentration of Al, which is 5.54 (±0.47) % and a lower concentration of V and Fe, which is 5.83(±1.37) % and 0.46(±0.13) % respectively. This indicates that during the air-cooling process, there is not enough time for V or Fe element to be enriched in β phase, whereas Al element can’t be enriched from β phase into α phase and finally remains in β phase, due to a very short cooling time.

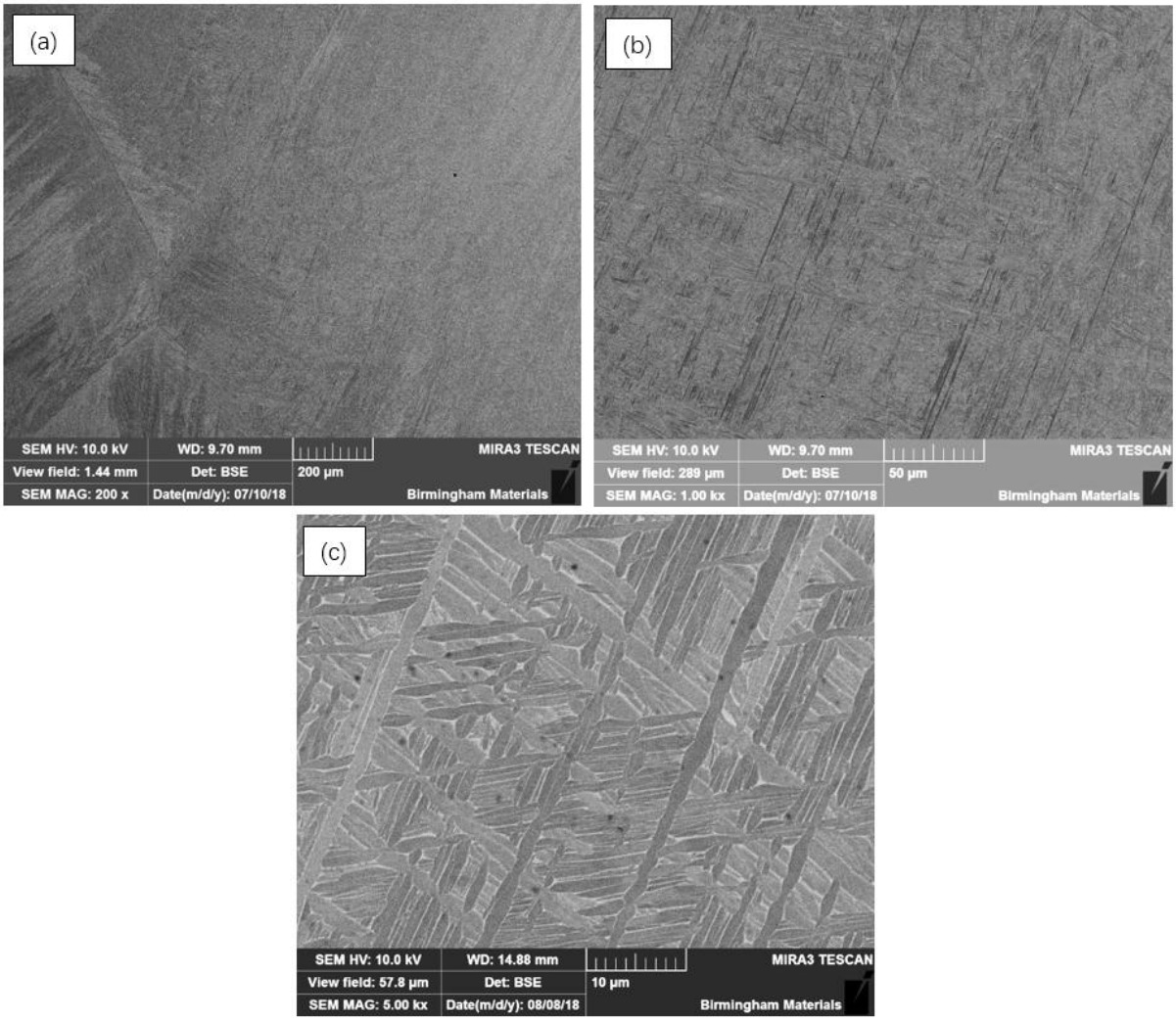

Figure 4.2.3 SEM-BSE images at different magnifications (200x, 1000x and 5000x) show the microstructure of the heat-treated Ti-6Al-4V with an air-cooling method, resulting the fully lamellar microstructure.

Table 4.2.1 Chemical compositions of α, β phases and overall values (wt%) for furnace cooled and air-cooled Ti-6Al-4V alloys.

element		Ti	Al	V	Fe
Furnace cooled	α	Bal. (±0.17)	6.56(±0.05)	2.40(±0.19)	0.22(±0.16)
	β	Bal. (±0.37)	1.78(±0.19)	23.00(±0.62)	3.23(±0.52)
	overall	Bal.	5.8	4.4	0.4
Air cooled	α	Bal. (±0.33)	6.31(±0.05)	2.79(±0.23)	0.17(±0.12)
	β	Bal. (±0.87)	5.54(±0.47)	5.83(±1.37)	0.46(±0.13)
	overall	Bal.	5.9	4.4	0.4

4.3 Calculation of Potential Slip Systems based on EBSD Results

In order to activate the expected slip systems, including prismatic <a_2>, prismatic <a_3>, basal <a_1>, basal <a_3> and pyramidal <a_3> slip system, several grains with specific orientations are selected, meanwhile Schmid factors calculated for different slip systems are obtained and summarized in Table 4.3.1 to Table 4.3.5.

For Grain 1 with an orientation of [18 $\bar{8}$ $\overline{10}$ 1] through furnace-cooling treatment, three main slip systems with high Schmid factors are obtained, as is shown in Table 4.3.1, which are prismatic <a_3>, pyramidal <a_3> and 2nd pyramidal <c+a> slip with a Schmid factor of 0.460, 0.417 and 0.468 respectively. Since the CRSS value of Ti-6Al-4V in different slip systems varies a lot, both CRSS values and Schmid factors are considered for the slip activation. In this case, $\tau_{CRSS}^{prism<a>} < \tau_{CRSS}^{basal<a>} < \tau_{CRSS}^{pyr<a>} < \tau_{CRSS}^{pyr<c+a>}$ and $\tau_{CRSS}^{pyr<c+a>}$, which is approximately

twice the value of $\tau_{CRSS}^{prism<a>}$ according to Table 2.4. However, there is limited difference in the Schmid factors of prismatic <a_3>, pyramidal <a_3> and 2nd pyramidal <c+a> slip. So, the CRSS of prismatic <a_3> slip is more likely to be first reached due to its low value. Thus, in Grain 1 with a loading direction of [18 $\bar{8}$ $\overline{10}$ 1], prismatic <a_3> slip is possible to be activated.

Similarly, in Grain 2-5 with an orientation of [$\bar{6}60\bar{1}$], [$2\bar{1}\bar{1}3$], [$\bar{2}\bar{2}4\bar{9}$] and [$02\bar{2}\bar{1}$], prismatic <a_2>, basal <a_1>, basal <a_3> and pyramidal <a_3> slips are expected to be achieved. The summary of possibly activated slip systems is shown in Table 4.3.6.

Table 4.3.1. Schmid factors of furnace-cooled samples for possible slip systems in the h.c.p structure of Ti-6Al-4V with parameters a = 0.295nm and c = 0.468nm along the loading direction [18 $\bar{8}$ $\bar{1}\bar{0}$ 1]. The Schmid factors of three possible slip systems are highlighted in red.

	Slip system	Schmid factor in [18 $\bar{8}$ $\bar{1}\bar{0}$ 1]		Slip system	Schmid factor in [18 $\bar{8}$ $\bar{1}\bar{0}$ 1]
<a> Basal	(0001) [11$\bar{2}$0]	0.028	<c+a> Pyram. (1st)	(0$\bar{1}$11) [11$\bar{2}$3]	0.020
	(0001) [1$\bar{2}$10]	0.022		(0$\bar{1}$11) [$\bar{1}$2$\bar{1}$3]	0.022
	(0001) [$\bar{2}$110]	0.050		(1$\bar{1}$01) [$\bar{1}$2$\bar{1}$3]	0.196
<a> Prism	(1$\bar{1}$00) [11$\bar{2}$0]	0.460		($\bar{1}$101) [1$\bar{2}$13]	0.146
	(10$\bar{1}$0) [1$\bar{2}$10]	0.397		(01$\bar{1}$1) [1$\bar{2}$13]	0.006
	(01$\bar{1}$0) [$\bar{2}$110]	0.064		($\bar{1}$101) [2$\bar{1}\bar{1}$3]	0.368
<a> Pyram.	(1$\bar{1}$01) [11$\bar{2}$0]	0.391		($\bar{1}$011) [2$\bar{1}\bar{1}$3]	0.396
	($\bar{1}$101) [11$\bar{2}$0]	0.417		(1$\bar{1}$01) [$\bar{2}$113]	0.405
	(10$\bar{1}$1) [1$\bar{2}$10]	0.337		(10$\bar{1}$1) [$\bar{2}$113]	0.437
	($\bar{1}$011) [1$\bar{2}$10]	0.359	<c+a> Pyram. (2nd)	($\bar{1}\bar{1}$22)[11$\bar{2}$3]	0.125
	(01$\bar{1}$1) [$\bar{2}$110]	0.032		(11$\bar{2}$2)[$\bar{1}\bar{1}$23]	0.149
	(0$\bar{1}$11) [$\bar{2}$110]	0.080		($\bar{1}$2$\bar{1}$2)[1$\bar{2}$13]	0.078
<c+a> Pyram. (1st)	(10$\bar{1}$1) [$\bar{1}\bar{1}$23]	0.257		(1$\bar{2}$12)[$\bar{1}$2$\bar{1}$3]	0.097
	(01$\bar{1}$1) [$\bar{1}\bar{1}$23]	0.011		(2$\bar{1}\bar{1}$2)[$\bar{2}$113]	0.468
	($\bar{1}$011) [11$\bar{2}$3]	0.205		($\bar{2}$112)[2$\bar{1}\bar{1}$3]	0.425

Table 4.3.2. Schmid factors of furnace-cooled samples for possible slip systems in the h.c.p structure of Ti-6Al-4V with parameters a = 0.295nm and c = 0.468nm along the loading direction [$\bar{6}60\bar{1}$]. The Schmid factors of three possible slip systems are highlighted in red.

	Slip system	Schmid factor in [$\bar{6}60\bar{1}$]		Slip system	Schmid factor in [$\bar{6}60\bar{1}$]
<a> Basal	(0001) [$11\bar{2}0$]	0.016	<c+a> Pyram. (1st)	($0\bar{1}11$) [$11\bar{2}3$]	0.090
	(0001) [$1\bar{2}10$]	0.146		($0\bar{1}11$) [$\bar{1}2\bar{1}3$]	0.124
	(0001) [$\bar{2}110$]	0.161		($1\bar{1}01$) [$\bar{1}2\bar{1}3$]	0.261
<a> Prism	($1\bar{1}00$) [$11\bar{2}0$]	0.085		($\bar{1}101$) [$1\bar{2}13$]	0.450
	($10\bar{1}0$) [$1\bar{2}10$]	0.455		($01\bar{1}1$) [$1\bar{2}13$]	0.161
	($01\bar{1}0$) [$\bar{2}110$]	0.370		($\bar{1}101$) [$2\bar{1}\bar{1}3$]	0.486
<a> Pyram.	($1\bar{1}01$) [$11\bar{2}0$]	0.082		($\bar{1}011$) [$2\bar{1}\bar{1}3$]	0.257
	($\bar{1}101$) [$11\bar{2}0$]	0.067		($1\bar{1}01$) [$\bar{2}113$]	0.305
	($10\bar{1}1$) [$1\bar{2}10$]	0.469		($10\bar{1}1$) [$\bar{2}113$]	0.188
	($\bar{1}011$) [$1\bar{2}10$]	0.329	<c+a> Pyram. (2nd)	($\bar{1}\bar{1}22$)[$11\bar{2}3$]	0.125
	($01\bar{1}1$) [$\bar{2}110$]	0.247		($11\bar{2}2$)[$\bar{1}\bar{1}23$]	0.149
	($0\bar{1}11$) [$\bar{2}110$]	0.402		($\bar{1}2\bar{1}2$)[$1\bar{2}13$]	0.078
<c+a> Pyram. (1st)	($10\bar{1}1$) [$\bar{1}\bar{1}23$]	0.062		($1\bar{2}12$)[$\bar{1}2\bar{1}3$]	0.097
	($01\bar{1}1$) [$\bar{1}\bar{1}23$]	0.030		($2\bar{1}\bar{1}2$)[$\bar{2}113$]	0.468
	($\bar{1}011$) [$11\bar{2}3$]	0.082		($\bar{2}112$)[$2\bar{1}\bar{1}3$]	0.425

Table 4.3.3. Schmid factors of air-cooled samples for possible slip systems in the h.c.p structure of Ti-6Al-4V with parameters a = 0.295nm and c = 0.468nm along the loading direction [$2\bar{1}\bar{1}3$]. The Schmid factors of three possible slip systems are highlighted in red.

	Slip system	Schmid factor in [$2\bar{1}\bar{1}3$]		Slip system	Schmid factor in [$2\bar{1}\bar{1}3$]
<a> Basal	(0001) [$11\bar{2}0$]	0.199	<c+a> Pyram. (1st)	($0\bar{1}11$) [$11\bar{2}3$]	0.370
	(0001) [$1\bar{2}10$]	0.242		($0\bar{1}11$) [$\bar{1}2\bar{1}3$]	0.251
	(0001) [$\bar{2}110$]	0.441		($1\bar{1}01$) [$\bar{1}2\bar{1}3$]	0.468
<a> Prism	($1\bar{1}00$) [$11\bar{2}0$]	0.107		($\bar{1}101$) [$1\bar{2}13$]	0.006
	($10\bar{1}0$) [$1\bar{2}10$]	0.122		($01\bar{1}1$) [$1\bar{2}13$]	0.338
	($01\bar{1}0$) [$\bar{2}110$]	0.015		($\bar{1}101$) [$2\bar{1}\bar{1}3$]	0.007
<a> Pyram.	($1\bar{1}01$) [$11\bar{2}0$]	0.189		($\bar{1}011$) [$2\bar{1}\bar{1}3$]	0.032
	($\bar{1}101$) [$11\bar{2}0$]	0.002		($1\bar{1}01$) [$\bar{2}113$]	0.367
	($10\bar{1}1$) [$1\bar{2}10$]	0.223		($10\bar{1}1$) [$\bar{2}113$]	0.356
	($\bar{1}011$) [$1\bar{2}10$]	0.009	<c+a> Pyram. (2nd)	($\bar{1}\bar{1}22$)[$11\bar{2}3$]	0.221
	($01\bar{1}1$) [$\bar{2}110$]	0.198		($11\bar{2}2$)[$\bar{1}\bar{1}23$]	0.393
	($0\bar{1}11$) [$\bar{2}110$]	0.224		($\bar{1}2\bar{1}2$)[$1\bar{2}13$]	0.192
<c+a> Pyram. (1st)	($10\bar{1}1$) [$\bar{1}\bar{1}23$]	0.475		($1\bar{2}12$)[$\bar{1}2\bar{1}3$]	0.400
	($01\bar{1}1$) [$\bar{1}\bar{1}23$]	0.232		($2\bar{1}\bar{1}2$)[$\bar{2}113$]	0.402
	($\bar{1}011$) [$11\bar{2}3$]	0.028		($\bar{2}112$)[$2\bar{1}\bar{1}3$]	0.022

Table 4.3.4. Schmid factors of air-cooled samples for possible slip systems in the h.c.p structure of Ti-6Al-4V with parameters a = 0.295nm and c = 0.468nm along the loading direction [$\bar{2}\bar{2}49$]. The Schmid factors of three possible slip systems are highlighted in red.

	Slip system	Schmid factor in [$\bar{2}\bar{2}49$]		Slip system	Schmid factor in [$\bar{2}\bar{2}49$]
<a> Basal	(0001) [$11\bar{2}0$]	0.361	<c+a> Pyram. (1st)	($0\bar{1}11$) [$11\bar{2}3$]	0.133
	(0001) [$1\bar{2}10$]	0.195		($0\bar{1}11$) [$\bar{1}2\bar{1}3$]	0.120
	(0001) [$\bar{2}110$]	0.165		($1\bar{1}01$) [$\bar{1}2\bar{1}3$]	0.378
<a> Prism	($1\bar{1}00$) [$11\bar{2}0$]	0.007		($\bar{1}101$) [$1\bar{2}13$]	0.304
	($10\bar{1}0$) [$1\bar{2}10$]	0.070		($01\bar{1}1$) [$1\bar{2}13$]	0.497
	($01\bar{1}0$) [$\bar{2}110$]	0.063		($\bar{1}101$) [$2\bar{1}\bar{1}3$]	0.400
<a> Pyram.	($1\bar{1}01$) [$11\bar{2}0$]	0.166		($\bar{1}011$) [$2\bar{1}\bar{1}3$]	0.132
	($\bar{1}101$) [$11\bar{2}0$]	0.179		($1\bar{1}01$) [$\bar{2}113$]	0.290
	($10\bar{1}1$) [$1\bar{2}10$]	0.155		($10\bar{1}1$) [$\bar{2}113$]	0.499
	($\bar{1}011$) [$1\bar{2}10$]	0.032	<c+a> Pyram. (2nd)	($\bar{1}\bar{1}22$)[$11\bar{2}3$]	0.157
	($01\bar{1}1$) [$\bar{2}110$]	0.134		($11\bar{2}2$)[$\bar{1}\bar{1}23$]	0.468
	($0\bar{1}11$) [$\bar{2}110$]	0.024		($\bar{1}2\bar{1}2$)[$1\bar{2}13$]	0.446
<c+a> Pyram. (1st)	($10\bar{1}1$) [$\bar{1}\bar{1}23$]	0.416		($1\bar{2}12$)[$\bar{1}2\bar{1}3$]	0.277
	($01\bar{1}1$) [$\bar{1}\bar{1}23$]	0.425		($2\bar{1}\bar{1}2$)[$\bar{2}113$]	0.439
	($\bar{1}011$) [$11\bar{2}3$]	0.149		($\bar{2}112$)[$2\bar{1}\bar{1}3$]	0.296

Table 4.3.5. Schmid factors of air-cooled samples for possible slip systems in the h.c.p structure of Ti-6Al-4V with parameters a = 0.295nm and c = 0.468nm along the loading direction [$02\bar{2}\bar{1}$]. The Schmid factors of three possible slip systems are in red.

	Slip system	Schmid factor in [$02\bar{2}\bar{1}$]		Slip system	Schmid factor in [$02\bar{2}\bar{1}$]
<a> Basal	(0001) [$11\bar{2}0$]	0.221	<c+a> Pyram. (1st)	($0\bar{1}11$) [$11\bar{2}3$]	0.167
	(0001) [$1\bar{2}10$]	-0.250		($0\bar{1}11$) [$\bar{1}2\bar{1}3$]	0.220
	(0001) [$\bar{2}110$]	0.029		($1\bar{1}01$) [$\bar{1}2\bar{1}3$]	0.143
<a> Prism	($1\bar{1}00$) [$11\bar{2}0$]	0.437		($\bar{1}101$) [$1\bar{2}13$]	0.254
	($10\bar{1}0$) [$1\bar{2}10$]	0.341		($01\bar{1}1$) [$1\bar{2}13$]	0.496
	($01\bar{1}0$) [$\bar{2}110$]	0.096		($\bar{1}101$) [$2\bar{1}\bar{1}3$]	0.106
<a> Pyram.	($1\bar{1}01$) [$11\bar{2}0$]	0.490		($\bar{1}011$) [$2\bar{1}\bar{1}3$]	0.141
	($\bar{1}101$) [$11\bar{2}0$]	0.278		($1\bar{1}01$) [$\bar{2}113$]	0.118
	($10\bar{1}1$) [$1\bar{2}10$]	0.179		($10\bar{1}1$) [$\bar{2}113$]	0.038
	($\bar{1}011$) [$1\bar{2}10$]	0.419	<c+a> Pyram. (2nd)	($\bar{1}\bar{1}22$)[$11\bar{2}3$]	0.139
	($01\bar{1}1$) [$\bar{2}110$]	0.071		($11\bar{2}2$)[$\bar{1}\bar{1}23$]	0.329
	($0\bar{1}11$) [$\bar{2}110$]	0.098		($\bar{1}2\bar{1}2$)[$1\bar{2}13$]	0.417
<c+a> Pyram. (1st)	($10\bar{1}1$) [$\bar{1}\bar{1}23$]	0.134		($1\bar{2}12$)[$\bar{1}2\bar{1}3$]	0.202
	($01\bar{1}1$) [$\bar{1}\bar{1}23$]	0.458		($2\bar{1}\bar{1}2$)[$\bar{2}113$]	0.044
	($\bar{1}011$) [$11\bar{2}3$]	0.082		($\bar{2}112$)[$2\bar{1}\bar{1}3$]	0.020

Table 4.3.6. Summary of furnace cooled and air-cooled samples for possible slip systems in the h.c.p structure of Ti-6Al-4V with parameters a = 0.295nm and c = 0.468nm with different loading directions.

	Grain 1	Grain 2	Grain 3	Grain 4	Grain 5
Loading direction	[18 $\bar{8}$ $\bar{10}$ 1]	[$\bar{6}60\bar{1}$]	[$2\bar{1}\bar{1}3$]	[$\bar{2}\bar{2}49$]	[$02\bar{2}\bar{1}$]
Slip system	prismatic $<a_3>$	prismatic $<a_2>$	basal $<a_1>$	basal $<a_3>$	pyramidal $<a_3>$

4.4 Micro pillars Containing 0, 1, and 2 β Fillets Oriented for Prismatic $<a_3>$ Slip

This part is to study the effect of pillar size and the number of α/β interfaces (or β fillets) on the CRSS value, step size and slip band distribution of prismatic $<a_3>$ slip with a Schmid factor of 0.460. All pillars are fabricated from Grain 1 with a loading direction of [18 $\bar{8}$ $\bar{10}$ 1]. Each micro-pillar contains one β fillet.

4.4.1 Surface Morphology of the Deformed Micro-pillars and the Corresponding Stress-strain Curves

The micro-compression tests of pillars with different β fillets (0, 1 and 2) as well as different sizes (10μm, 8μm and 5μm in top diameter) are compressed to strains ranging from 4% to 7% in a displacement-controlled system. Fig. 4.4.1 to Fig. 4.4.3 show the surface morphology of micro-pillars before and after the compression. Fig. 4.4.4 shows a comparison of the surface morphology of slip bands with different α/β interfaces (or β fillets) and sizes. Fig. 4.4.5 indicates the slip trace transmission from α phase into β phase. Fig. 4.4.6 to Fig. 4.4.8

show the true stress-strain curves with different α/β interfaces (or β fillets) and sizes. The yield stress and CRSS values obtained from 0.2% proof point are summarized in Table 4.4.1.

From Fig. 4.4.1 to Fig. 4.4.3, all slip bands from prismatic planes are shown, among which β phase is indicated by orange dash lines and slip bands are shown by red arrows. For a single α phase with 0 β fillet micro-pillar, slip bands with a large step size and a limited number can be investigated after compression in Fig. 4.4.1. Also, one set of slip bands dominate the plastic deformation indicated as red arrows, which distribute in a limited area. For a α/β/α micro-structure with 1 β fillet, two sets of slip bands can be observed in SEM images, whose step size decreases dramatically, and there is a large increasement of the number of slip bands across the pillars, when introducing 1 β fillets into a single α phase, as is shown in Fig. 4.4.2. Furthermore, when the number of β fillets increases to 2, Fig. 4.4.3 shows that only one set of slip bands appears with a small step size and a homogeneous distribution across the pillars, similar to the pillars containing 1 β fillet. A clear comparison of the surface morphology of micro-pillars with different numbers of β fillets is given in Fig. 4.4.4 at a high magnification. However, there is no big difference among surface morphologies with different sizes. The size effect on step size and the distribution of slip bands is limited.

Fig. 4.4.5 shows the transmission of slip bands from α phase into β phase. When one slip band occurs in α phase and encounters a α/β interface, it splits into two in β phase, which activates the $<b_1>$ and $<b_2>$ slip in β phase, as is indicated by red arrows.

Stress-strain curves obtained in Fig. 4.4.6 to Fig. 4.4.8 are non-linear at the elastic stage, which is because of the misalignment between the pillar top surface and the flat punch. Additionally, the slopes of loading and unloading parts during elastic deformation are not exactly the same, since the geometrically necessary dislocations (GND) are pre-existing and move during loading. Stress-strain curves with different β fillets (0, 1 and 2) and different

sizes (10μm, 8μm and 5μm in top diameter) are shown in Fig. 4.4.6 to Fig. 4.4.8, which have similar shapes with a very low strain hardening rate. Small load drops can be investigated during plastic deformation. The effect of the number and size of α/βinterfaces on yield stress is limited when the number of β fillets changes from 0 to 2.

More accurate values of the average yield stress (0.2% proof stress) and CRSS are obtained. For pillars deformed in a single α phase (with 0 β fillet), the average yield stresses (0.2% proof stress) are 923 (±14) MPa and 837 (±58) MPa for 8μm and 5μm micro-pillars, corresponding to CRSS values of 424 (±7) MPa and 385 (±27) MPa respectively. For micro-pillars deformed in a α/β/α microstructure (with 1 β fillet), the average yield stresses (0.2% proof stress) are 840 (±24) MPa, 895 (±61) MPa and 960 (±14) MPa for 10μm, 8μm and 5μm micro-pillars, corresponding to CRSS values of 387 (±11) MPa, 412 (±28) MPa and 442 (±34) MPa, respectively. For micro- pillars in a α/β/α/β/α microstructure (with 2 β fillets), the average yield stresses (0.2% proof stress) are 941 (±21) MPa, 967 (±14) MPa and 992 (±33) MPa for 10μm, 8μm and 5μm micro-pillars, corresponding to a CRSS values of 433 (±9) MPa, 445 (±6) MPa and 456 (±15) MPa, respectively. All yield stresses and CRSS values are listed in Table 4.4.1

The mean yield stress and the CRSS values measured from the micro-pillars of 8 μm in top diameter are higher than those measured from the 5 μm sized pillars. This observation is different from literature reports. The reason for this abnormal phenomenon is unknown and more repeated tests under well-controlled experimental conditions would be needed to reassure the results before a concrete conclusion can be drawn.

In addition, based on the stress-strain curves in Fig. 4.4.7 (a), pillar 1 is slightly stiffer than pillar 2 and 3. For pillar 2 and 3, it can be investigated that in Fig. 4.4.8 (b) and (c) there is only one β fillet inside a pillar. However, at the edge of pillar 1, there is extra small part of

second β fillet involved in the pillar, as shown in Fig. 4.4.8 (a). Therefore, more phase boundaries exist in pillar 1 that makes the pillar stiffer. Since the β fillet is very thin, the effect of β phase volume fraction on the strength reduction is weak enough.

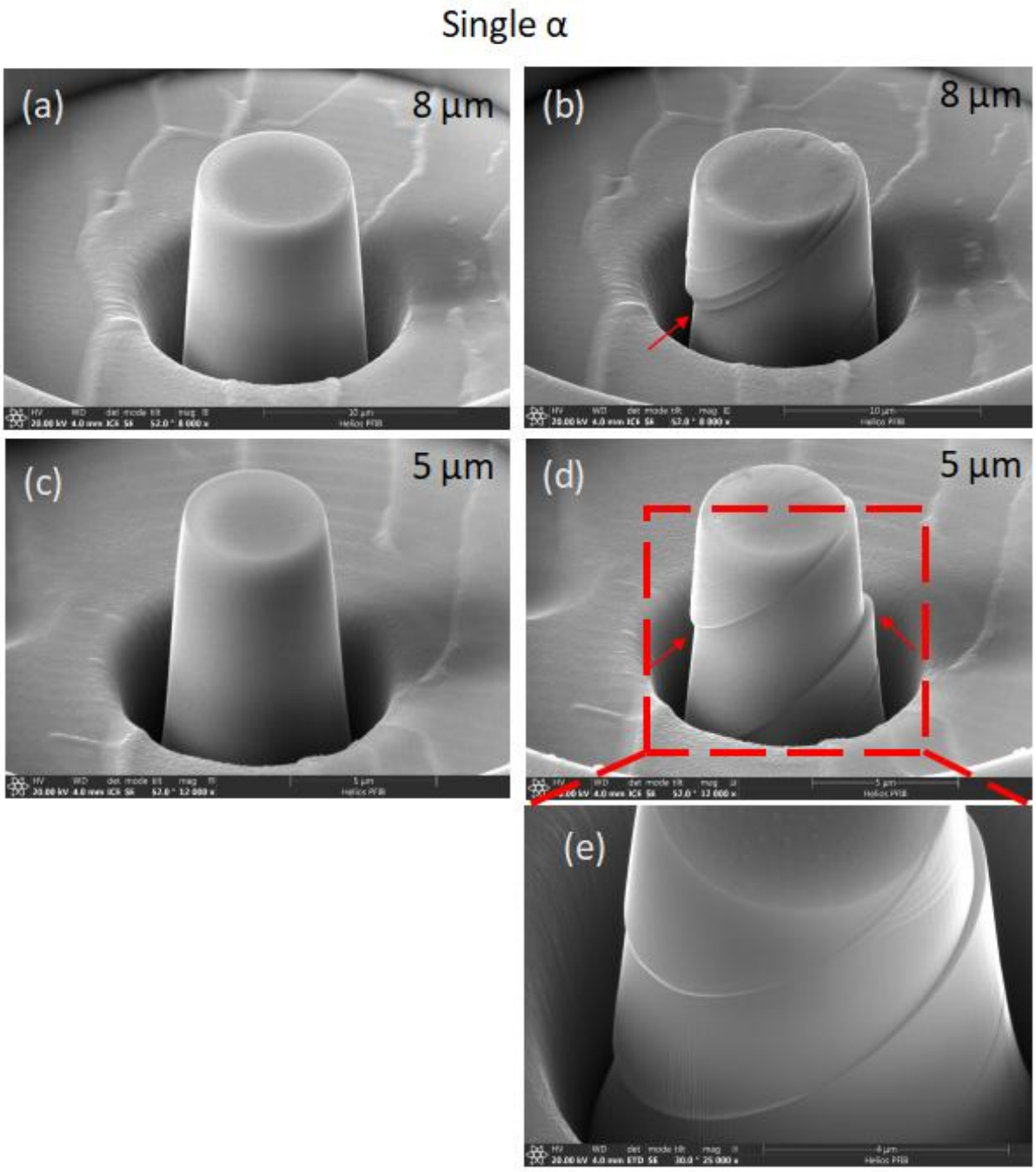

Fig. 4.4.1 SEM images of surface morphology before and after micro-compression from 8μm and 5μm micro-pillars in a single α phase without β phase along the direction of [18 $\bar{8}$ $\bar{10}$ 1]

for prismatic <a_3> slip. (a) and (c) are the micro-pillar images of 8μm and 5μm pillars before compression, while (b) and (d) are the images of 8μm and 5μm pillars after compression with about 6% of strain. (e) is the image with larger magnification at tilting angle of 30°, showing the complete slip trace without collision with the surrounding walls. All images are taken at a tilted angle of 52° and large slip steps are indicated by red arrows.

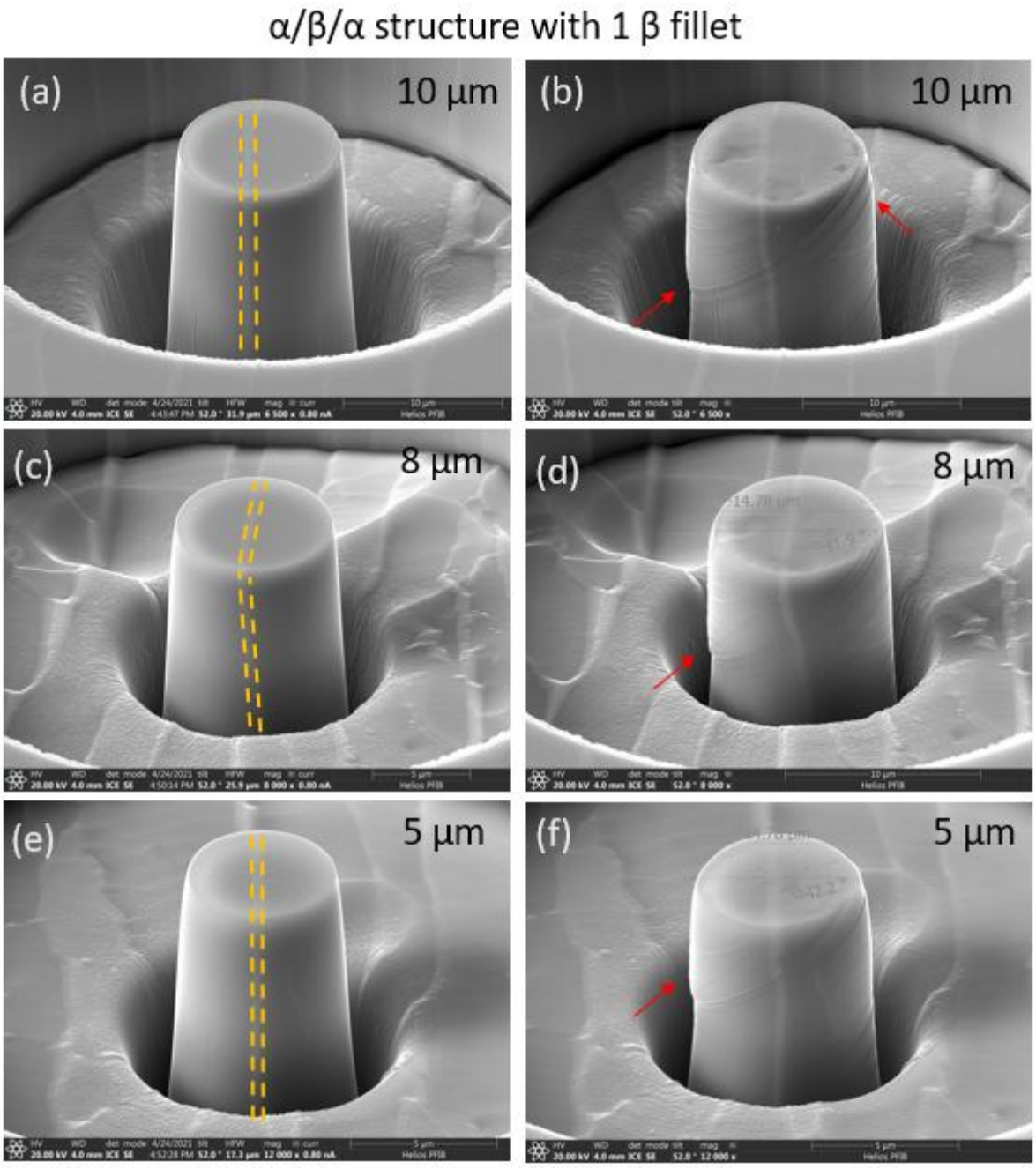

Fig. 4.4.2 SEM images of surface morphology before and after micro-compression from 10µm, 8µm and 5µm micro-pillars in α/β/α micro-structure with 1 β phase along the direction of $[18\ \bar{8}\ \bar{10}\ 1]$ *for prismatic <a_3> slip (β phase is indicated by orange dash lines). (a), (c)and (e) are the micro-pillar images of 10µm, 8µm and 5µm pillars before compression, while (b), (d) and (f) are the images of 10µm, 8µm and 5µm pillars after compression with*

about 6% of strain. All images are taken at tilted angle of 52° and small slip steps are indicated by red arrows.

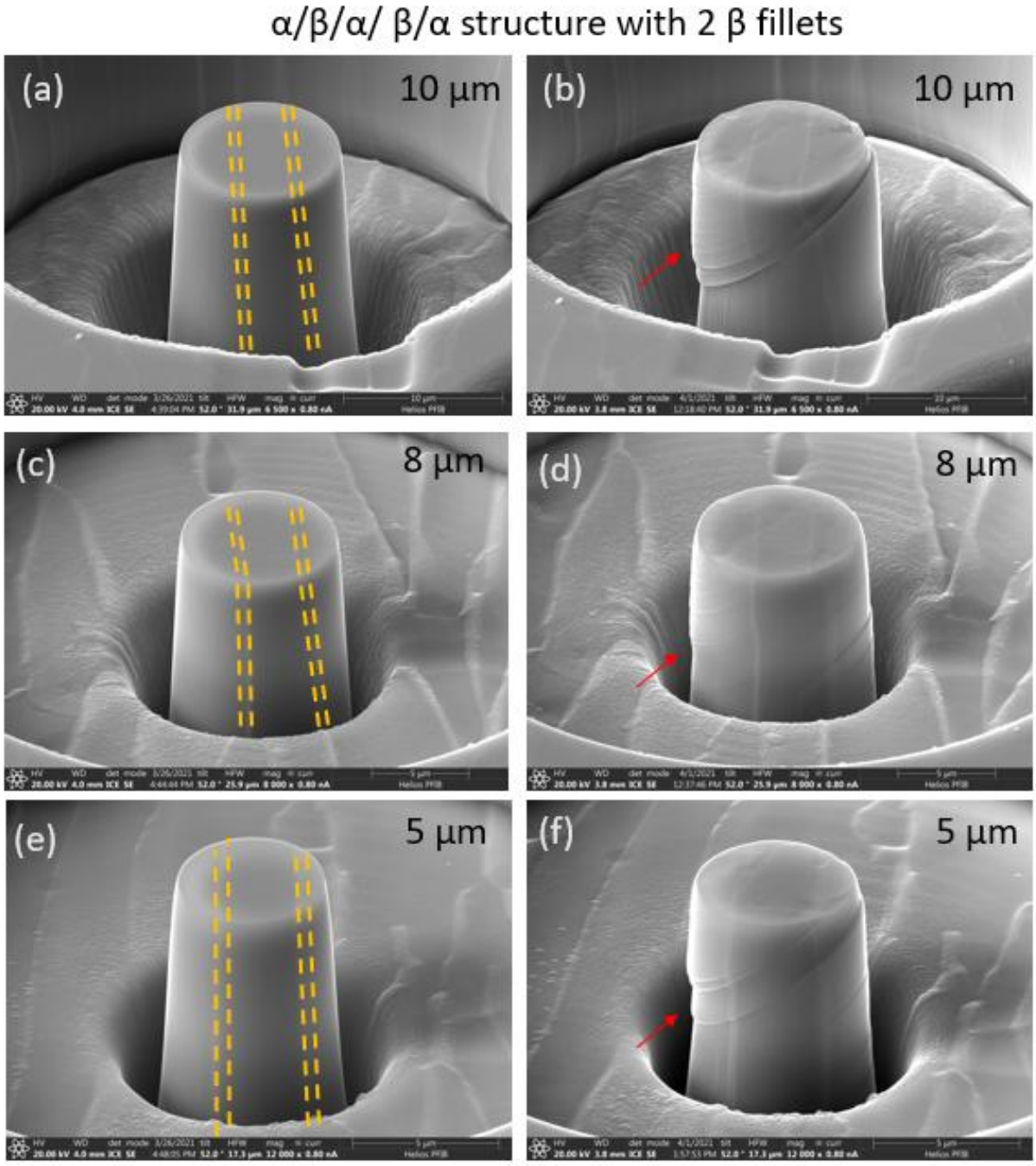

Fig. 4.4.3 SEM images of surface morphology before and after micro-compression from 10μm, 8μm and 5μm micro-pillars in a α/β/α/β/α micro-structure with 2 β phases along the direction of $[18\ \bar{8}\ \bar{10}\ 1]$ *for prismatic* $<a_3>$ *slip (β phase is indicated by orange dash lines). (a), (c)and (e) are the micro-pillar images of 10μm, 8μm and 5μm pillars before compression, while (b), (d) and (f) are the images of 10μm, 8μm and 5μm pillars after compression with about 6% of strain.*

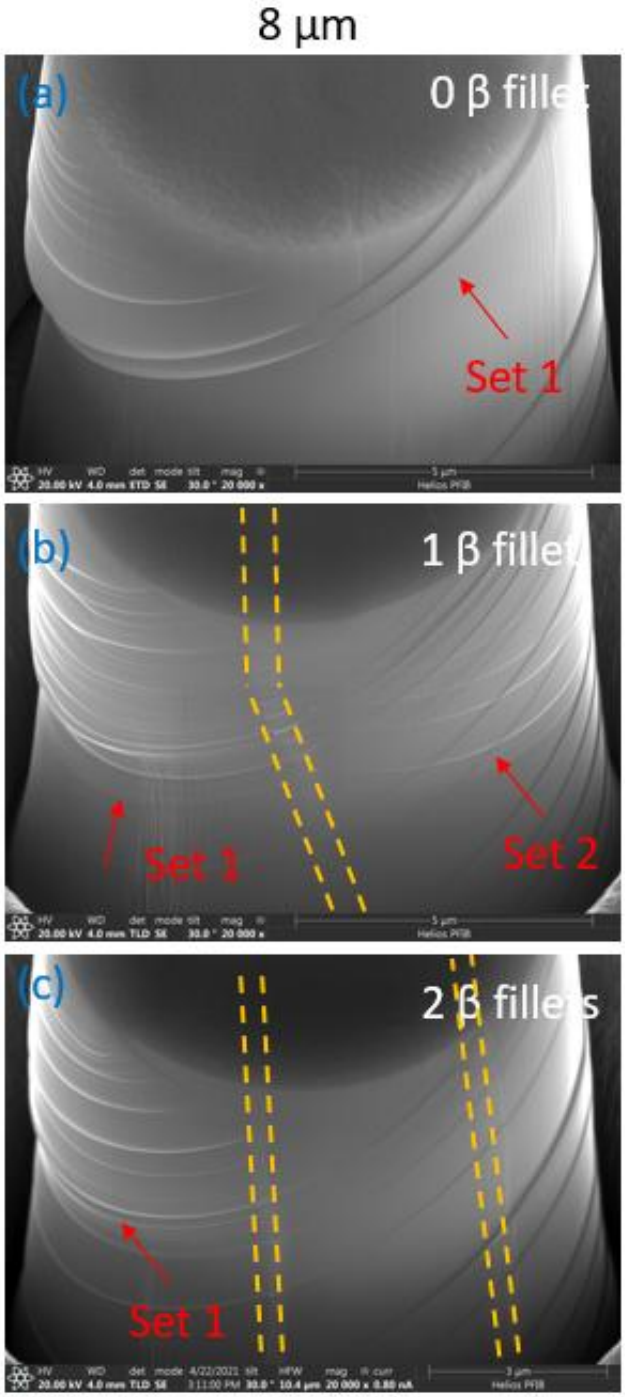

Fig. 4.4.4 SEM images of surface morphology after micro-compression from 0, 1 and 2 β fillets pillars corresponding to single α phase, α/β/α micro-structure, and α/β/α/β/α micro-structure, with the same size of 8µm in top diameter along $[18\ \bar{8}\ \bar{10}\ 1]$ *direction for prismatic* $\langle a_3 \rangle$ *slip (β phase is indicated by orange dash lines). All imaged are taken at 30° tilted angle and small slip steps are indicated by red arrows.*

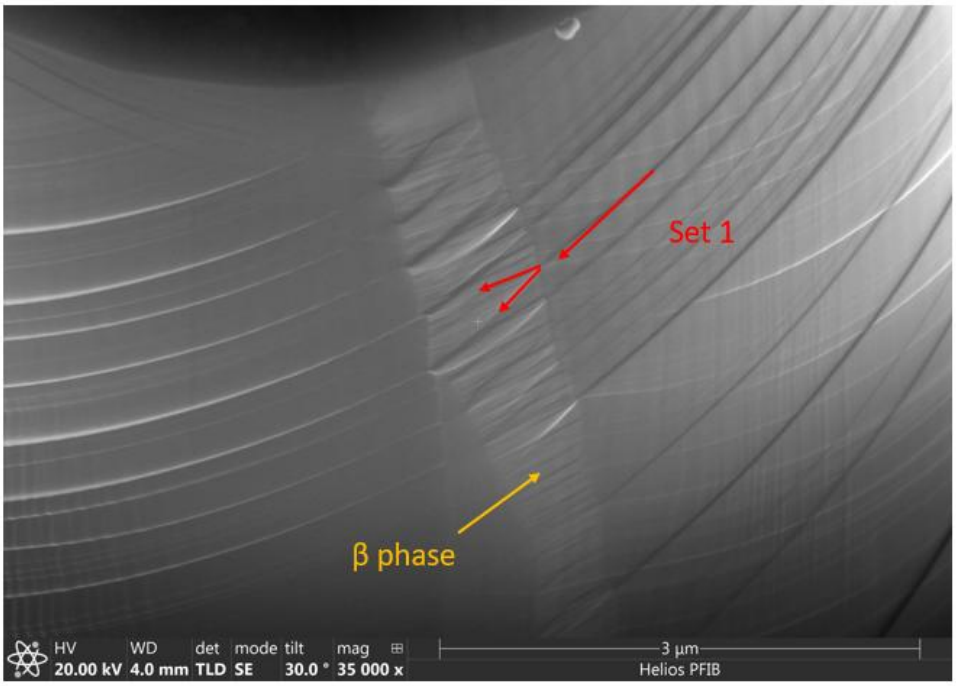

Fig. 4.4.5 SEM images of surface morphology after micro-compression at high magnification along the direction of [18 $\bar{8}$ $\bar{10}$ 1] *for prismatic <a_3> slip. Set one of the slip traces as prismatic <a_3> slip, which activates two sets of slip traces in β phase.*

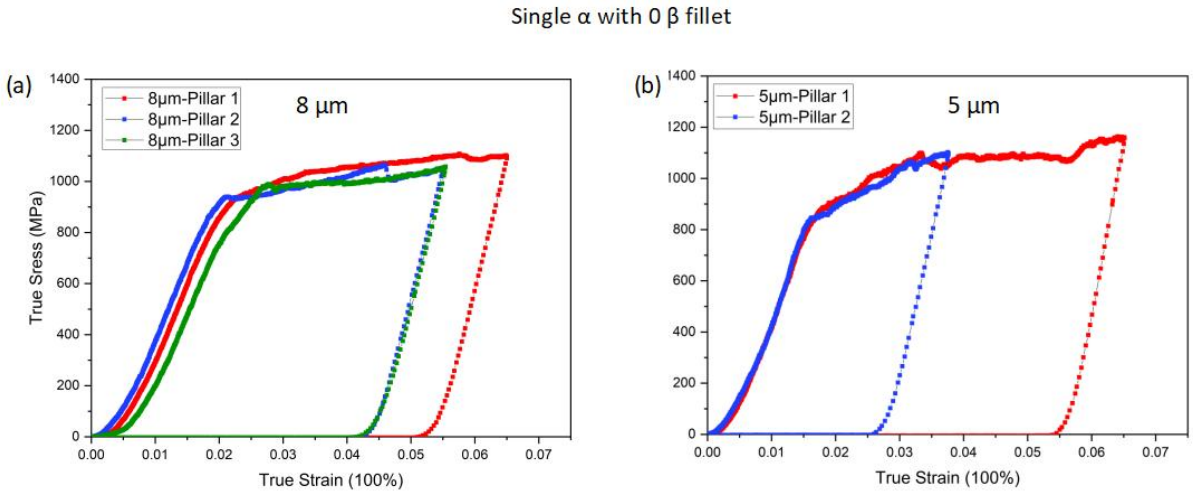

Fig. 4.4.6 Stress- strain curves after micro-compression of single α phase Ti-6Al-4V alloy for prismatic <a_3> slip: (a) 8 µm in diameter; (b) 5 µm in diameter.

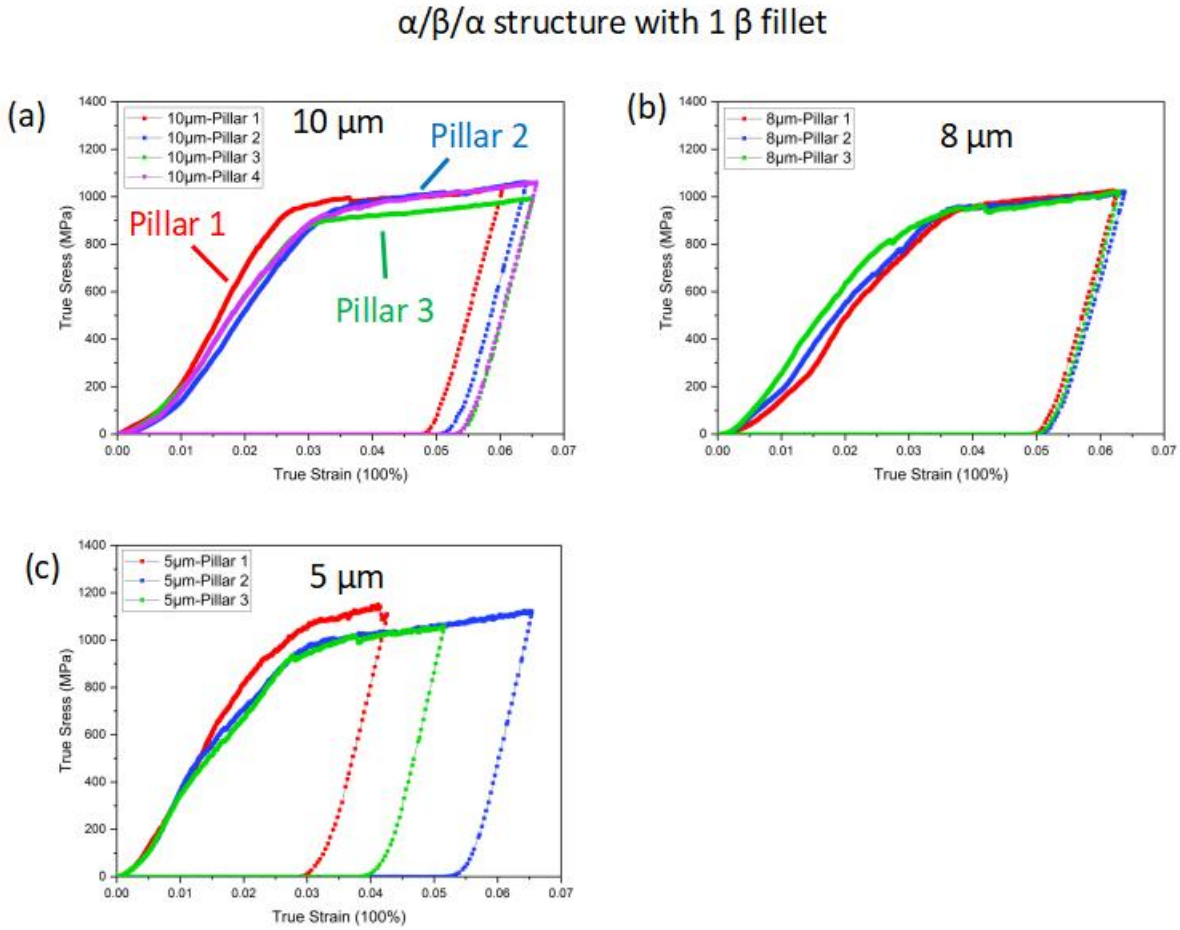

Fig. 4.4.7 Stress- strain curves after micro-compression of α/β/α micro-structures with 1 β phase fillet for prismatic <a_3> slip: (a) 10 µm in diameter; (b) 8 µm in diameter; (c) 5 µm in diameter.

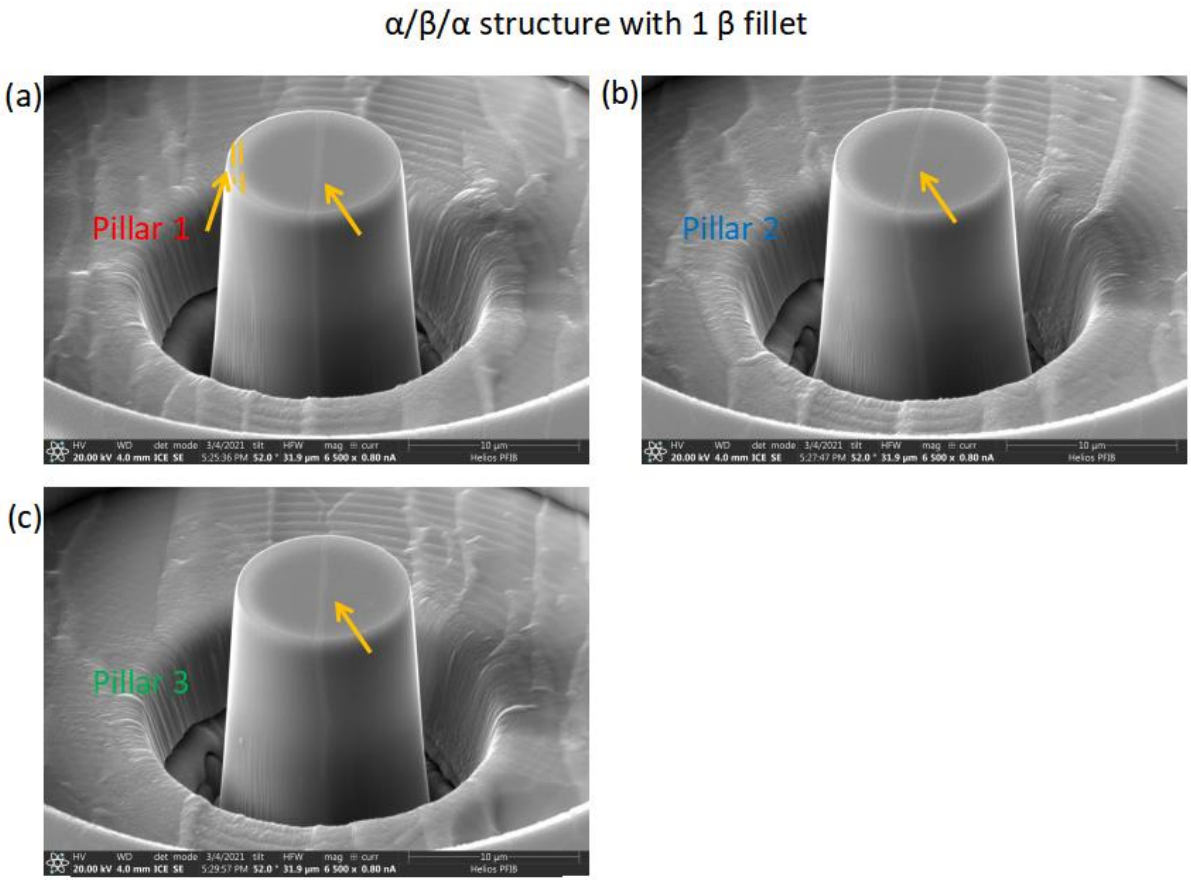

Fig. 4.4.8 SEM images of micro-pillars containing 1 β fillet with the diameter of 10 μm, corresponding to stress-strain curves in Figure 5.4.7 (a) for Pillar 1-3. Yellow arrows and dashed lines refer to β phase. (a) at the left side, there is extra small part of second β fillet in pillar 1, (b-c) only one β fillet involved in pillar 2 and 3.

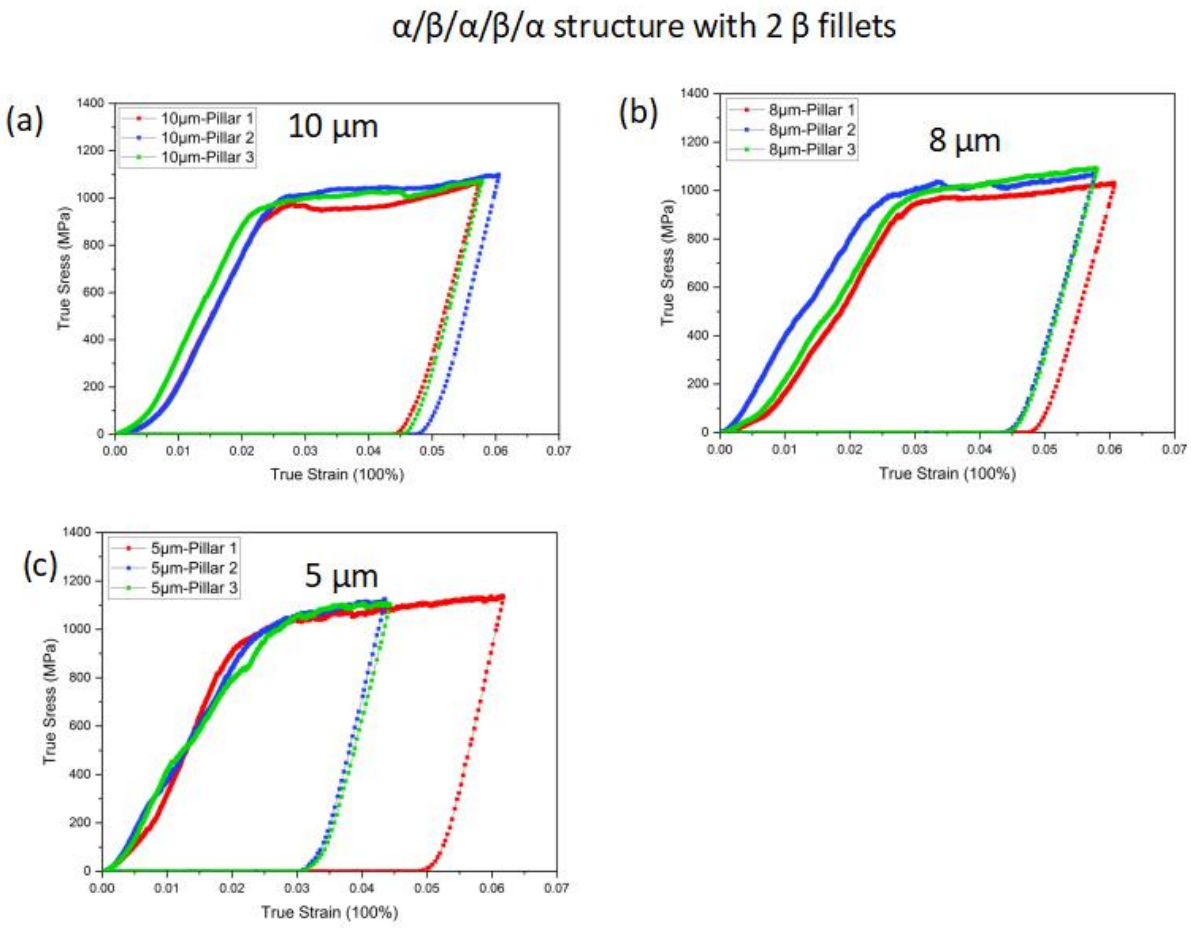

Fig. 4.4.9 Stress- strain curves after micro-compression of α/β/α/β/α micro-structures with 2 β phase fillets for prismatic <a_3> slip: (a) 10 µm in diameter; (b) 8 µm in diameter; (c) 5 µm in diameter.

Table 4.4.1. Summary of 0.2 proof stress ($R_{p0.2}$) and the critical resolved shear stress (τ_{CRSS}) for prismatic <a_3> slip with different quantities of β fillets. Mmax refers to the maxima of Schmid factor.

		0 β	**1 β**	**2 β**
Primary slip		<a_3> Prism	<a_3> Prism	<a_3> Prism
M_{max}		0.460	0.460	0.460
$R_{p0.2}$ (MPa)	10 µm	-	840 (±24)	941 (±21)
	8 µm	923 (±14)	895 (±61)	967 (±14)
	5 µm	837 (±58)	960 (±14)	992 (±33)
τ_{CRSS} (MPa)	10 µm	-	387 (±11)	433 (±9)
	8 µm	424 (±7)	412 (±28)	445 (±6)
	5 µm	385 (±27)	442 (±34)	456 (±15)

4.4.2 Slip System Analysis Using the TEM

In this section, TEM is utilised to analyse the slip band distribution, slip systems after deformation, the morphology of slip steps and β phase, as well as the interaction between dislocations and α/β interfaces for the deformed micro-pillars containing 0, 1 and 2 β fillets inside for the prismatic <a_3> slip. Three TEM foils are extracted from 8μm-sized micro-pillars to a strain of about 6%.

The micro-compression was performed up to the final strain of about 6% in order to have suitable dislocation density in the sample for the subsequent TEM observations.

Fig. 4.4.10 shows an overview of the cross-section of micro-pillars with different numbers of β fillets and the distribution of slip bands. Fig. 4.4.10 (a) represents a micro-pillar in a single α phase containing 0 β fillet and a limited distribution of slip bands, which concentrate at the top of the pillar; Fig. 4.4.10 (b) and (c) show more slip bands occurring with a more homogeneous distribution all cross the pillar from the top to the bottom. Meanwhile the differences in the number of slip bands and distribution are not significant between Fig. 4.4.10 (b) and (c).

For a micro-pillar containing 0 β fillet in a single α phase, two types of dislocations can be observed in Fig. 4.4.11 and Fig. 4.4.12. As is shown in Fig. 4.4.11, a two-beam condition is achieved to enhance or reduce the reflection of dislocations. BD~ [0001] and g vector of $\bar{1}\bar{1}20$ are selected in Fig. 4.4.11 (a), where dislocations are edge-on and visible, outlined by a dashed orange circle. However, when selecting g vectors of $1\bar{1}00$ and $1\bar{1}0\bar{1}$ respectively corresponding to BD~ [0001] and BD~ [$2\bar{1}\bar{1}3$], dislocations outlined by orange circles become invisible in Fig. 4.4.11 (b) and (c), indicating that this set of dislocations are <a_3> 1/3a[$\bar{1}\bar{1}20$]. Additionally, since <a_3> dislocations are edge-on under a two-beam condition with g = $\bar{1}\bar{1}20$, and BD~ [0001], the slip plane is ($1\bar{1}00$). So, the main slip system of

deformed micro-pillars in a single α phase is prismatic <a_3> 1/3a$[\bar{1}\bar{1}20]$ $(1\bar{1}00)$, dominating the plastic deformation. Different from the morphology of the SEM images in Fig. 4.4.11, the second set of slips are investigated in Fig. 4.4.12. Under a two-beam condition with g = $\bar{1}2\bar{1}0$ and BD~ [0001], dislocations outlined by dashed orange circles in Fig. 4.4.12 (a) are visible. When selecting g vectors of $10\bar{1}0$ and $10\bar{1}\bar{1}$ respectively corresponding to BD~ [0001] and BD~ $[2\bar{1}\bar{1}3]$, dislocations outlined by orange circles become invisible in Fig. 4.4.12 (b) and (c), indicating that this set of dislocations are <a_2> 1/3a$[\bar{1}2\bar{1}0]$. Likely, <a_2> dislocations are edge-on under a two-beam condition with g = $\bar{1}2\bar{1}0$ and BD~ [0001], and the slip plane is $(10\bar{1}0)$. Thus, the second activated slip system is prismatic <a_2> 1/3a$[\bar{1}2\bar{1}0]$ $(10\bar{1}0)$.

As micro-pillars containing 0, 1 and 2 β fillets are in the same grain (G1) oriented from [18 $\bar{8}$ $\overline{10}$ 1], their possible slip systems are the same, which are prismatic <a_2> and <a_3> for Schmid factors 0.397 and 0.460 respectively. Even the pyramidal <c+a> slip $(2\bar{1}\bar{1}2)[\bar{2}113]$ and pyramidal <a> slip $(\bar{1}101)$ $[11\bar{2}0]$ have a higher Schmid factor of 0.468 and 0.417, respectively, which are difficult to be activated due to their higher CRSS. The TEM results agree with it that both prismatic <a_2> 1/3a$[\bar{1}2\bar{1}0]$ $(1\,0\bar{1}0)$ and prismatic <a_3> 1/3a$[\bar{1}\bar{1}20]$ $(1\,\bar{1}0\,0)$ slip exist, as is shown in Fig. 4.4.13 to Fig. 4.4.16, where prismatic <a_3> slip dominates the plastic deformation. It should be noted that prismatic <a_2> slip in micro-pillars with 1 β fillet is more obvious than that in micro-pillars with 0 or 2 β fillets. The invisibility and visibility criteria for prismatic <a_2> and <a_3> slip with different g vectors are summarized in Table 4.4.2.

In Fig. 4.4.17, the morphology of slip steps is shown as blue dashed rectangles. The loading and slip directions are indicated by green and orange arrows. Large and sharp slip steps are obvious in deformed micro-pillars in a single α phase containing 0 β fillet, as is shown in Fig. 4.4.17 (a). Smaller slips are observed in deformed micro-pillars containing 1 β fillet in Fig.

4.4.17 (b), compared to micro-pillars with 0 β fillet. When the number of β fillets increases to 2 in Fig. 4.4.17 (c), no obvious slip steps can be investigated along the edge of the TEM foil.

The morphology of β phase after deformation is shown as blue dashed rectangles in Fig. 4.4.18. The loading and slip directions are indicated by green and orange arrows. When there is only 1 β fillet, β phase can be largely and even totally sheared or cut off. Comparably, when there are 2 β fillets in micro-pillars, β phase is less sheared.

The interaction between dislocations and α/β interfaces is investigated in Fig. 4.4.19. The interfaces are regarded as barriers that impedes the propagation of $<a_3>$ dislocations highlighted in blue dashed rectangles and $<a_2>$ dislocations generated from the interfaces in Fig. 4.4.19 (a). Once $<a_3>$ dislocations go through the interfaces and β phase under a high stress, the shear bands become wider, as is indicated by blue dash lines in Fig. 4.4.19 (b), where the shear bands before dislocation transmission are relatively narrow.

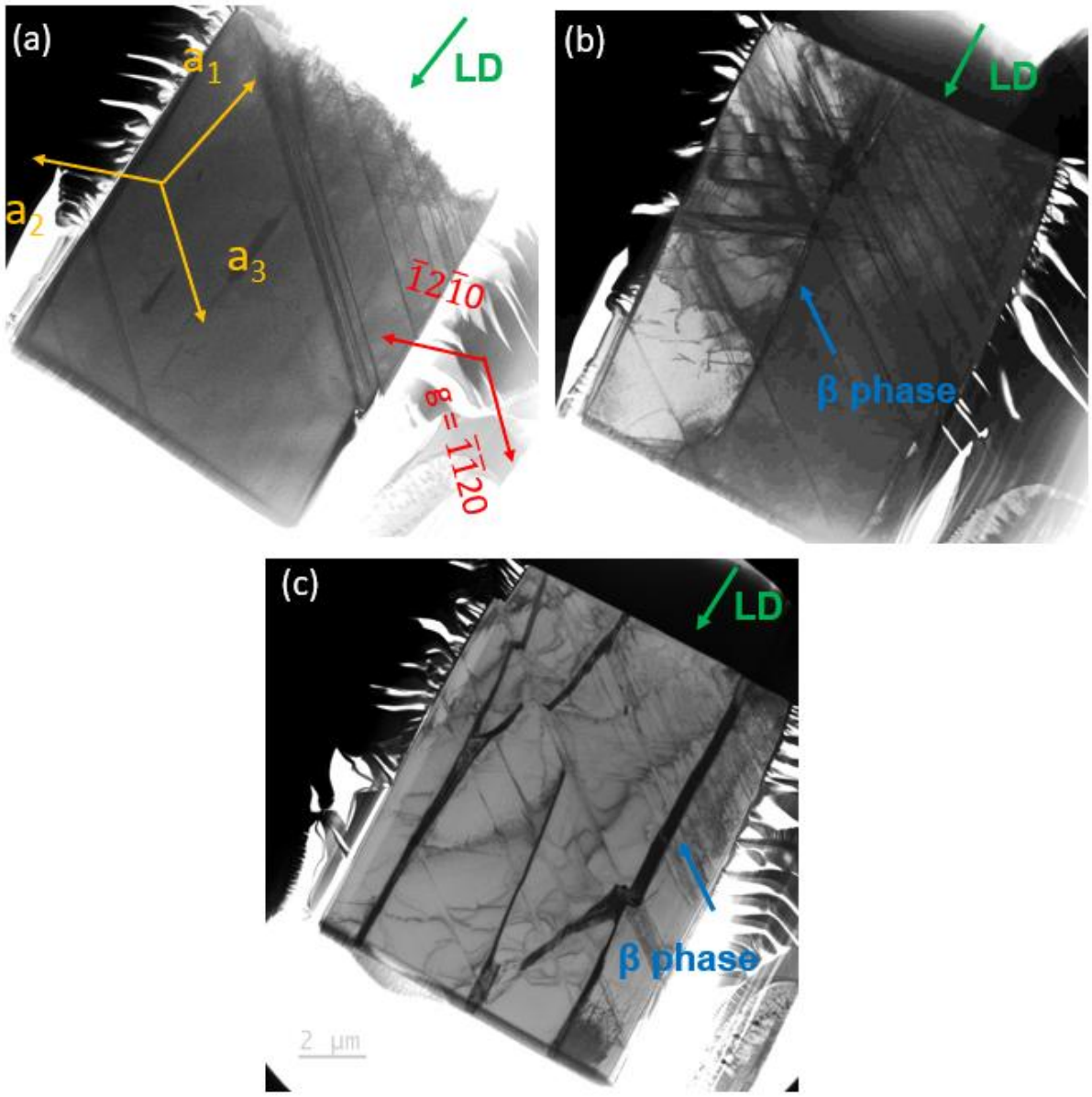

Fig. 4.4.10 An overview of TEM images from deformed micro-pillars with about 6% of strain for prismatic <a_3> slip in a two beam condition with g = $\bar{1}\bar{1}20$ and BD~[0001]. β phase and loading direction are indicated by blue and green arrows, respectively. Directions of <a_1>, <a_2> and <a_3> are shown as orange arrows. (a) Micro-pillar with 0 β fillet in a single α phase, (b) α/β/α-structured micro-pillars with 1 β fillet, (c) α/β/α/β/α structured micro-pillars with 2 β fillets.

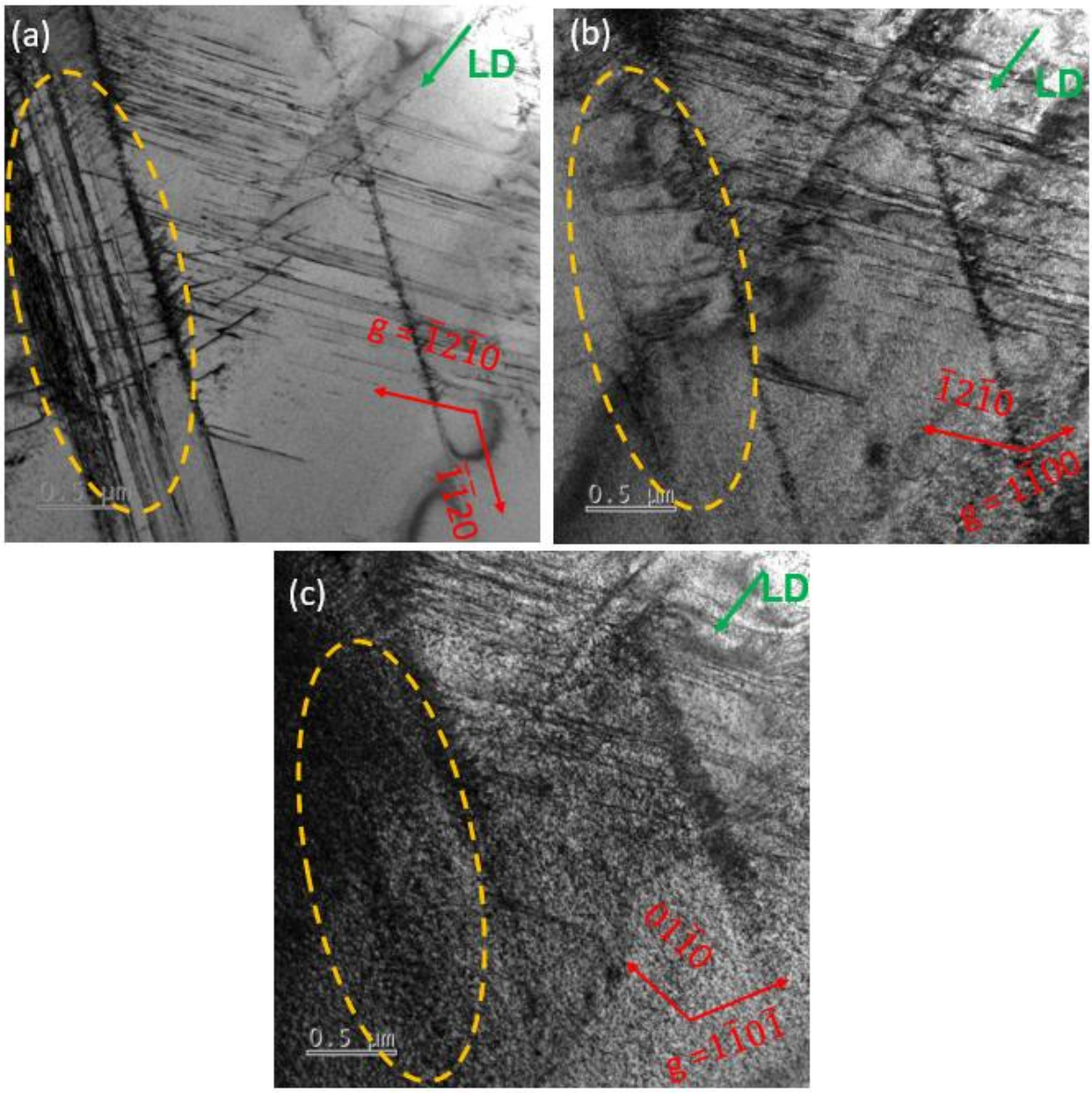

Fig. 4.4.11 Analysis of prismatic <a_3> slip from TEM bright field images of micro-pillars (0 β fillet) with a diameter of 8 μm under two-beam conditions in a single α after a strain of about 6%. Prismatic <a_3> slip is highlighted by orange dash circles, and the loading directions are indicated by green arrows. (a) g = $\bar{1}2\bar{1}0$, and BD~ *[0001]*, which are visible; *(b) g =* $1\bar{1}00$, and BD~ *[0001]*, which are invisible; *(c) g =* $1\bar{1}0\bar{1}$, and BD~ *[*$2\bar{1}\bar{1}3$*]*, which are invisible.

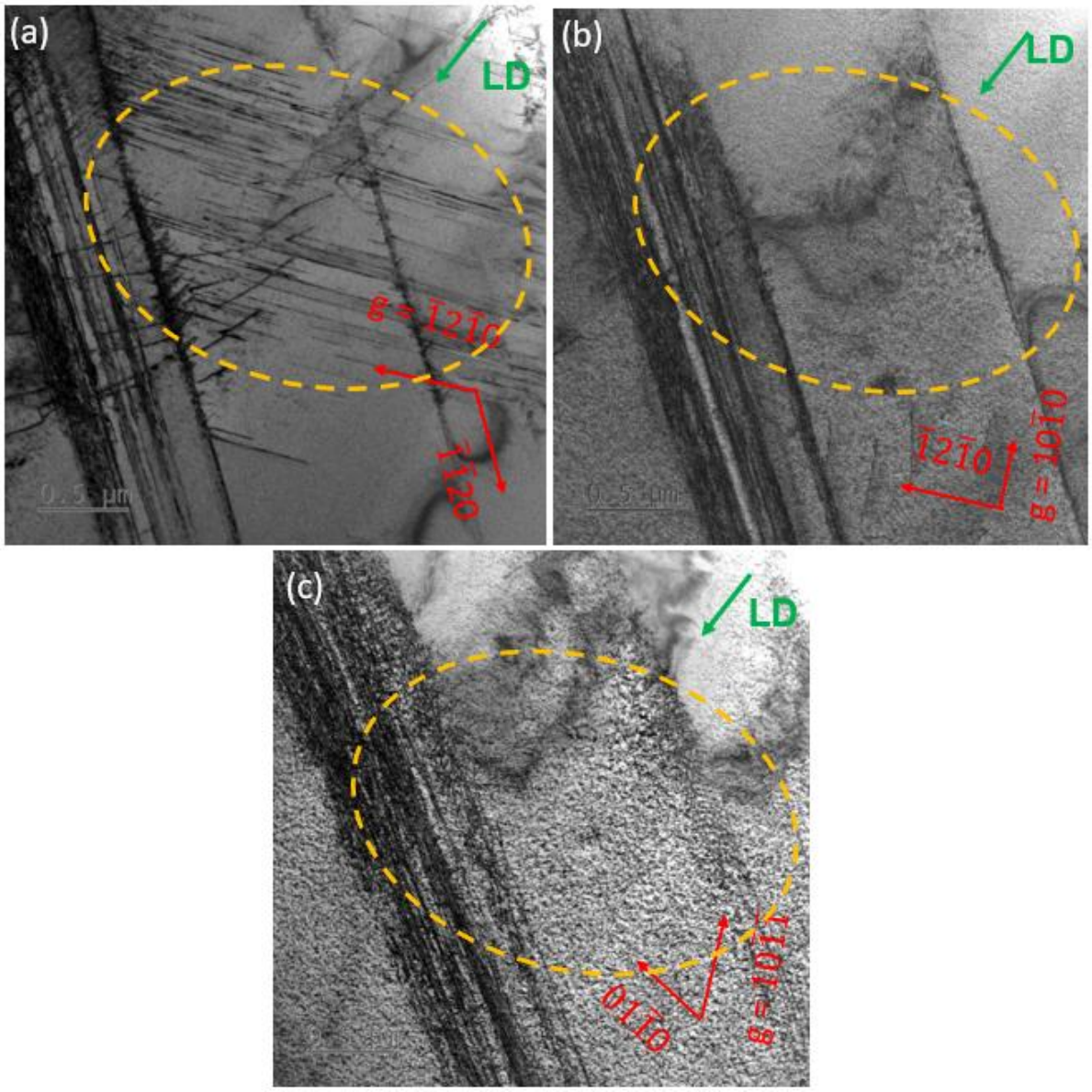

Fig. 4.4.12 Analysis of prismatic <a_2> slip from TEM bright field images of micro-pillars (0 β fillet) with a diameter of 8 μm under two-beam conditions in a single α after a strain of about 6%. Prismatic <a_2> slip is highlighted by orange dash circles, and the loading directions are indicated by green arrows. (a) g = $\bar{1}2\bar{1}0$, and BD~ *[0001]*, which are visible; *(b) g =* $10\bar{1}0$, and BD~ *[0001]*, which are invisible; *(c) g =* $10\bar{1}\bar{1}$, and BD~ *[*$2\bar{1}\bar{1}3$*]*, which are invisible.

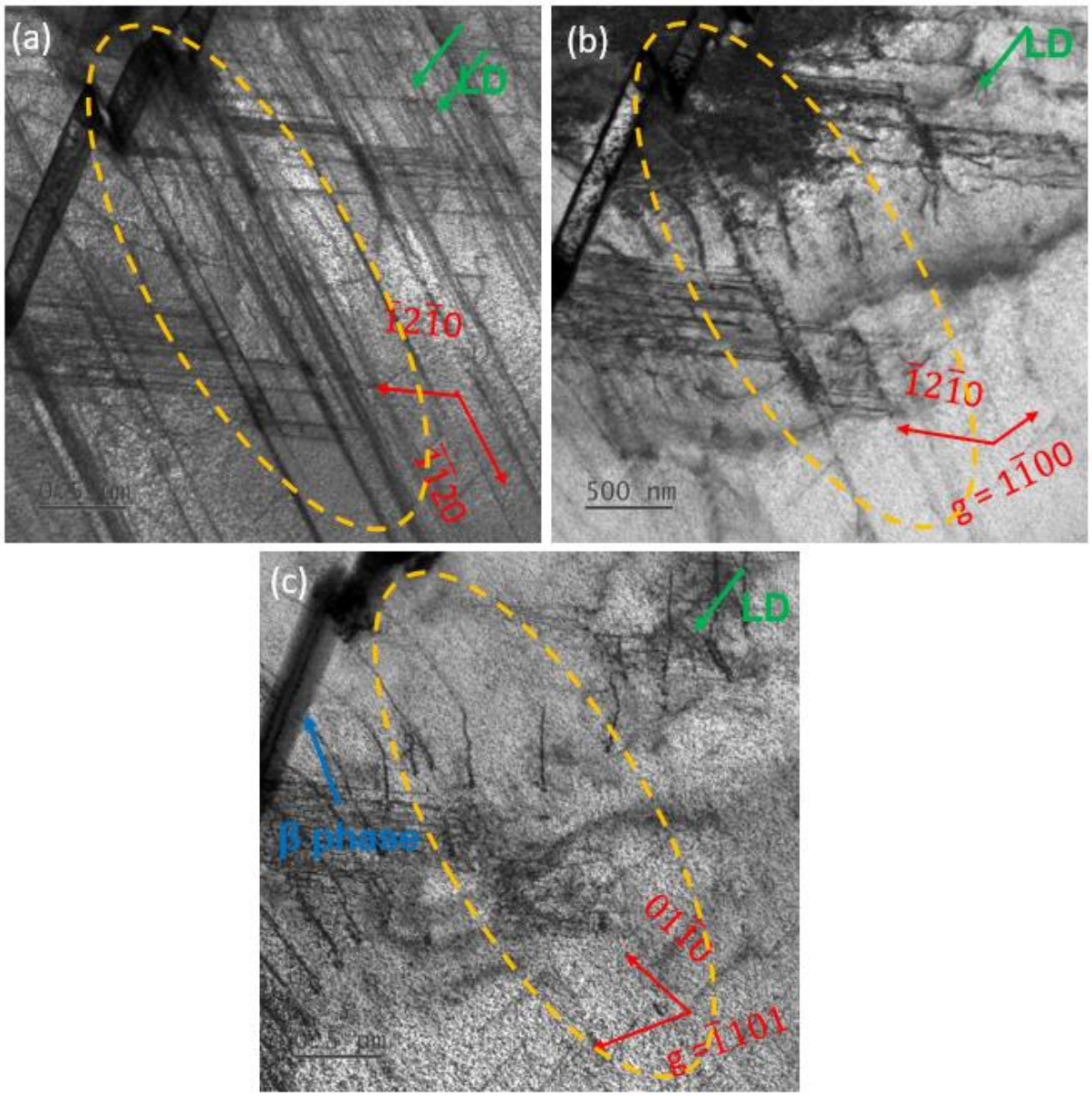

Fig. 4.4.13 Analysis of prismatic <a_3> slip from TEM bright field images of α/β/α structured micro-pillars (1 β fillet) with a diameter of 8 μm under two-beam conditions after a strain of about 6%. Prismatic <a_3> slip is highlighted by the orange dash circles, and the loading directions are indicated by green arrows. (a) $g = \bar{1}2\bar{1}0$, and BD~ *[0001]*, which are visible; *(b) $g = 1\bar{1}00$,* and BD~ *[0001]*, which are invisible; *(c) $g = \bar{1}101$,* and BD~ *[$2\bar{1}\bar{1}3$]*, which are invisible.

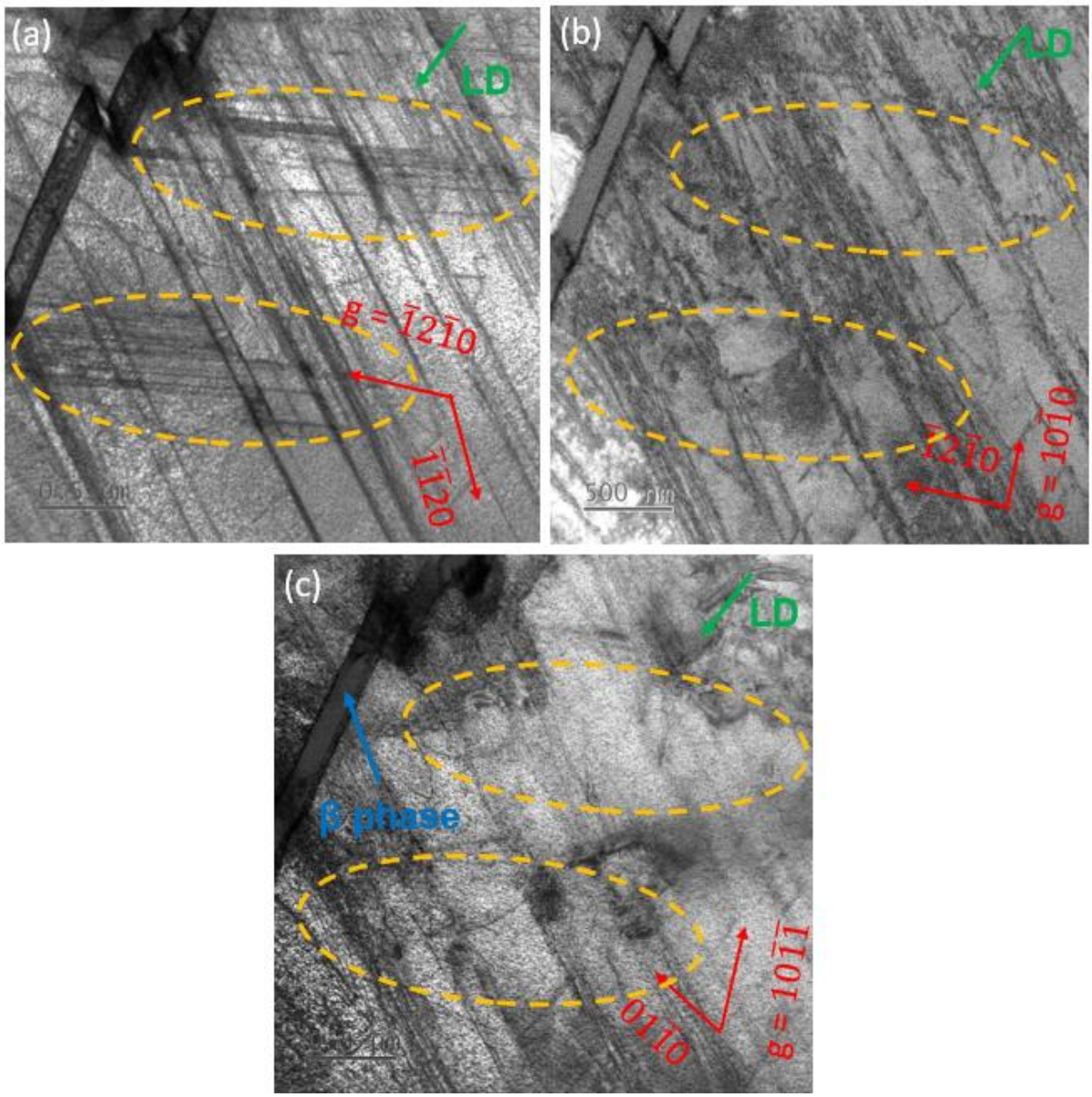

Fig. 4.4.14 Analysis of prismatic <a_2> slip from TEM bright field images of α/β/α structured micro-pillars (1 β fillet) with a diameter of 8 μm under two-beam conditions after a strain of about 6%. Prismatic <a_2> slip is highlighted by orange dash circles, and loading directions are indicated by green arrows. (a) g = $\bar{1}2\bar{1}0$, and BD~ *[0001]*, which are visible; *(b) g =* $10\bar{1}0$, and BD~ *[0001]*, which are invisible; *(c) g =* $10\bar{1}\bar{1}$, and BD~ *[*$2\bar{1}\bar{1}3$*]*, which are invisible.

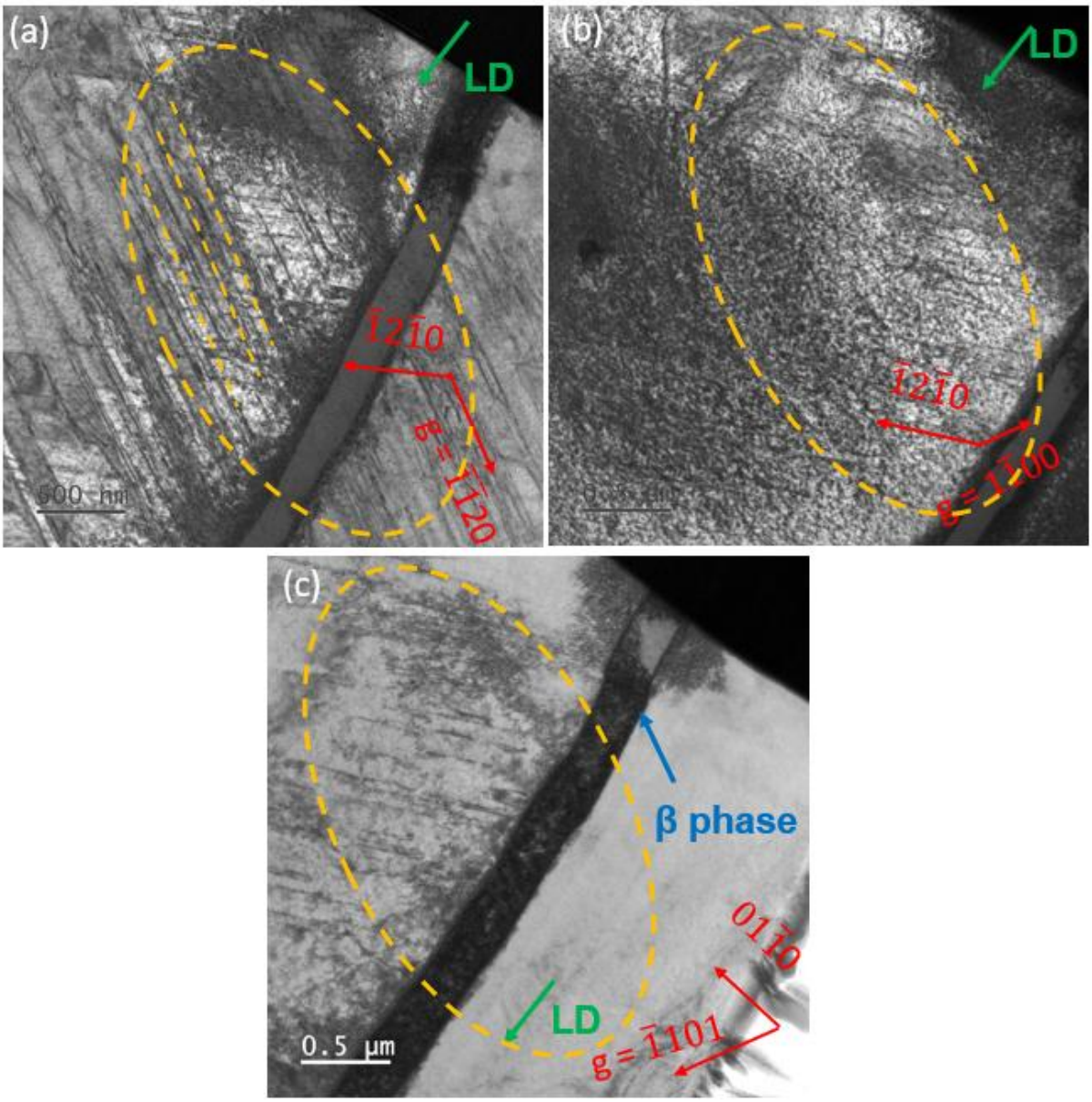

Fig. 4.4.15 Analysis of prismatic <a_3> slip from TEM bright field images of α/β/α/β/α structured micro-pillars (2 β fillets) with a diameter of 8 μm under two-beam conditions after a strain of about 6%. Prismatic <a_3> slip is highlighted by orange dash circles, and the loading directions are indicated by green arrows. (a) $g = \bar{1}\bar{1}20$, and BD~ *[0001]*, which are visible; *(b) $g = 1\bar{1}00$*, and BD~ *[0001]*, which are invisible; *(c) $g = \bar{1}101$*, and BD~ *[$2\bar{1}\bar{1}3$]*, which are invisible.

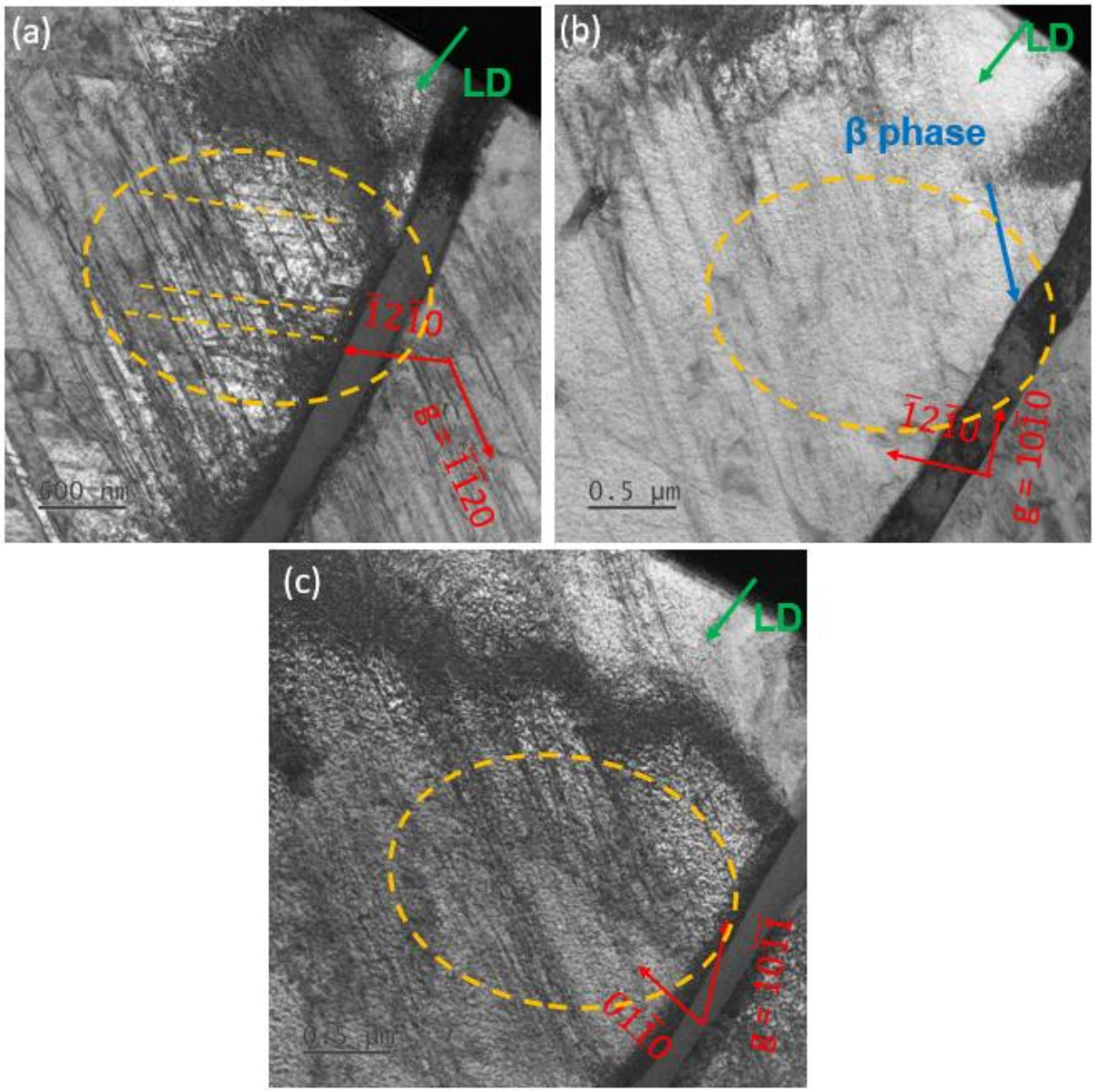

Fig 4.4.16 Analysis of prismatic <a_2> slip from TEM bright field images of α/β/α/β/α structured micro-pillars (2 β fillets) with a diameter of 8 μm under two-beam conditions after a strain of about 6%. Prismatic <a_2> slip is highlighted by orange dash circles, and the loading directions are indicated by green arrows. (a) $g = \bar{1}\bar{1}20$, and BD~ *[0001]*, which are visible; *(b) $g = 10\bar{1}0$*, and BD~ *[0001]*, which are invisible; *(c) $g = 10\bar{1}\bar{1}$*, and BD~ *$[2\bar{1}\bar{1}3]$*, which are invisible.

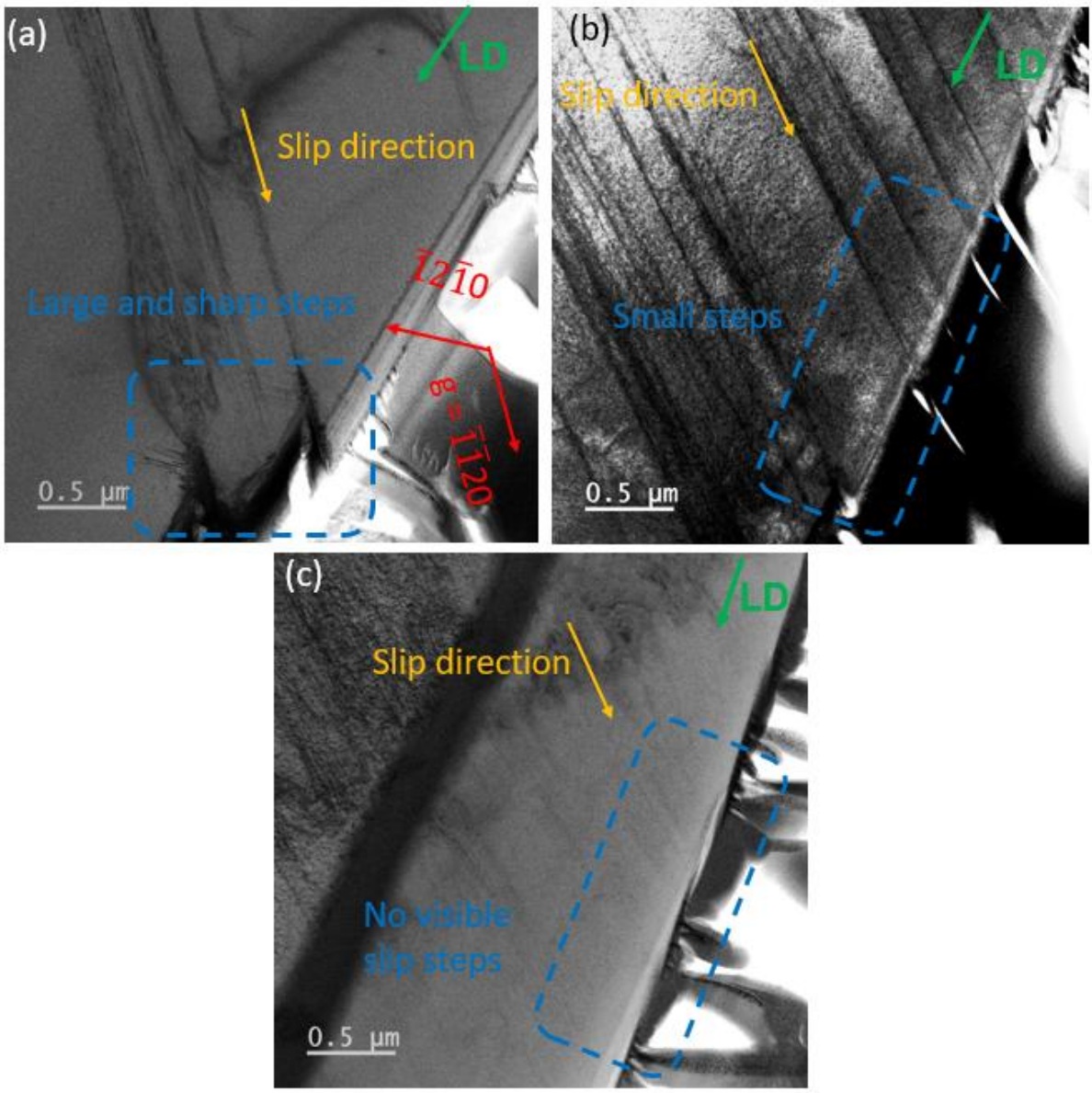

Fig. 4.4.17 A comparison of the size of slip steps through TEM images from deformed micro-pillars with about 6% of strain for prismatic <a_3> slip in a two-beam condition with g = $\bar{1}\bar{1}20$ *and* BD~ [0001]. *Loading directions are indicated by green arrows. Slip directions are shown as orange arrows. (a) Micro-pillars with 0 β fillet in a single α phase have the largest and sharpest steps (b) α/β/α-structured micro-pillars with 1 β fillet involve fewer steps (c) α/β/α/β/α-structured micro-pillars with 2 β fillets involve invisible steps*

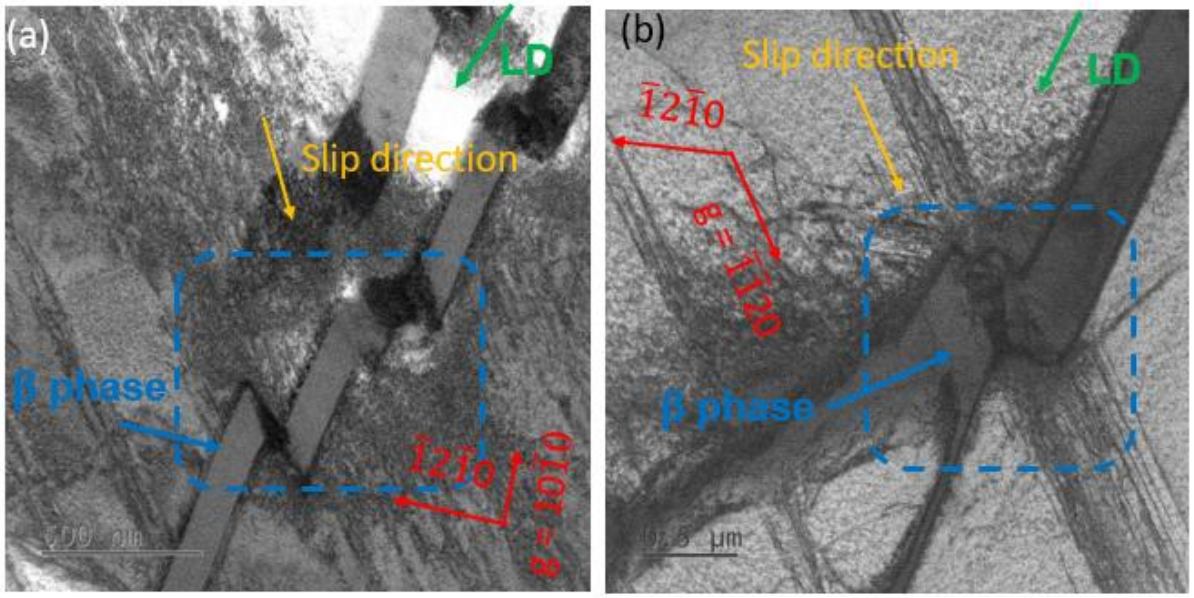

Fig. 4.4.18 The morphology of deformed micro-pillars in β phase through TEM images with about 6% of strain for prismatic <a_3> slip in a two-beam condition with g = $10\bar{1}0$, *BD~* [0001] *and g =* $\bar{1}\bar{1}20$, *BD~* [0001]. *Loading and slip directions are indicated by green and orange arrows. (a) For micro-pillars in a single α phase with 0 β fillet, β phase can be totally cut off, (b) For α/β/α-structured micro-pillars with 1 β fillet, β phase is largely deformed but not cut off, as is shown by blue dashed rectangles*

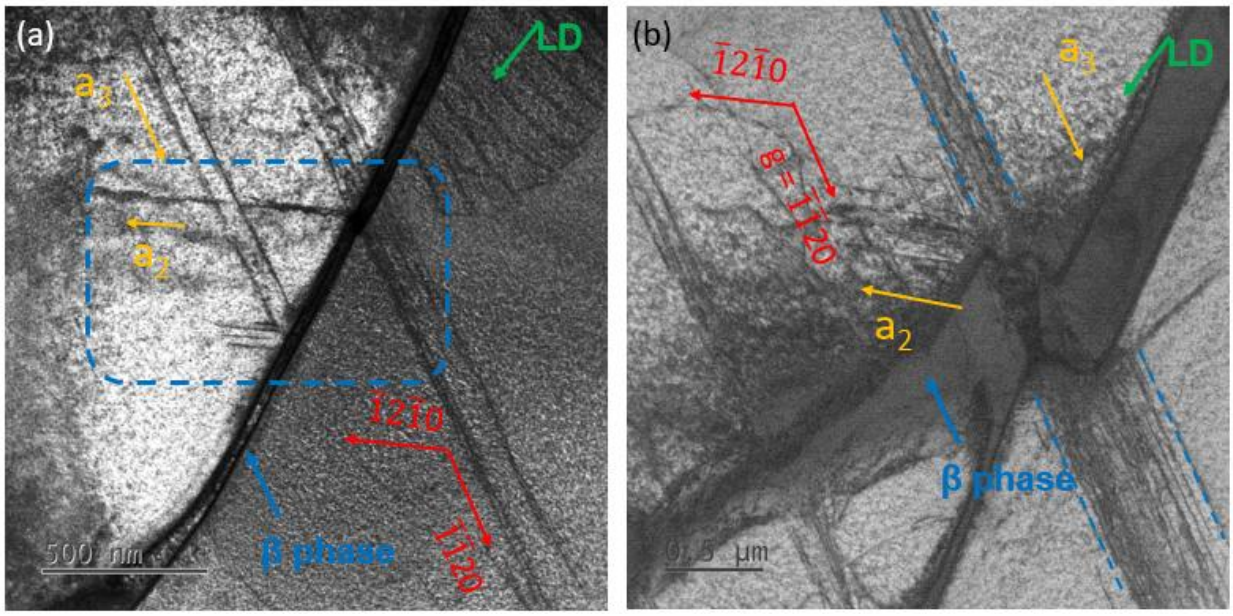

Fig. 4.4.19 TEM images of interactions between dislocations and α/β interfaces from deformed micro-pillars with about 6% of strain for *prismatic <a3> slip in a* two-beam condition *with g =* $\bar{1}\bar{1}20$ and BD~ *[0001]. Loading and slip directions are indicated by green and orange arrows. (a) The α/β interfaces stop the propagation of <a_3> and <a_2> dislocations generated at interfaces, (b) When dislocations go through interfaces and β phase, the width of shear bands becomes larger, as is shown by blue dashed lines*

Table 4.4.2. Summary of diffraction condition for prismatic <a_2> and <a_3> slip with different quantities of β fillets.

Beam direction	g	Prismatic <a_2> slip system a/3$[\bar{1}2\bar{1}0]$ $(10\bar{1}0)$	Prismatic <a_3> slip system a/3$[\bar{1}\bar{1}20]$ $(1\bar{1}00)$
[0001]	$\bar{1}2\bar{1}0$	Visible (edge on)	Visible (edge on)
[0001]	$\bar{1}\bar{1}20$	Visible (edge on)	Visible (edge on)
[0001]	$1\bar{1}00$	Visible (edge on)	Invisible
[0001]	$10\bar{1}0$	Invisible	Visible (edge on)
$[2\bar{1}\bar{1}3]$	$1\bar{1}0\bar{1}$	Visible	Invisible
$[2\bar{1}\bar{1}3]$	$10\bar{1}\bar{1}$	Invisible	Visible

4.4.3 Summary

The deformation of compressed micro-pillars containing 0, 1 and 2 β fillets with different sizes, namely 10μm, 8μm and 5μm in diameter, is studied. True stress-strain curves are of a strain of 4%-6%, meanwhile the deformation behaviour of micro-pillars is released based on SEM and TEM characterizations.

The mean yield stress (0.2% proof stress) and CRSS are obtained from stress-strain curves. The strain hardening rate in stress-strain curves is extremely low.

For micro-pillars of the same size of 5 μm, the mean yield stress increases gradually by increasing the number of β fillets from 0 to 2. The mean yield stresses of micro-pillars of the same size but various numbers (0, 1 and 2) of β phase are 837 (±58) MPa, 960 (±14) MPa and 992 (±33) MPa, respectively corresponding to CRSS values of 385 (±27) MPa, 442 (±34) MPa and 456 (±15) MPa. The mean yield stress and CRSS increase by 18.5% when the number of β fillets changes from 0 to 2.

For the same number of β fillets, mean yield stress increases gradually by reducing the pillar size from 10μm to 5μm. The mean yield stresses of micro-pillars containing 1 β fillet but various sizes (10μm, 8μm and 5μm) are 840 (±24) MPa, 895 (±61) MPa and 960 (±14) MPa, respectively corresponding to CRSS values of 387 (±11) MPa, 412 (±28) MPa, and 442 (±34) MPa. The mean yield stress and CRSS increase by 14.2% when the pillar size reduces from 10μm to 5μm. Additionally, the mean yield stresses of micro-pillars containing 2 β fillets but various sizes (10μm, 8μm and 5μm) are 941 (±21) MPa, 967 (±14) MPa and 992 (±33) MPa, respectively corresponding to CRSS values of 433 (±9) MPa, 445 (±6) MPa and 456 (±15) MPa. The mean yield stress and CRSS increase by 5.3% when the pillar size reduces from 10μm to 5μm. However, there is an abnormal phenomenon observed for deformed micro-pillars without β fillets that the strength decreases when reducing the pillar size from 8μm to

5μm. As seen in the Fig. 4.4.1(e), the whole micro-compression process was not disturbed by the surrounding walls. So, this result doesn't agree with the external size effect. And the reason for it remains to be studied furthermore.

Based on an analysis of the slip systems through TEM results, prismatic $<a_2>$ and prismatic $<a_3>$ slips are activated and prismatic $<a_3>$ slip dominates the plastic deformation.

The number of shear bands increases with that of β fillets increasing from 0 to 2, which means that shear bands are easier to form when introducing more β fillets or interfaces.

Comparing the morphology of micro-pillars in β phase with 1 and 2 β fillets, those β phase in micro-pillars containing 1 β fillets or 2 interfaces can be cut off or largely sheared, where β phase in micro-pillars containing 2 β fillets are less deformed. It indicates that more β fillets or interfaces can impede the deformation of β phase.

When $<a_3>$ dislocations go towards the interfaces, they can be stopped and piled up at the interfaces. Even, $<a_2>$ dislocations can be generated at interfaces due to local stress concentration.

Dislocations are subjected to the image force when located close to a free surface. Such image force tends to drag screw dislocation out of the materials[114, 115] via cross slip hence the fact that screw dislocations are rarely observed in TEM samples. However, in the current work, the dislocations are expected to be present in the form of dislocation loops rather than pure screw formed during the compression. Furthermore, the TEM foils were prepared in parallel to the loading axis, rather than parallel to the slip planes. Therefore, it is believed that most of dislocations generated are preserved and that the image force has no significant effect on the TEM observation.

4.5 Micro-pillars containing 2 β Fillets Oriented for Prismatic <a_2> Slip

This part is to study the deformation behaviour of micro-pillars containing 2 β fillets for the prismatic <a_2> slip with a Schmid factor of 0.455. All pillars are fabricated from Grain 2 along the loading direction [$\bar{6}60\bar{1}$].

4.5.1 Surface Morphology of the Deformed Micro-pillars and the Corresponding Stress-strain Curves

Compression tests on micro-pillars containing 2 β fillets and different sizes (10μm, 5μm and 2μm in top diameter) are performed with strains ranging from 2.5% to 6% in a displacement-controlled system. Fig. 4.5.1 and Fig. 4.5.2 show the surface morphology of micro-pillars before and after compression. Fig. 4.5.3 shows the true stress-strain curves with different pillar sizes. The yield stresses and CRSS values obtained from 0.2% proof point are summarized in Table 4.5.1.

In Fig. 4.5.1, all slip bands are on prismatic planes, β phase is indicated by orange dash lines, meanwhile slip bands are difficult to be observed at the α/β/α/β/α-structured micro-pillars with a relative low magnification after compression. Only one set of slip bands can be investigated in Fig. 4.5.2 at a high magnification, which homogeneously distribute from the top to the bottom of the pillars, as is indicated by red arrows. There is no difference in surface morphologies with different sizes. The effect of size on the step size and the distribution of slip bands can be ignored.

Stress-strain curves obtained in Fig. 4.5.3 with different sizes (10μm, 8μm and 5μm in top diameter) have similar shapes with a very low strain hardening rate, and the yield stresses are between 800 MPa and 1000 MPa. Small load drops can be observed during the plastic deformation due to shear band nucleation and formation.

More accurate values of the average yield stress (0.2% proof point) and CRSS are obtained. The average yield stresses (0.2% proof point) are 888 (±18) MPa, 923 (±14) MPa and 970 (±35) MPa for 10μm, 5μm and 2μm-sized micro-pillars, respectively corresponding to CRSS values of 404 (±8) MPa, 420 (±6) MPa and 441 (±16) MPa. With the size decreasing, yield stress and CRSS increase. All yield stresses and CRSS values are listed in Table 4.5.1.

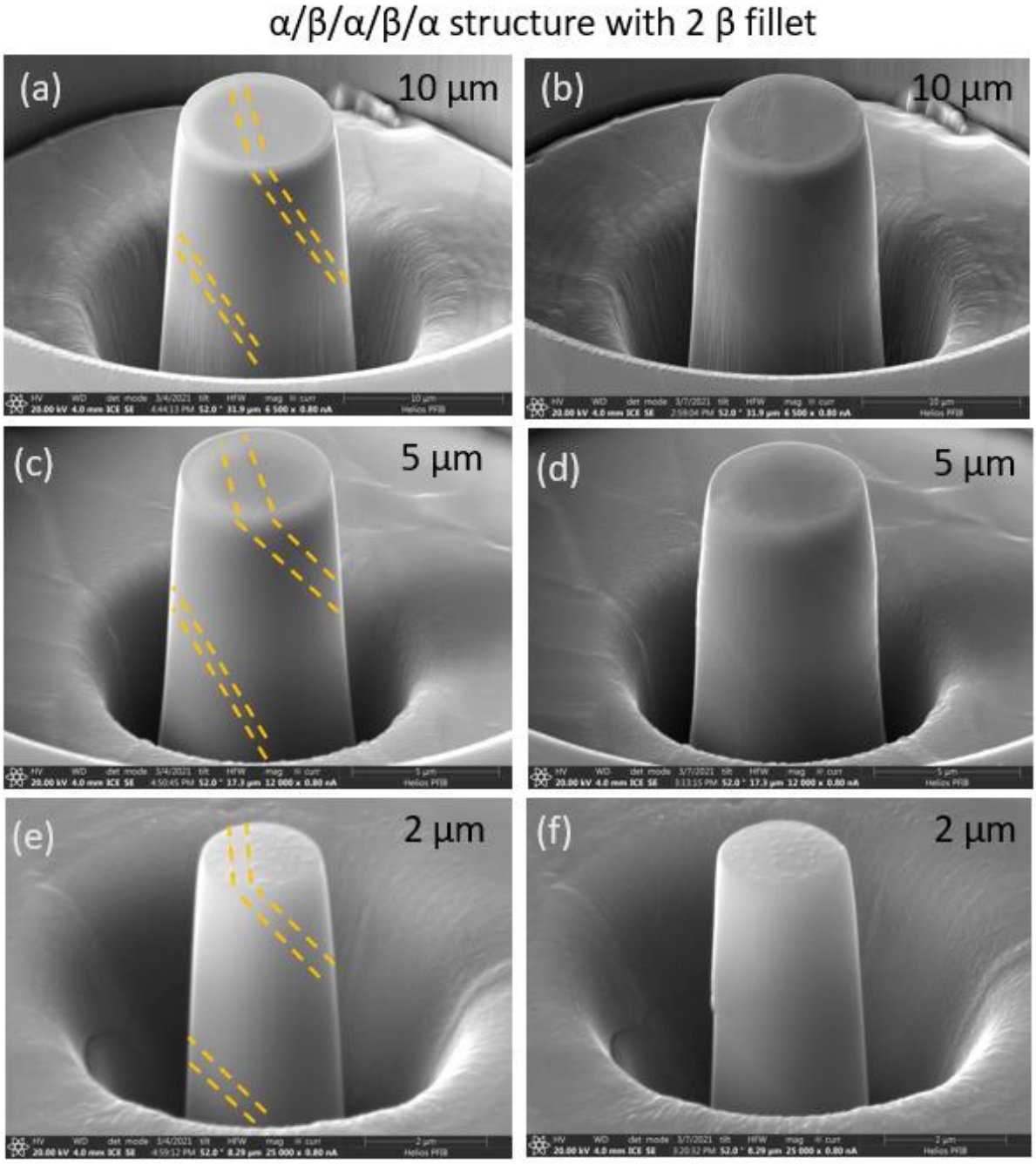

Fig. 4.5.1 SEM images of surface morphology before and after micro-compression from 10μm,5μm and 2μm pillars in a α/β/α/β/α micro-structure with 2 β phases along the direction of $[\bar{6}60\bar{1}]$ *for prismatic <a_2> slip (β phase is indicated by orange dash lines). (a), (c)and (e) are the micro-pillar images of 10μm, 5μm and 2μm pillars before compression, while (b), (d) and (f) are the images of 10μm, 5μm and 2μm pillars after compression with about 3% of strain. Very small slip steps are difficult to be investigated.*

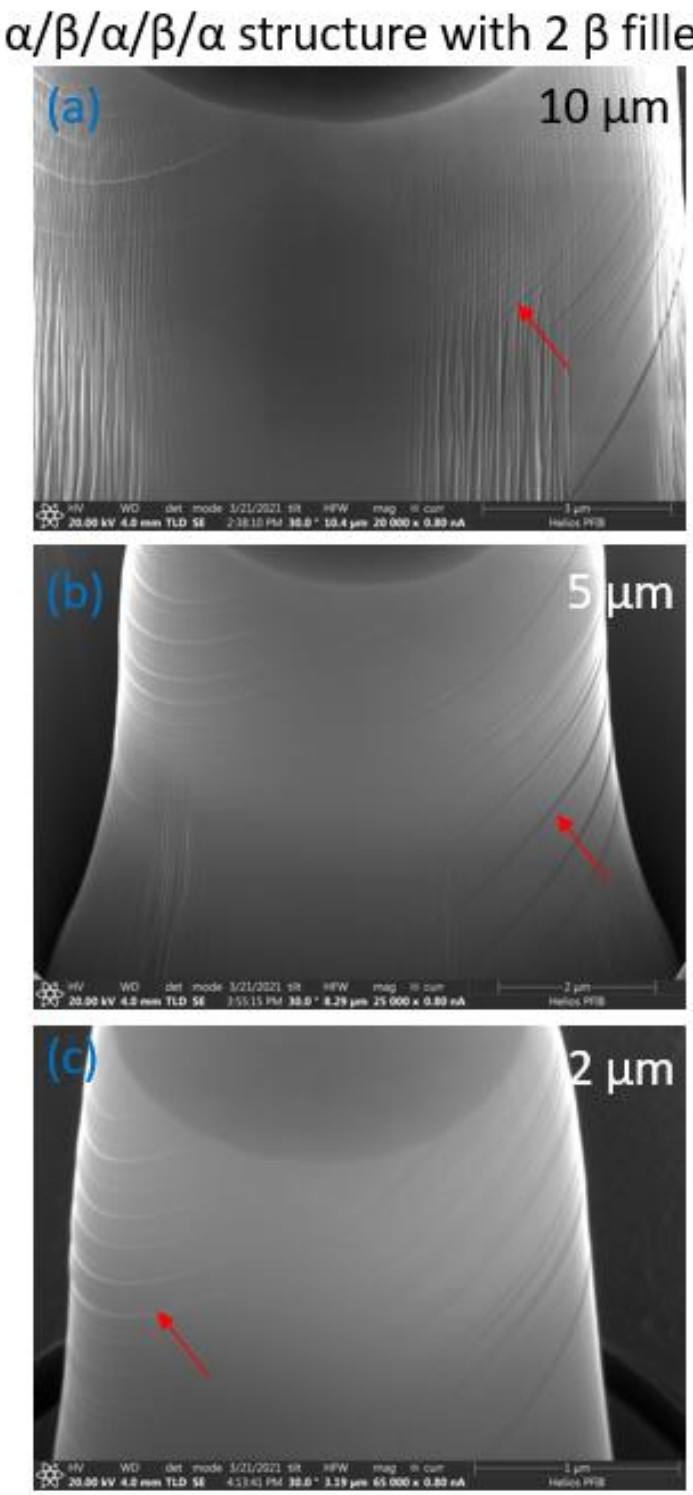

Figure 4.5.2 SEM images of surface morphology after micro-compression from 10µm, 5µm and 2µm pillars in a α/β/α/β/α micro-structure with 2 β phases along the direction of $[\bar{6}60\bar{1}]$ *for prismatic <a_2> slip. Small slip steps are indicated by red arrows.*

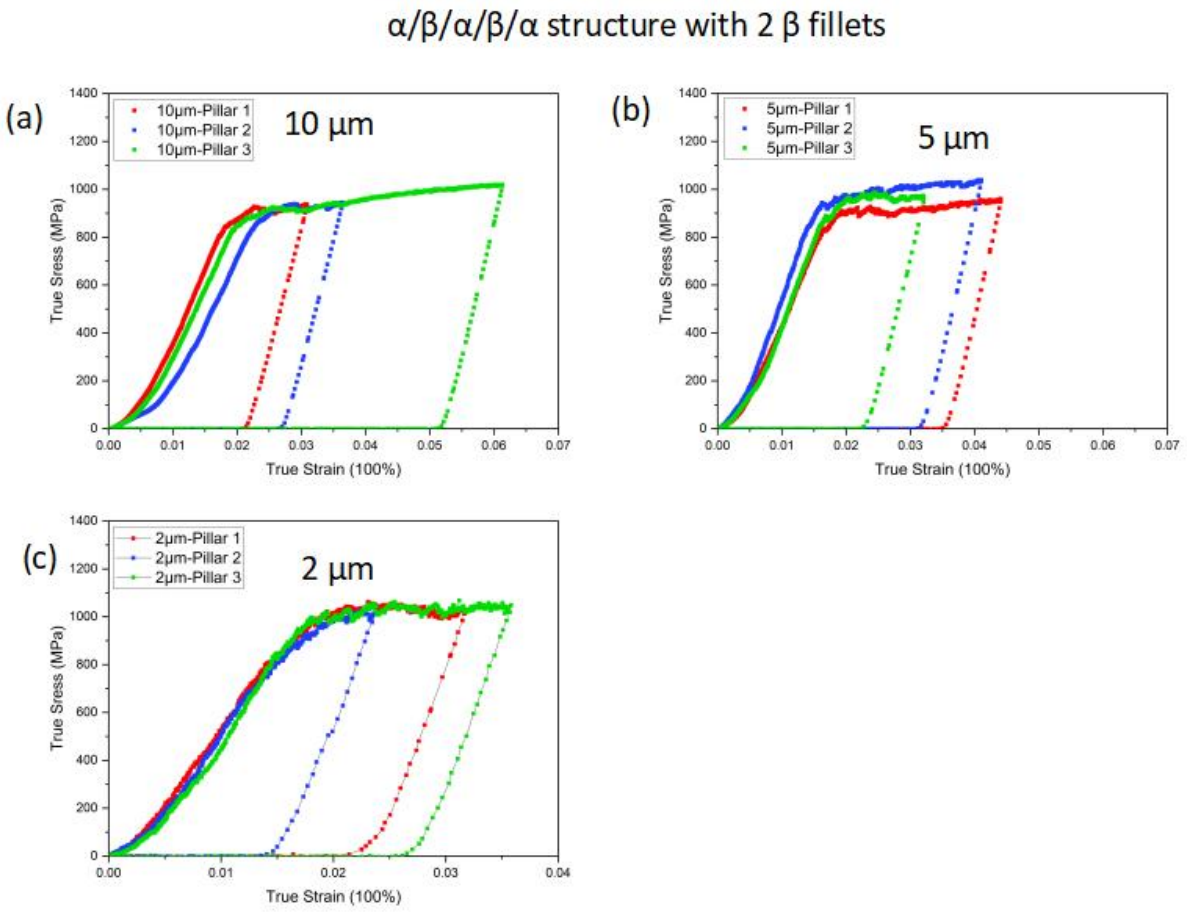

Fig. 4.5.3 Stress- strain curves after micro-compression of α/β/α/β/α micro-structures with 2 β phase fillets for prismatic <a_2> slip: (a) 10 µm in diameter; (b) 5 µm in diameter; (c) 2 µm in diameter.

Table 4.5.1. Summary of 0.2 proof stress ($R_{p0.2}$) and the critical resolved shear stress (τ_{CRSS}) for prismatic <a_2> slip with different sizes of micro-pillars.

No. of β	Primary slip	M_{max}	$R_{p0.2}$ (MPa)			τ_{CRSS} (MPa)		
			10 μm	5 μm	2 μm	10 μm	5 μm	2 μm
2 β	<a_2> Prism	0.455	888(±18)	923(±14)	970(±35)	404(±8)	420(±6)	441(±16)

4.5.2 Slip System Analysis Using the TEM

TEM is used to analyse slip band distribution, slip systems after deformation, the morphology of slip steps and β phase as well as interaction of dislocations with α/β interfaces for the deformed micro-pillars containing 2 β fillets after prismatic <a_2> slip. The TEM foil is extracted from 8μm-sized micro-pillars with a strain of about 3%.

An overview of the cross-section of micro-pillars containing 2 β fillets shows the distribution of shear bands in Fig. 4.5.4, together with the morphology of β phase and slip steps. The TEM images are taken in a multiple-beam condition along ~BD [0001]. Two β fillets are indicated by blue arrows. It can be observed that slip bands homogeneously distribute across all pillars. All dislocations are edge-on in α phase. No significant β phase shearing can be found, and slip steps are also very small and difficult to be seen. As is shown in the SEM images, the size of slip steps is estimated to be about 10nm.

In Fig. 4.5.5, visibility and invisibility criteria are achieved to determine the dislocation type. Dislocations and β phase are indicated by orange dashed lines and blue arrows. Only one type of dislocations can be found after compression. As is shown in Fig. .4.5.5 (a), a two-beam condition with BD~ [0001] and g vector of $01\bar{1}0$ is selected, while dislocations are visible. However, under the conditions with g = $10\bar{1}0$, BD~ [0001] and g = $10\bar{1}1$ BD~ [$\bar{2}113$], dislocations become invisible, which indicates that the type of dislocations is <a_2> a/3[$\bar{1}2\bar{1}0$]. Additionally, the slip plane can be determined as a prismatic plane ($10\bar{1}0$), as all dislocations are edge-on, which means that the slip plane is edge-on with normal direction of [$10\bar{1}0$]. So, the slip system can be determined as prismatic <a_2> a/3 [$\bar{1}2\bar{1}0$] ($1\,0\bar{1}0$). The visibility and invisibility criteria for different two-beam conditions are summarized in Table 4.5.2.

In Fig. 4.5.6, the interaction between dislocations and α/β interfaces can be investigated. The loading and slip direction are indicated by green and orange arrows. The interfaces are regardes as barriers to impede the propagation of <a_2> dislocations highlighted by orange dashed circles. When <a_2> dislocations go towards the interfaces, some dislocations are stopped by such barriers, while others can go through the interfaces and change their slip direction to <b_2> in β phase. Then <b_2> dislocations again go back into the α phase as the slip direction returns to <a_2>. The angle between <a_2> and <b_2> is 12 , which is very close to the 11 reported.

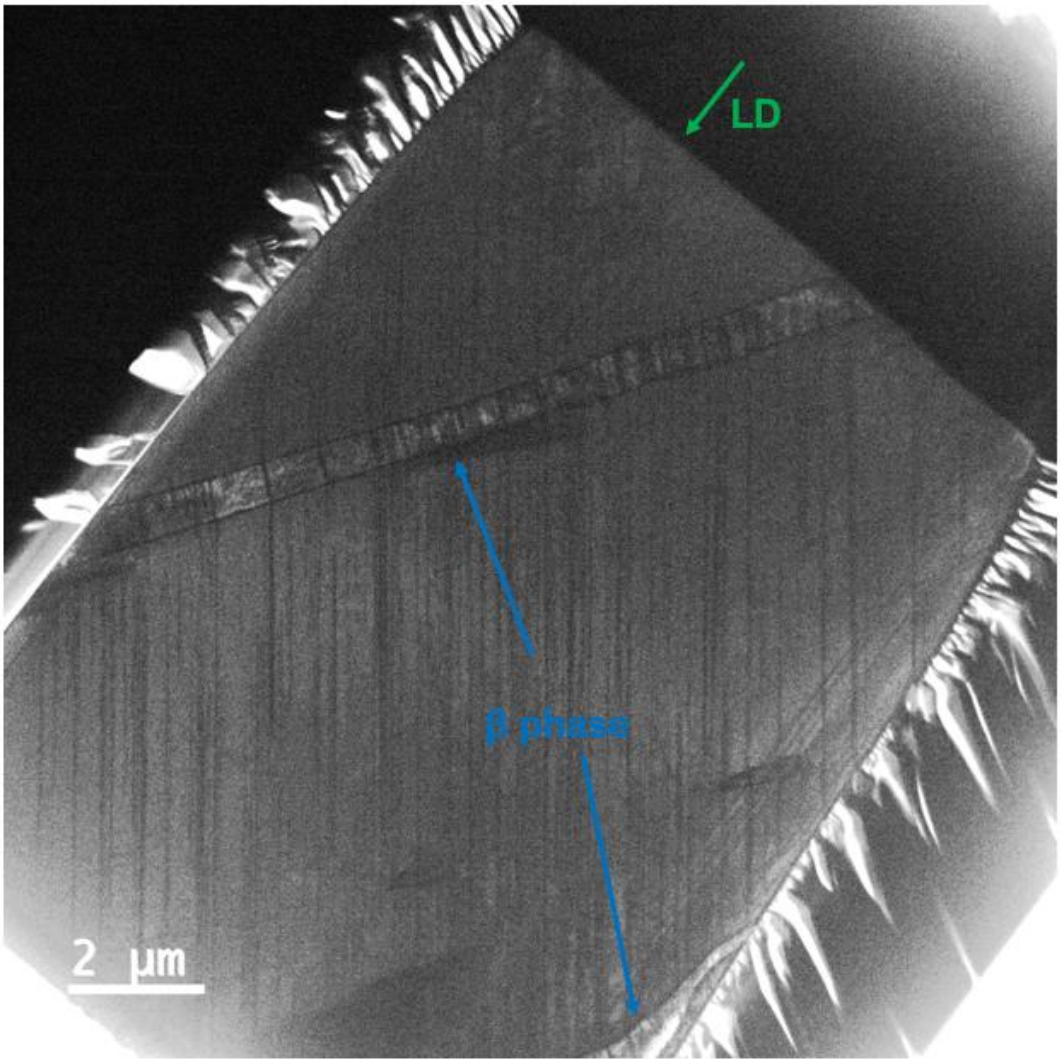

Fig. 4.5.4 An overview of TEM image from deformed micro-pillars with 2 β fillets to about 3% of strain for prismatic <a_2> slip in a multiple beam condition with BD~ [0001]. β phase and loading direction are indicated by blue and green arrows, respectively. Dislocations are edge-on and shear bands distribute homogeneously across the whole pillar. There is no big deformation of β phase and slip steps are very small.

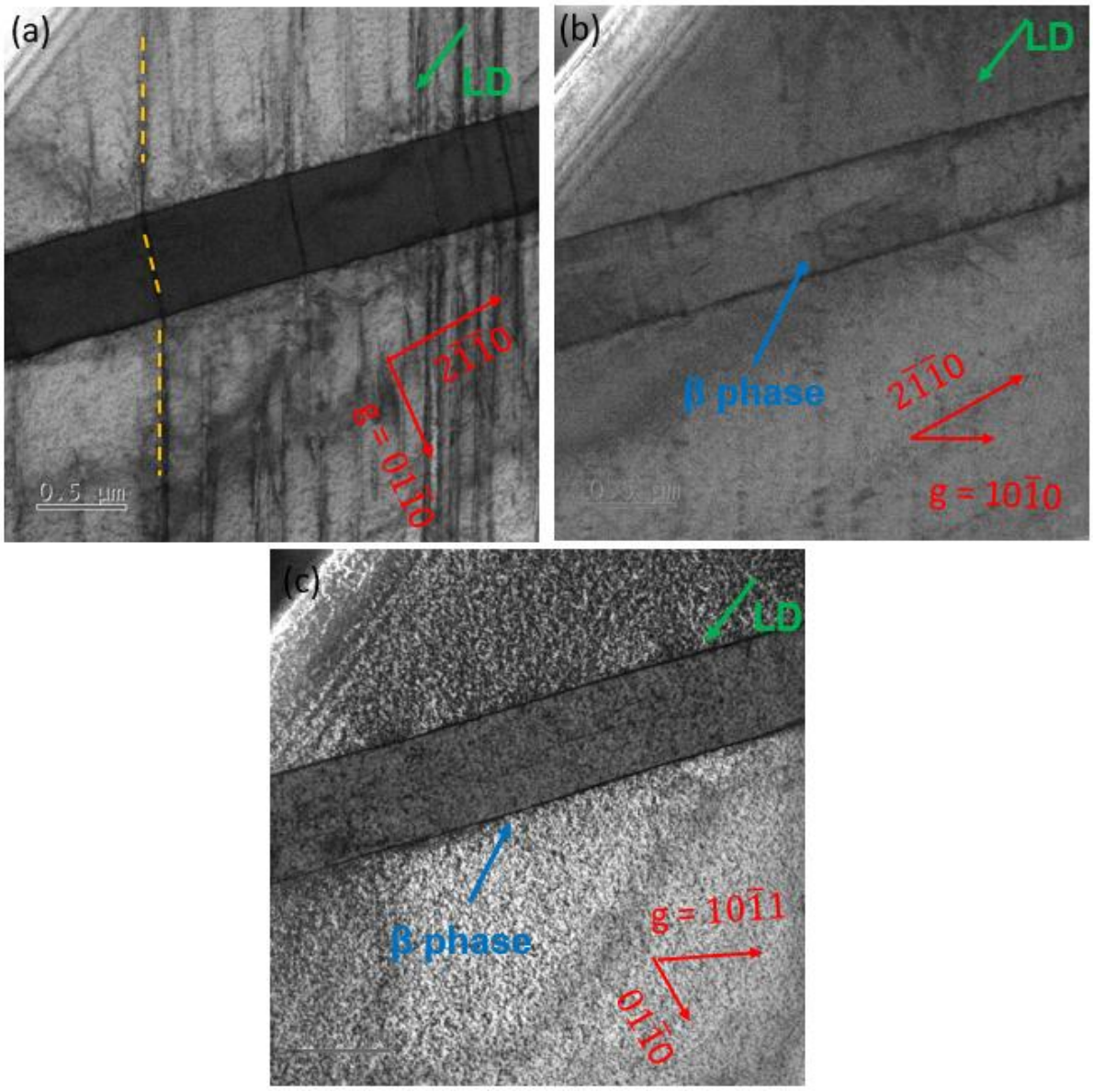

Fig. 4.5.5 Analysis of prismatic <a_2> slip from TEM bright field images of α/β/α/β/α structured micro-pillars (2 β fillets) with a diameter of 8 μm under two-beam conditions after deformed to a strain of about 6%. Prismatic <a_2> slip is highlighted by orange dash circles, and the loading directions are indicated by green arrows. (a) g = $01\bar{1}0$, and BD~ *[0001]*, which are visible; *(b) g =* $10\bar{1}0$, and BD~ *[0001]*, which are invisible; *(c) g =* $10\bar{1}1$, and BD~ *[*$\bar{2}113$*]*, which are invisible.

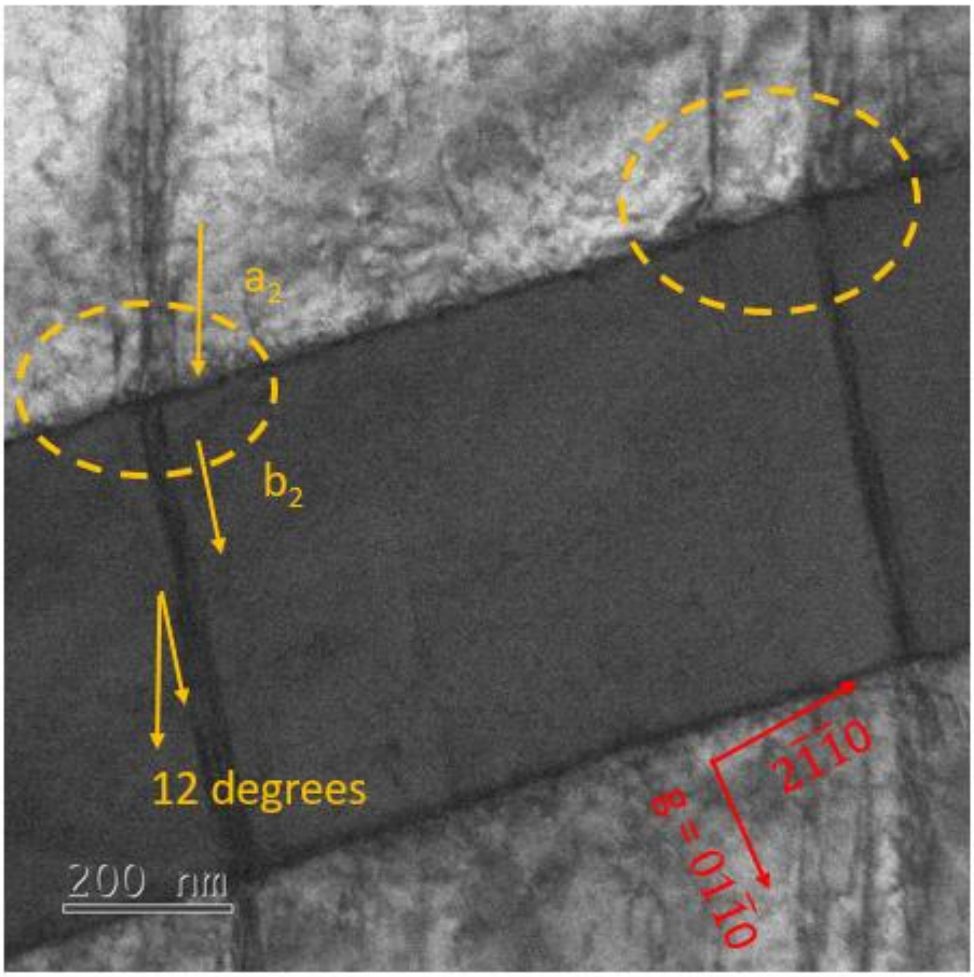

Fig. 4.5.6 TEM images of interactions between dislocations and α/β interfaces from deformed micro-pillars with about 3% of strain for prismatic <a_2> slip in a two-beam condition with g = 01$\bar{1}$0 and BD~ [0001]. Loading and slip directions are indicated by green and orange arrows. Some of the dislocations are impended by the interfaces, as is indicated by orange dashed circles.

Table 4.5.2. Summary of diffraction condition for prismatic <a_2> slip.

Beam direction	g	Prismatic <a_2> slip system a/3[$\bar{1}2\bar{1}0$] ($10\bar{1}0$)
[0001]	$01\bar{1}0$	Visible (edge on)
[0001]	$10\bar{1}0$	Invisible
[$\bar{2}113$]	$10\bar{1}\bar{1}$	Invisible

4.5.3 Summary

The deformation of compressed micro-pillars containing 2 β fillets with different sizes, namely 10µm, 5µm and 2µm in diameter, is studied for prismatic <a_2> slip. The deformation behaviour of micro-pillars is released through true stress-strain curves to a strain of 2.5%-6%, SEM and TEM characterizations.

The mean yield stress (0.2% proof stress) and CRSS are determined from stress-strain curves, with very low strain hardening rates. There are slight load drops during plastic deformation, which is related to shear band nucleation and formation.

For the same number of 2 β fillets in micro-pillars, mean yield stress increases gradually while reducing the pillar size from 10µm to 2µm. The mean yield stresses are 888 (±18) MPa, 923 (±14) MPa and 970 (±35) MPa, respectively corresponding to the CRSS values of 404 (±8) MPa, 420 (±6) MPa and 441 (±16) MPa. The mean yield stress and CRSS increase by 4% when the pillar size reduces from 10µm to 5µm, which, additionally, increase by 9.2% when the pillar size reduces from 10 µm to 2 µm.

Based on the slip system analysis using TEM, only prismatic $<a_2>$ slips are activated. A large number of shear bands homogeneously distribute across all pillars. There is no apparent deformation of β phase or slip steps.

When $<a_2>$ dislocations go towards the interfaces, they can be stopped and piled-up at those interfaces. Then slip direction changes to $<b_2>$ and again returns to $<a_2>$ as dislocations go back to α phase.

4.6 Micro-pillars containing ~10 β Fillets Oriented for Pyramidal $<a_3>$ Slip

This part is to study the deformation behaviour of micro-pillars with 10 β fillets for the pyramidal $<a_3>$ slip with a Schmid factor of 0.490. All pillars are fabricated from Grain 5 with a loading direction of $[02\bar{2}\bar{1}]$.

4.6.1 Surface Morphology of the Deformed Micro-pillars and the Corresponding Stress-strain Curves

Compression tests on micro-pillars with 10 β fillets and different sizes (10μm, 8μm and 5μm in top diameter) are performed with a strain of about 4% in a displacement-controlled system. Fig. 4.6.1 shows the surface morphology of micro-pillars before and after compression. Fig. 4.6.2 shows the true stress-strain curves with different pillar sizes. The yield stress and CRSS values obtained from 0.2% proof point are summarized in Table 4.6.1.

Representative SEM images in Fig. 4.6.1 shows the surface morphology of micro-pillars containing 10 β fillets before and after deformation. β phase is indicated by orange dash lines.

Only one set of slip bands and one significant slip band can be investigated at a high magnification, as is indicated by red arrows. Except the notable slip bands, there are many others with very small slip steps generated. Again, there is no difference in the surface morphology with different sizes. The effect of size on the step size and the distribution of slip bands can be ignored.

In Fig. 4.6.2, stress-strain curves obtained with different sizes (10μm, 8μm and 5μm in top diameter) have similar shapes with a relatively high strain hardening rate, compared to the above results. In addition, stress-strain curves are very smooth.

Accurate values of the average yield stress (0.2% proof point) and CRSS are obtained. The average yield stresses (0.2% proof point) of 10μm, 8μm and 5μm-sized micro-pillars are 1131 (±28) MPa, 1164 (±18) MPa and 1170 (±11) MPa, respectively corresponding to CRSS values of 554 (±14) MPa, 570 (±9) MPa and 573 (±5) MPa. With the size decreasing, yield stress and CRSS increase gradually. All yield stresses and CRSS values are summarized in Table 4.6.1.

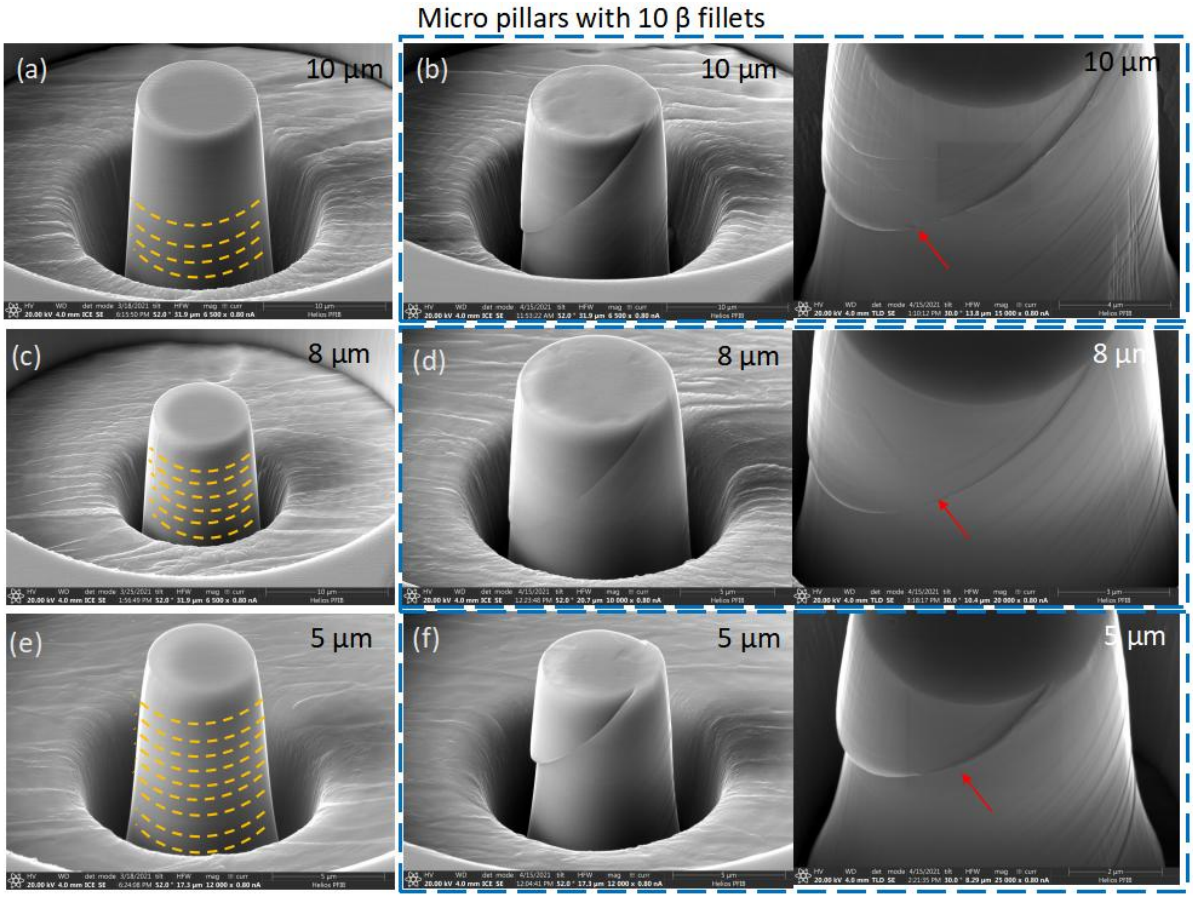

Fig. 4.6.1 SEM images of surface morphology before and after micro-compression from 10µm, 8µm and 5µm micro-pillars with 10 β phases along the direction of [02 $\bar{2}\bar{1}$] for pyramidal <a_3> slip (β phase is indicated by orange dash lines). (a), (c)and (e) are the micro-pillar images of 10µm, 8µm and 5µm pillars before compression, while (b), (d) and (f) are the images of 10µm, 8µm and 5µm pillars after compression with about 4% of strain. Only one significant slip band can be observed. Beside one major slip band can be found, many slip bands with small shearing also occur. Small slip steps are indicated by red arrows.

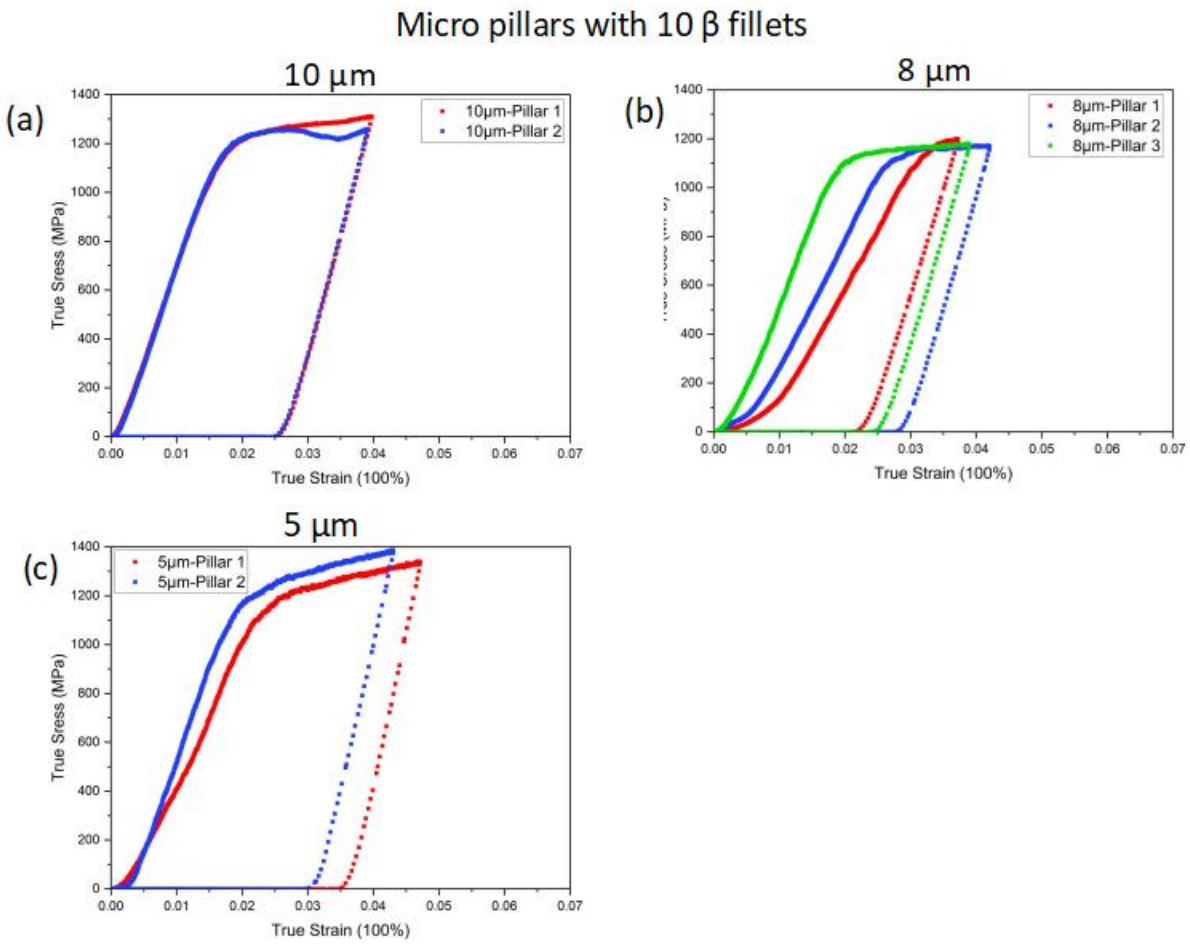

Fig. 4.6.2 Stress- strain curves after micro-compression of micro-pillars with 10 β phase fillets for pyramidal <a_3> slip: (a) 10 µm in diameter; (b) 8 µm in diameter; (c) 5 µm in diameter.

Table 4.6.1. Summary of 0.2 proof stress ($R_{p0.2}$) and the critical resolved shear stress (τ_{CRSS}) for pyramidal <a_3> slip with different sizes of micro-pillars.

No. of β	Primary slip	M_{max}	$R_{p0.2}$ (MPa)			τ_{CRSS} (MPa)		
			10 µm	8 µm	5 µm	10 µm	8 µm	5 µm
10 β	<a_3> Pyramidal	0.490	1131(±28)	1164(±18)	1170(±11)	554(±14)	570(±9)	573(±5)

4.6.2 Slip System Analysis Using the TEM

TEM is used to analyse slip band distribution, slip systems after deformation, the morphology of slip steps and β phase as well as interaction of dislocations with α/β interfaces for the deformed micro-pillars containing 10 β fillets for pyramidal <a_3> slip. The TEM foil is extracted from 10µm-sized micro-pillars with a strain of about 4%.

In Fig. 4.6.4, a TEM overview image taken under a multiple-beam condition along ~BD $[1\bar{2}1\bar{3}]$ of cross-section from micro-pillars illustrates the inhomogeneous distribution of β phase. As is indicated by the red dashed rectangle, it is an area of β phase with a high dense, whereas the low-dense area of β phase is shown as a blue dashed rectangle. The major shear bands are highlighted by the orange dashed rectangles. In areas with many β phases, few dislocations can be found. Inversely, massive dislocations occur in areas with less β phases, as is indicated by blue dashed rectangles. This is possibly because interfaces strongly hinder the dislocation movement. In addition, no big slip steps can be observed.

In Fig. 4.6.5, visibility and invisibility criteria are achieved to determine the dislocation type. Dislocations and β phase are indicated by orange dashed lines and blue arrows. As is shown in Fig. 4.6.5 (a), a two-beam condition with BD~ $[1\bar{2}1\bar{3}]$ and g vector of $\bar{1}010$ is selected, where dislocations are visible. However, with the conditions of g = $1\bar{1}01$, BD~ $[1\bar{2}1\bar{3}]$ and g = $1\bar{1}0\,0$ BD~ $[\,\bar{1}\bar{1}2\bar{3}\,]$, dislocations become invisible, which indicates that the type of dislocations is $<a_3>$ a/3$[\bar{1}\bar{1}20]$. Additionally, the slip plane can be determined as pyramidal plane $(\bar{1}10\bar{1})$, as all dislocations are edge-on, which means that the slip plane is edge-on with normal direction of $[\,\bar{1}\,1\,0\bar{1}\,]$. So, the slip system can be determined as pyramidal $<a_3>$ a/3$[\bar{1}\bar{1}20]$ $(\bar{1}10\bar{1})$. The visibility and invisibility criteria for different two-beam conditions are listed in Table 4.6.2.

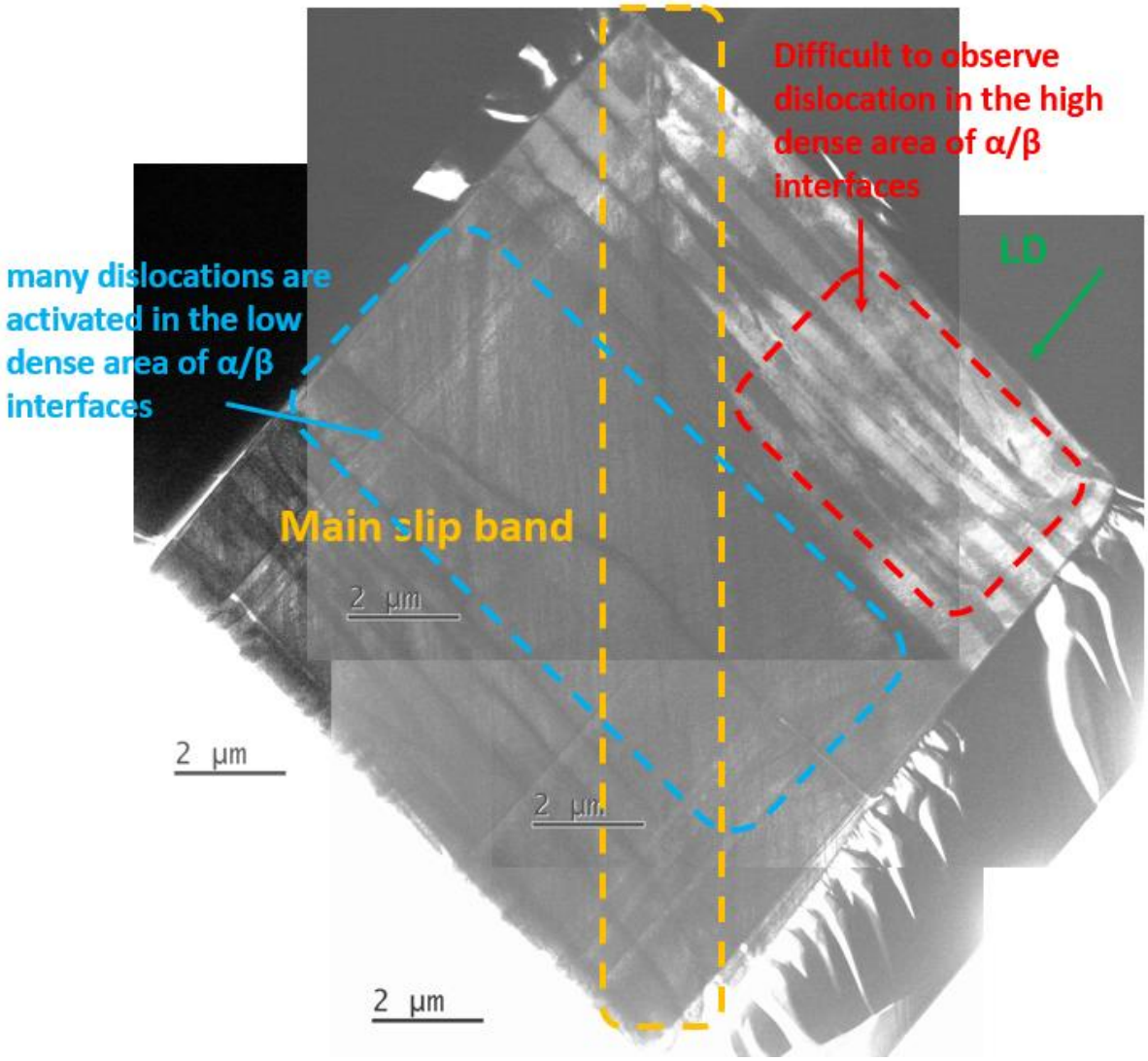

Fig. 4.6.4 An overview of TEM image from deformed micro-pillars with 10 β fillets to about 3% of strain for pyramidal <a_3> slip in a multiple beam condition with BD~ $[1\bar{2}1\bar{3}]$*. Loading direction is indicated by green arrows. Dislocations are edge-on and shear bands distribution is not homogeneous. Except one significant slip step, there is no big slip steps.*

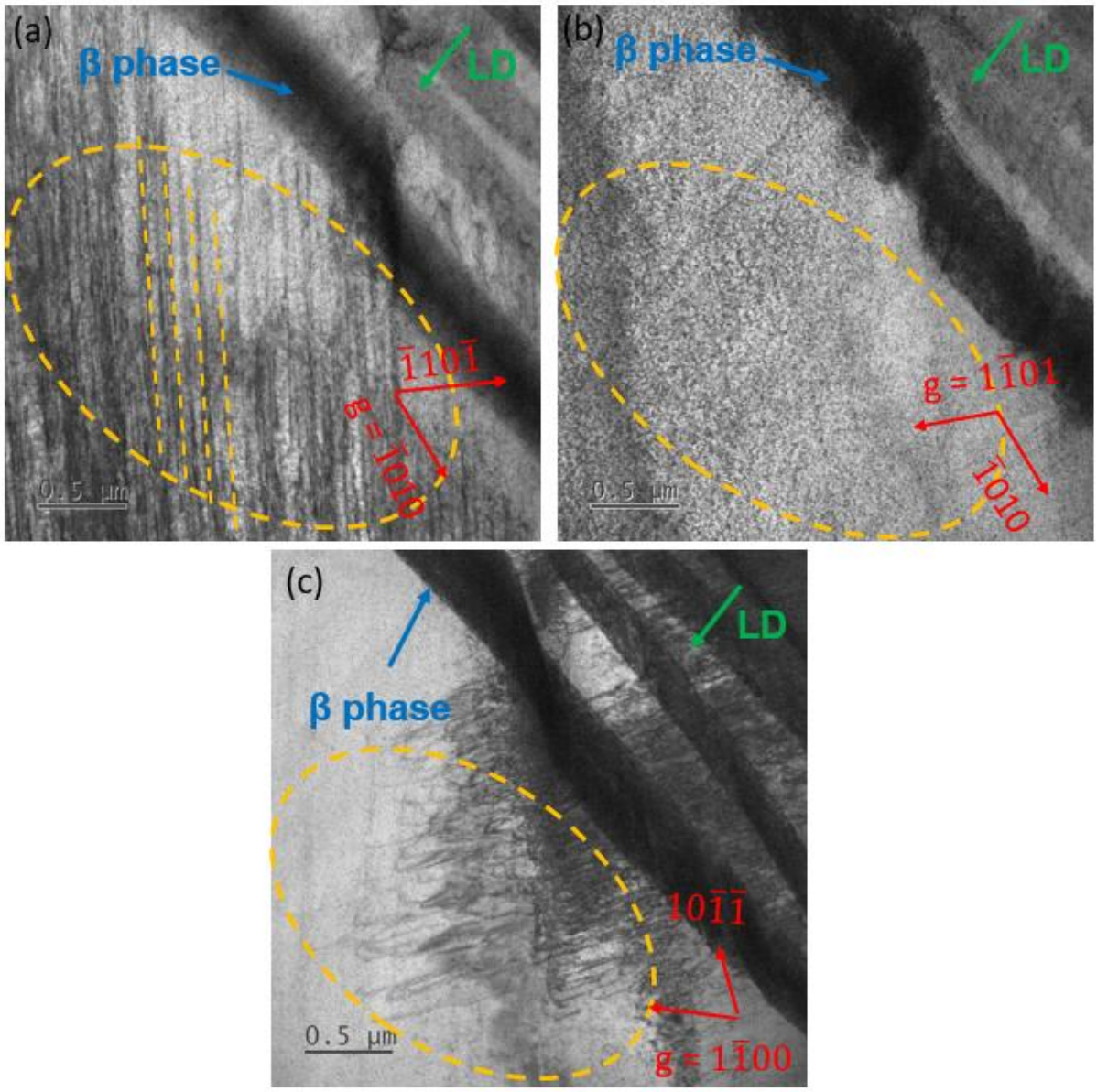

Fig. 4.6.5 Analysis of pyramidal <a_3> slip from TEM bright field images of the micro-pillars (10 β fillets inside) with a diameter of 8 μm under two-beam conditions after deformed to a strain of about 4%. Pyramidal <a_3> slip is highlighted by orange dash circles, and the loading directions are indicated by green arrows. (a) $g = \bar{1}010$, and BD~ *$[1\bar{2}1\bar{3}]$*, which are visible; *(b) $g = 1\bar{1}01$*, and BD~ *$[1\bar{2}1\bar{3}]$*, which are invisible; *(c) $g = 1\bar{1}00$*, and BD~ *$[\bar{1}\bar{1}2\bar{3}]$*, which are invisible.

Table 4.6.2. Summary of diffraction condition for pyramidal <a_3> slip.

Beam direction	g	Pyramidal <a_3> slip system a/3[$\bar{1}\bar{1}20$] ($1\bar{1}01$)
[$1\bar{2}1\bar{3}$]	$\bar{1}010$	Visible (edge on)
[$1\bar{2}1\bar{3}$]	$1\bar{1}01$	Invisible
[$\bar{1}\bar{1}23$]	$1\bar{1}00$	Invisible

4.6.3 Summary

The deformation of compressed micro-pillars containing 10 β fillets with different pillar sizes, namely 10μm, 8μm and 5μm in diameter, is studied for pyramidal <a_3> slip. The deformation behaviour of micro-pillars is released through true stress-strain curves with a strain of 4%, SEM and TEM characterizations.

The mean yield stress (0.2% proof stress) and CRSS are determined based on stress-strain curves, with relatively high strain hardening rates.

For the same number of 10 β fillets in micro-pillars, mean yield stress increases gradually while reducing the pillar size from 10μm to 5μm. The mean yield stresses are 1131 (±28) MPa, 1164 (±18) MPa and 1170 (±11) MPa, respectively corresponding to the CRSS value of 554 (±14) MPa, 570 (±9) MPa and 573 (±5) MPa. The mean yield stress and CRSS increase

by 3% when the pillar size reduces from 10μm to 5μm. The size effect on yield stress and CRSS is weaker than those pillars with fewer β fillets.

Based on a slip system analysis using TEM, only pyramidal $<a_3>$ slips are activated. The distribution of shear bands is homogeneous. The size of slip steps is very small, which is hard to be investigated.

4.7 Micro-pillars containing ~10 β Fillets Oriented for Basal $<a_1>$ Slip

The deformation behaviour of micro-pillars containing 10 β fillets for the basal $<a_1>$ slip with a Schmid factor of 0.441 is studied in this section. All pillars are fabricated from Grain 3 with a loading direction of $[2\bar{1}\bar{1}3]$.

4.7.1 Surface Morphology of the Deformed Micro-pillars and the Corresponding Stress-strain Curves

Micro-compression tests of pillars containing 10 β fillets and different sizes (10μm, 8μm and 5μm in top diameter) are performed to strains ranging from 3.5% to 6%. Fig. 4.7.1 and Fig. 4.7.2 show the surface morphology of micro-pillars before and after compression. Fig. 4.7.3 shows the true stress-strain curves with various pillar sizes. The yield stress and CRSS values obtained from 0.2% proof point are summarized in Table 4.7.1.

As is shown in Fig. 4.7.1, β phase is indicated by orange dash lines and there is only one big slip band that can be investigated at a relatively low magnification. However, in Fig. 4.7.2 (d), the big slip band is merged by many tiny slip bands and some others with tiny slip steps are formed, but they not totally go through the whole pillar, as is shown in Fig. 4.7.2 (a-c).

Similarly, there is no difference in surface morphologies with different sizes. The effect of size on the step size and distribution of slip bands can be ignored.

Differently, stress-strain curves obtained with different sizes (10μm, 8μm and 5μm in top diameter) have very high yield stresses and strain hardening rates, compared to the above results. In addition, stress-strain curves are very smooth with no load drops. Accurate values of average yield stress (0.2% proof point) and CRSS are obtained. The average yield stresses (0.2% proof point) of the 10μm, 8μm and 5μm-sized micro-pillars are 1273 (±42) MPa, 1288 (±32) MPa and 1441 (±15) MPa, respectively corresponding to CRSS values of 561 (±19) MPa, 568 (±14) MPa and 635 (±7) MPa. With the pillar size decreasing, yield stress and CRSS increase gradually. All yield stresses and CRSS values are listed in Table 4.7.1.

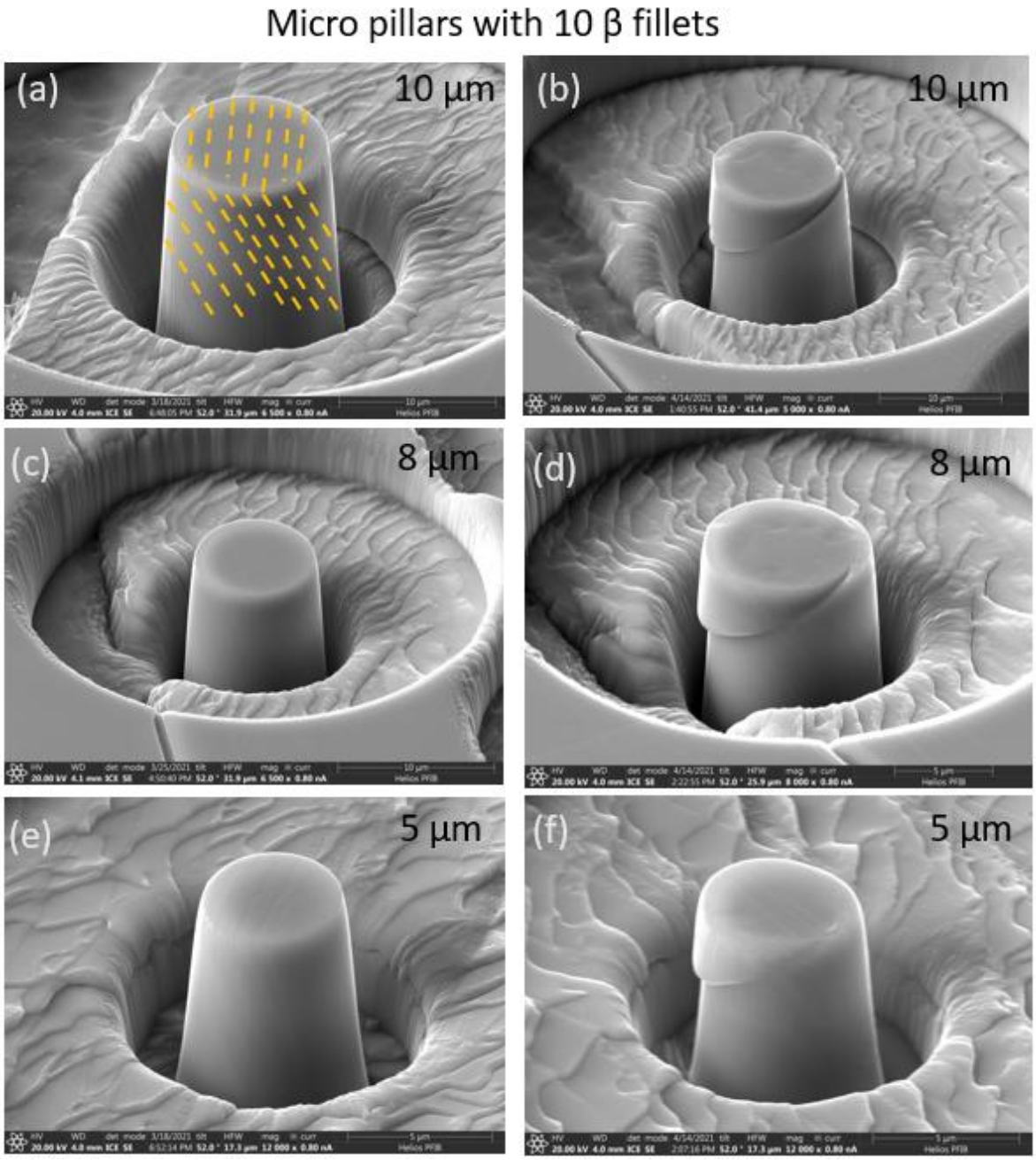

Fig. 4.7.1 SEM images of surface morphology before and after micro-compression from 10µm, 8µm and 5µm micro-pillars with 10 β phases along the direction of [$2\bar{1}\bar{1}3$] for basal <a_1> slip (β phase is indicated by orange dash lines). (a), (c)and (e) are the micro-pillar images of 10µm, 8µm and 5µm pillars before compression, while (b), (d) and (f) are the images of 10µm, 8µm and 5µm pillars after compression to strain ranging from 3.5% to 6%. Only one significant slip band can be observed at low magnification.

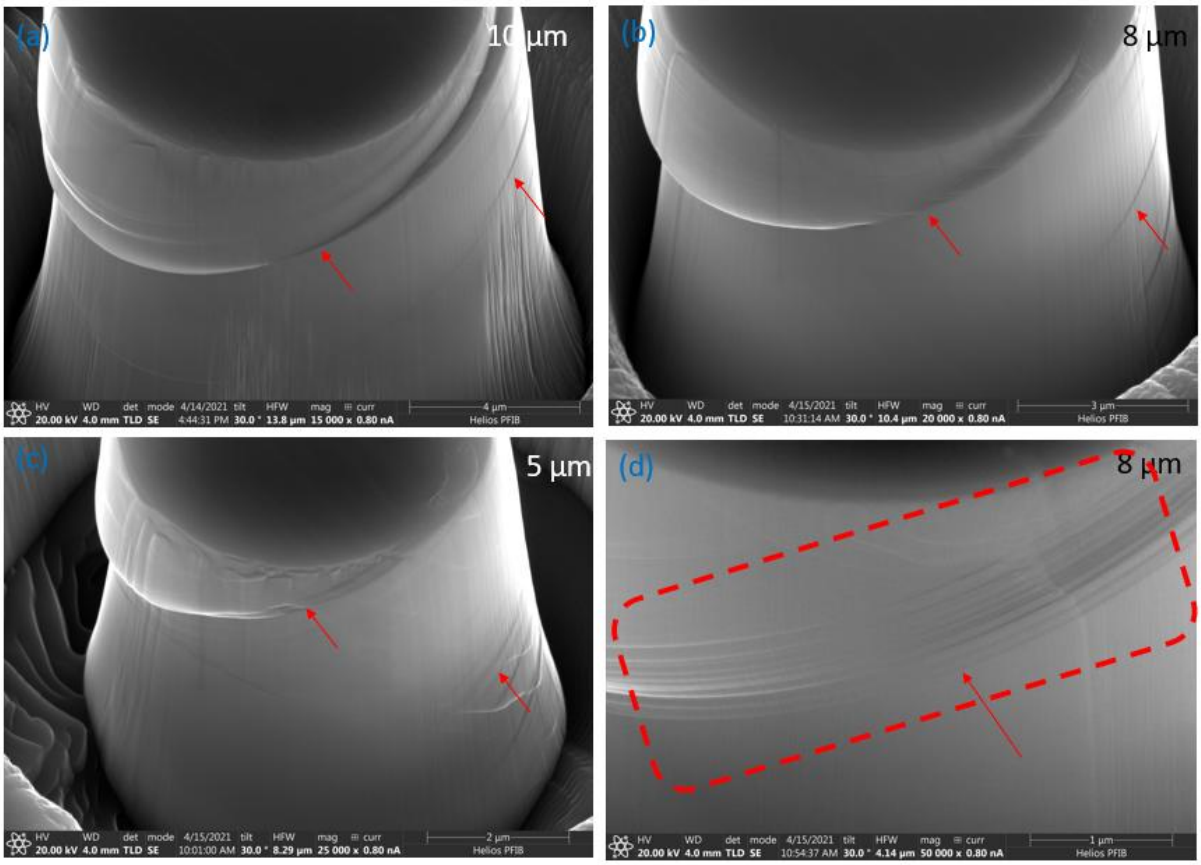

Fig. 4.7.2 SEM images at high magnifications of surface morphology after micro-compression from 10µm, 8µm and 5µm sized micro-pillars with 10 β phases along the direction of [$2\bar{1}\bar{1}3$] for basal <a_1> slip. Beside one major slip band can be found, some tiny slip bands with small shearing also occur but not transmit through the whole pillars as shown in (a-c). In (d), it shows the major slip band is formed by many tiny slip bands. Slip steps are indicated by red arrows.

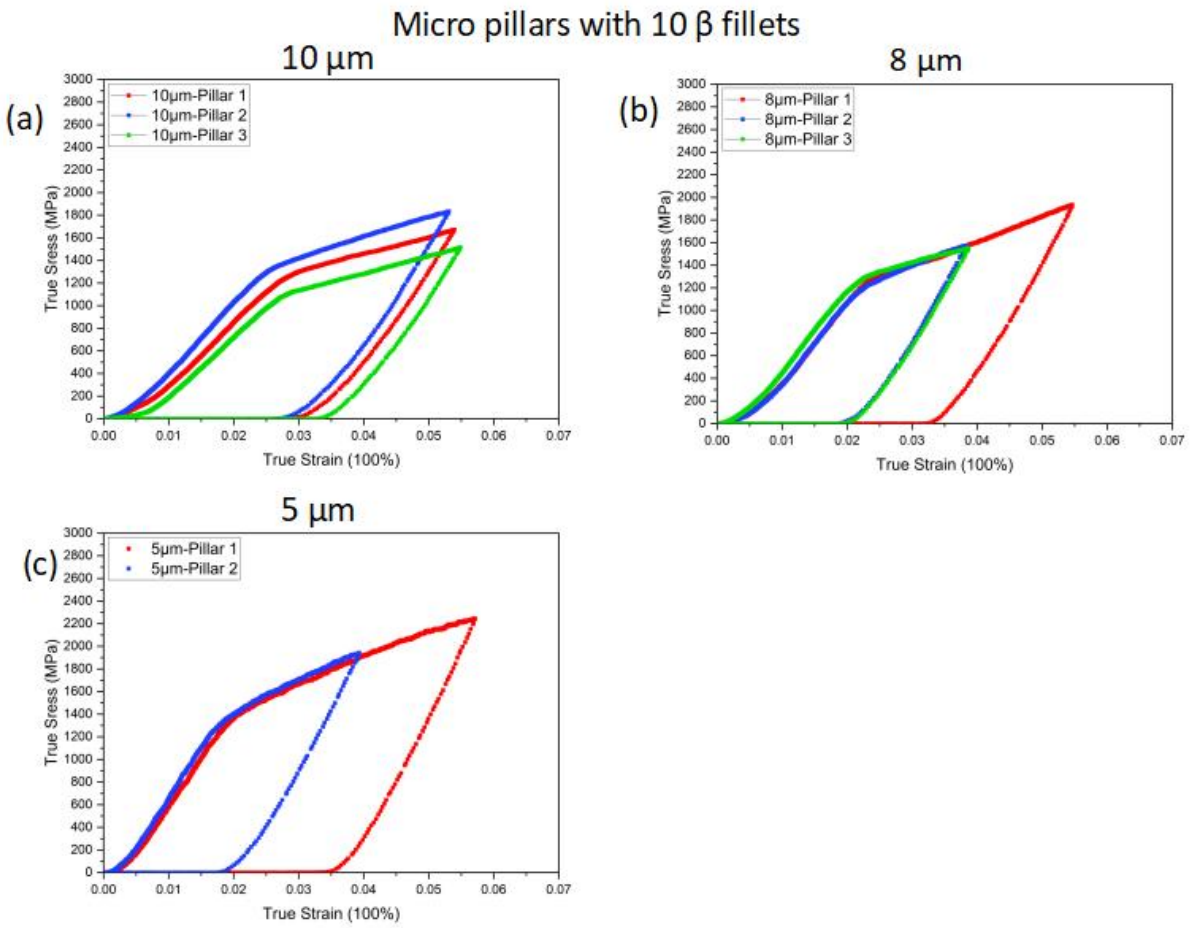

Fig. 4.7.3 Stress- strain curves after micro-compression of micro-pillars with 10 β phase fillets for basal <a_1> slip: (a) 10 µm in diameter; (b) 8 µm in diameter; (c) 5 µm in diameter.

Table 4.7.1. Summary of 0.2 proof stress ($R_{p0.2}$) and the critical resolved shear stress (τ_{CRSS}) for basal <a_1> slip with different sizes of micro-pillars.

No.	Primary slip	M_{max}	$R_{p0.2}$ (MPa)			τ_{CRSS} (MPa)		
			10 µm	8 µm	5 µm	10 µm	8 µm	5 µm
10 β	<a_1> Basal	0.441	1273(±42)	1288(±32)	1441(±15)	561(±19)	568(±14)	635(±7)

4.7.2 Slip System Analysis Using the TEM

TEM is used to analyse slip band distribution, slip systems after deformation, the morphology of slip steps and β phase, as well as interaction of dislocations with α/β interfaces for the deformed micro-pillars containing 10 β fillets after basal <a_1> slip. The TEM foil is extracted from 8µm-sized micro-pillars with a strain of about 6%.

In Fig. 4.7.4, a TEM overview image taken in a multiple-beam condition with ~BD $[1\bar{2}1\bar{3}]$ and g = 0001 shows the homogenous distribution of β phase, and only one major shear band is investigated, as is indicated by the orange dashed rectangle. Additionally, the slip step is not sharp, which is curved due to the accumulation and concentration of many tiny shear bands.

In Fig. 4.7.5, visibility and invisibility criteria are achieved to identify the dislocation type. Dislocations and β phase are indicated by orange dashed lines and blue arrows. As is shown in Fig. 4.7.5 (a), a two-beam condition with BD~ $[0\bar{1}10]$ and g vector of $2\bar{1}\bar{1}0$ is selected, where dislocations are visible. However, under the conditions with g = 0002, BD~

$[0\bar{1}10]$ and g = $02\bar{2}\bar{1}$ BD~ $[\bar{2}110]$, dislocations are out of contrast. The dislocations are identified as $<a_1>$ a/3 $[2\bar{1}\bar{1}0]$. Additionally, the slip band in Fig. 4.7.4 highlighted by an orange dashed rectangle becomes the narrowest, which is edge-on. So, the slip plane can be identified as pyramidal plane (0002), and the slip system can be determined as basal $<a_1>$ a/3$[2\bar{1}\bar{1}0]$ (0002). The visibility and invisibility criteria for different two-beam conditions are summarized in Table 4.7.2.

In Fig. 4.7.6, the interaction between dislocations and interfaces is investigated under a two-beam condition with g = $2\bar{1}\bar{1}0$ and BD~ $[0\bar{1}10]$. β phase is indicated by blue dashed lines. As can be seen, when dislocations go through interfaces, their number decreases dramatically, which can't reach the side surface. This illustrates that slip bands are formed but cannot go through the whole pillar, as is shown in SEM images.

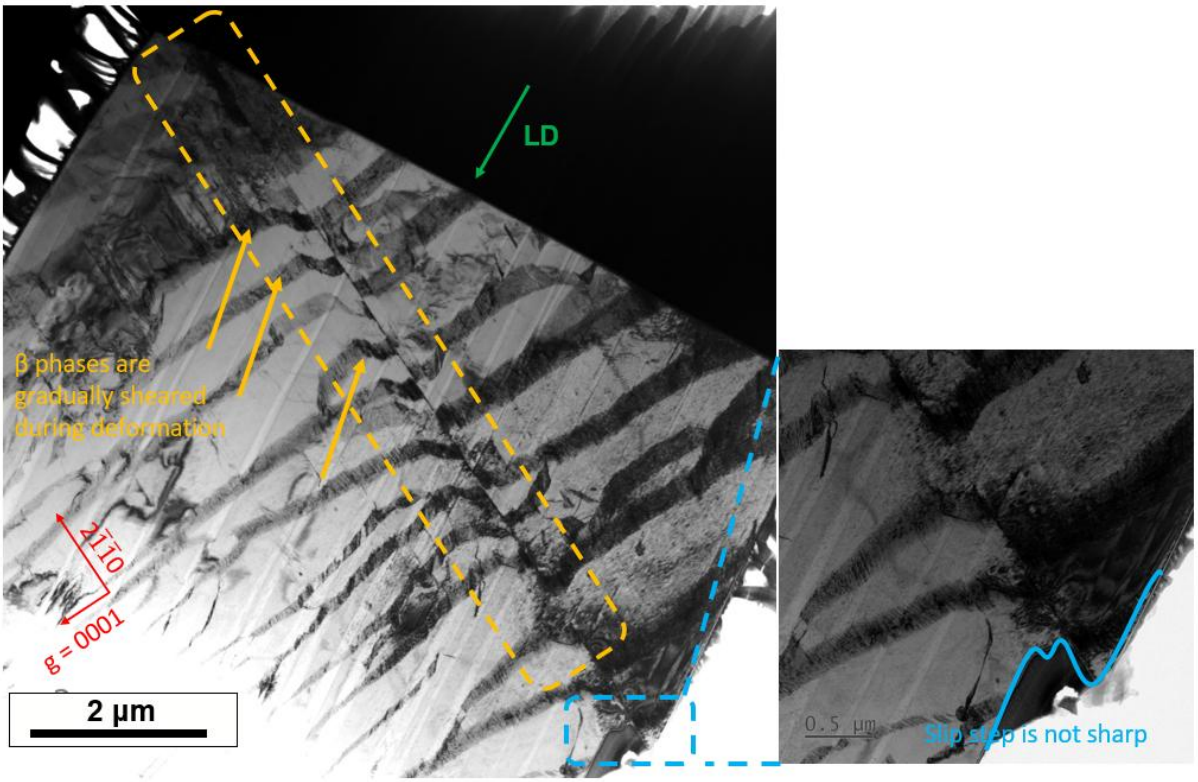

Fig. 4.7.4 An overview of TEM image from deformed micro-pillars with 10 β fillets to about 6% of strain for basal <a_1> slip in a two-beam condition with BD~ [$1\bar{2}1\bar{3}$], and g = 0002. Loading direction is indicated by green arrows. Dislocations are out of contrast and shear bands distribution is homogeneous. The slip step is not sharp.

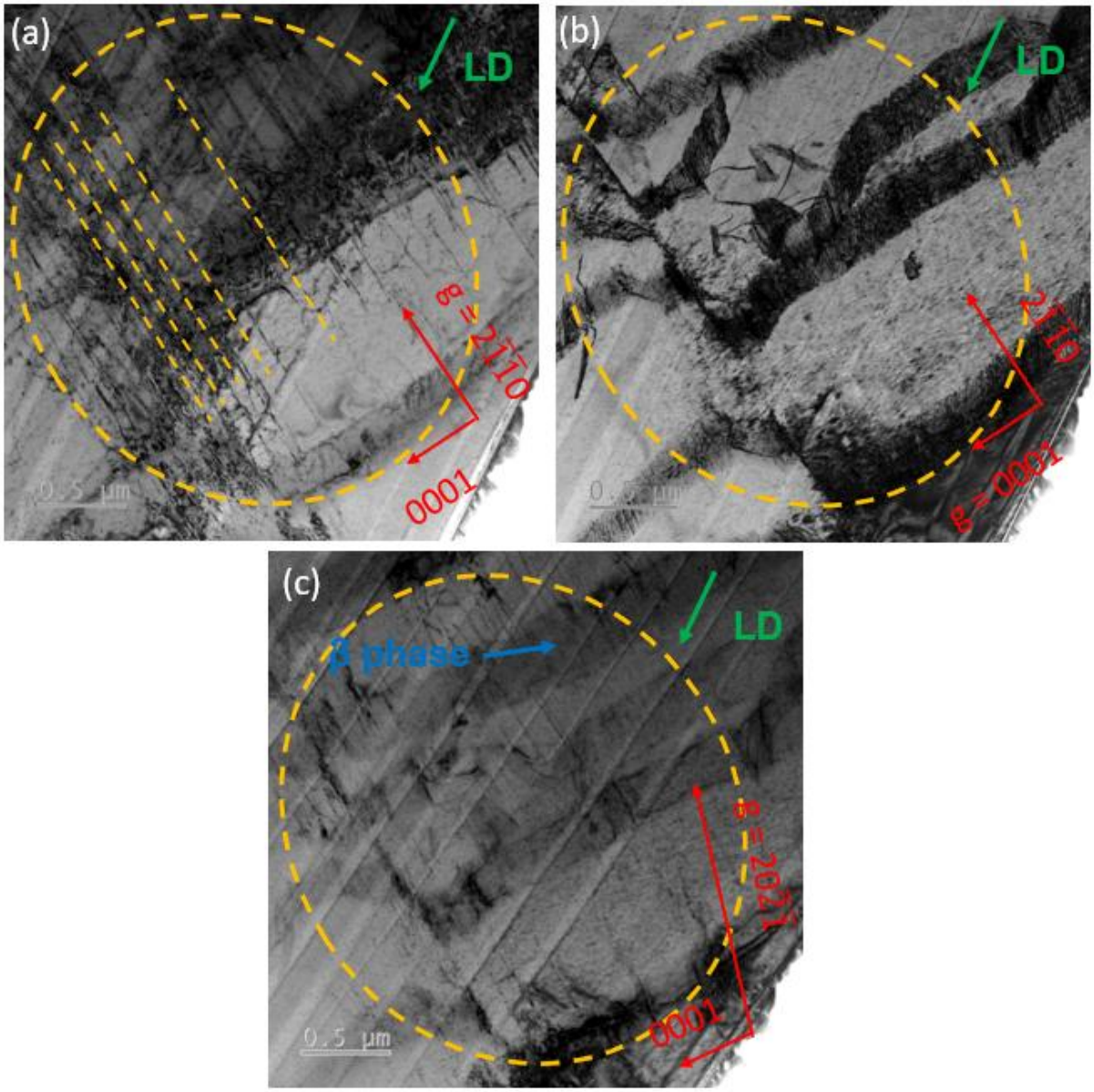

Fig. 4.7.5 Analysis of basal <a_1> slip from TEM bright field images of the micro-pillars (10 β fillets inside) with a diameter of 8 μm under two-beam conditions after deformed to a strain of about 6%. Basal <a_1> slip is highlighted by orange dash circles, and the loading directions are indicated by green arrows. (a) g = $2\bar{1}\bar{1}0$, and BD~ *[*$0\bar{1}10$*]*, which are visible; *(b) g = 0002*, and BD~ *[*$0\bar{1}10$*]*, which are invisible; *(c) g =* $02\bar{2}\bar{1}$, and BD~ *[*$\bar{2}110$*]*, which are invisible.

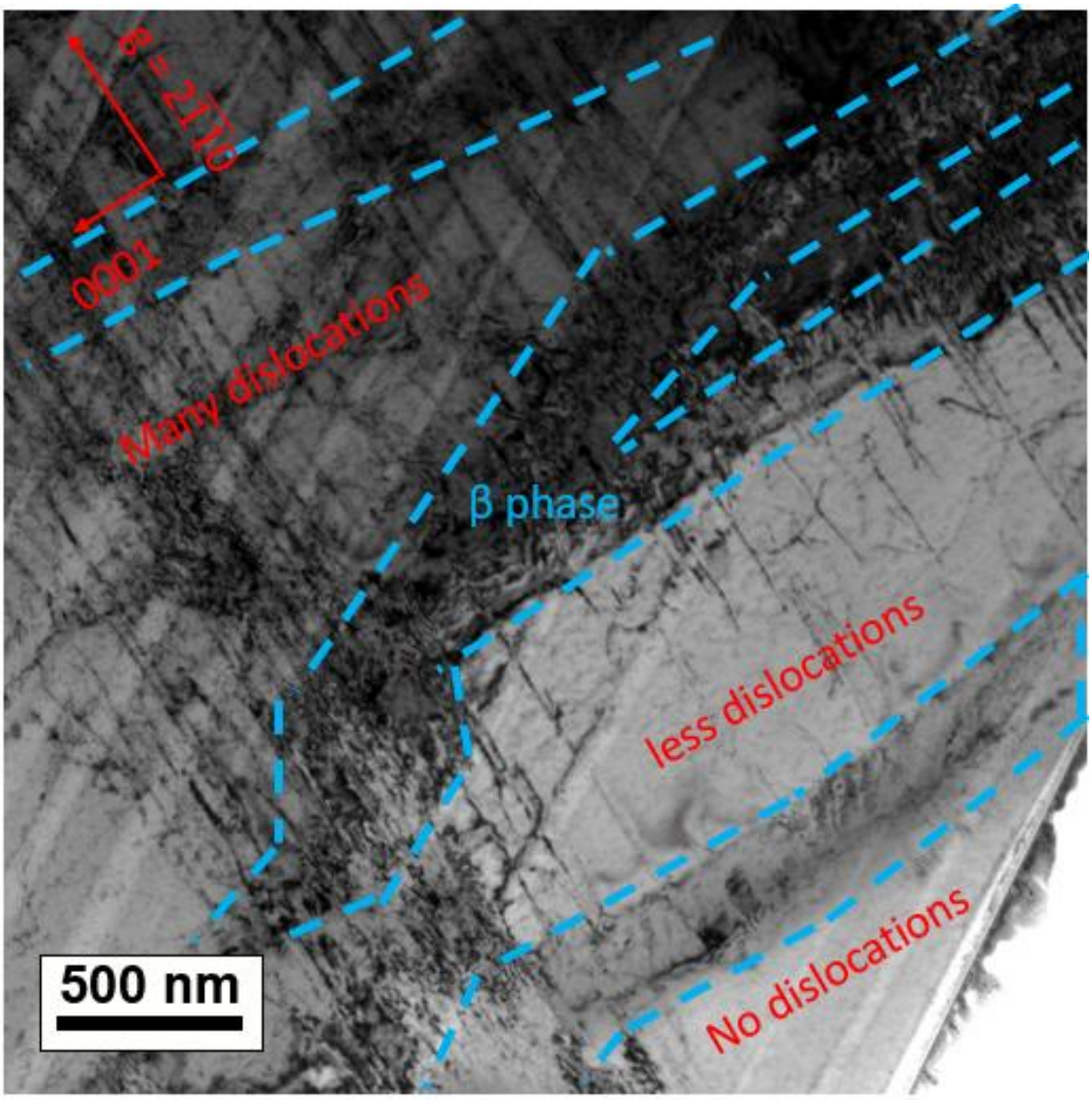

*Fig. 4.7.6 TEM images of interactions between dislocations and α/β interfaces from deformed micro-*pillars for about 6% of strain for *basal <a1> slip under* two-beam condition $g = 2\bar{1}\bar{1}0$, *and BD~* $[0\bar{1}10]$*. Loading and slip directions are indicated by green and orange arrows. Dislocations are impended by the interfaces and cannot reach the side surface. β phase is indicated by blue dashed lines.*

Table 4.7.2. Summary of diffraction condition for basal <a_1> slip.

Beam direction	g	basal <a1> slip system a/3[$2\bar{1}\bar{1}0$] (0001)
[$0\bar{1}10$]	$2\bar{1}\bar{1}0$	Visible (edge on)
[$0\bar{1}10$]	0002	Invisible
[$\bar{2}110$]	$02\bar{2}\bar{1}$	Invisible

4.7.3 Summary

The deformation of compressed micro-pillars containing 10 β fillets with different sizes, namely 10µm, 8µm and 5µm in diameter, is studied for basal <a_1> slip. The deformation behaviour of micro-pillars is released through true stress-strain curves with a strain ranging from 3.5% to 6%, SEM and TEM characterizations.

The mean yield stress (0.2% proof stress) and CRSS are determined by stress-strain curves. High yield stresses and CRSS values are obtained. Also, the strain hardening rate is very large. Stress-strain curves are very smooth without any load drop.

Mean yield stress increases gradually while reducing the pillar size from 10µm to 5µm. The mean yield stresses are 1273 (±42) MPa, 1288 (±32) MPa and 1441 (±15) MPa, respectively corresponding to CRSS values of 561 (±19) MPa, 568 (±14) MPa and 635 (±7) MPa. The mean yield stress and CRSS increase by 13% when the pillar size reduces from 10µm to 5µm.

Based on a slip system analysis using the TEM, only basal <a_1> slips are activated. The distribution of shear bands is homogeneous, which also accumulate to form a big shear band and curved big step that is not as sharp as those of a few β fillets. Additionally, some tiny shear bands are formed, but they cannot go through the whole pillar, impeded by the multiple interfaces.

4.8 Micro-pillars containing ~10 β Fillets Oriented for Basal <a_3> Slip

The deformation behaviour of micro-pillars containing 10 β fillets for the basal <a_3> slip with a Schmid factor of 0.361 is studied in this section. All pillars are fabricated from Grain 4 with a loading direction of $[\bar{2}\bar{2}49\bar{9}]$.

4.8.1 Surface Morphology of the Deformed Micro-pillars and the Corresponding Stress-strain Curves

Micro-compression tests on pillars containing 10 β fillets and different sizes (10μm, 8μm and 5μm in top diameter) are performed with strains ranging from 5% to 7%. Fig. 4.8.1 and Fig. 4.8.2 show the surface morphology of micro-pillars before and after compression. Fig. 4.8.3 shows the true stress-strain curves with different sizes. The yield stress and CRSS values obtained from 0.2% proof point are summarized in Table 4.8.1.

Similar to the results of basal <a_1> slip activation, there is only one big slip band that can be investigated at a relatively low magnification, and β phase is indicated by orange dash lines, as is shown in Fig. 4.8.1. However, in Fig. 4.7.2 (a-d), the big slip band is merged by many tiny slip bands. Similarly, there is no difference in surface morphologies with different sizes. The effect of size on the step size and distribution of slip bands is very limited.

As for the stress-strain curves, there are relatively large variations which may be caused by the complicated distribution of β phase inside the pillars. Stress-strain curves obtained with different sizes (10μm, 8μm and 5μm in top diameter) have very high strain hardening rates and yield stresses, compared to the results of pillars containing few β fillets. Additionally, stress-strain curves are very smooth with no load drops. Accurate values of the average yield stress (0.2% proof point) and CRSS are obtained. The average yield stresses (0.2% proof point) of 10μm, 8μm and 5μm-sized micro-pillars are 1870 (±117) MPa, 1913 (±131) MPa and 1936 (±116) MPa, respectively corresponding to CRSS values of 675 (±42) MPa, 691 (±47) MPa and 699 (±42) MPa. With the size decreasing, yield stress and CRSS increase gradually. All yield stresses and CRSS values are listed in Table 4.8.1.

In Fig. 4.8.4, SEM images of (a-c) corresponds to stress-strain curves in Fig.4.8.3 (b). It can be observed that the β fillet distribution of pillar 1 is homogeneous. However, β fillets of pillar 2 mainly distribute at two sides of the micro-pillar and that of pillar 3 mainly distribute at the centre of the micro-pillar. The difference in β fillet distribution is the main reason why stress-strain curves in Fig.4.8.3 (b) have big differences.

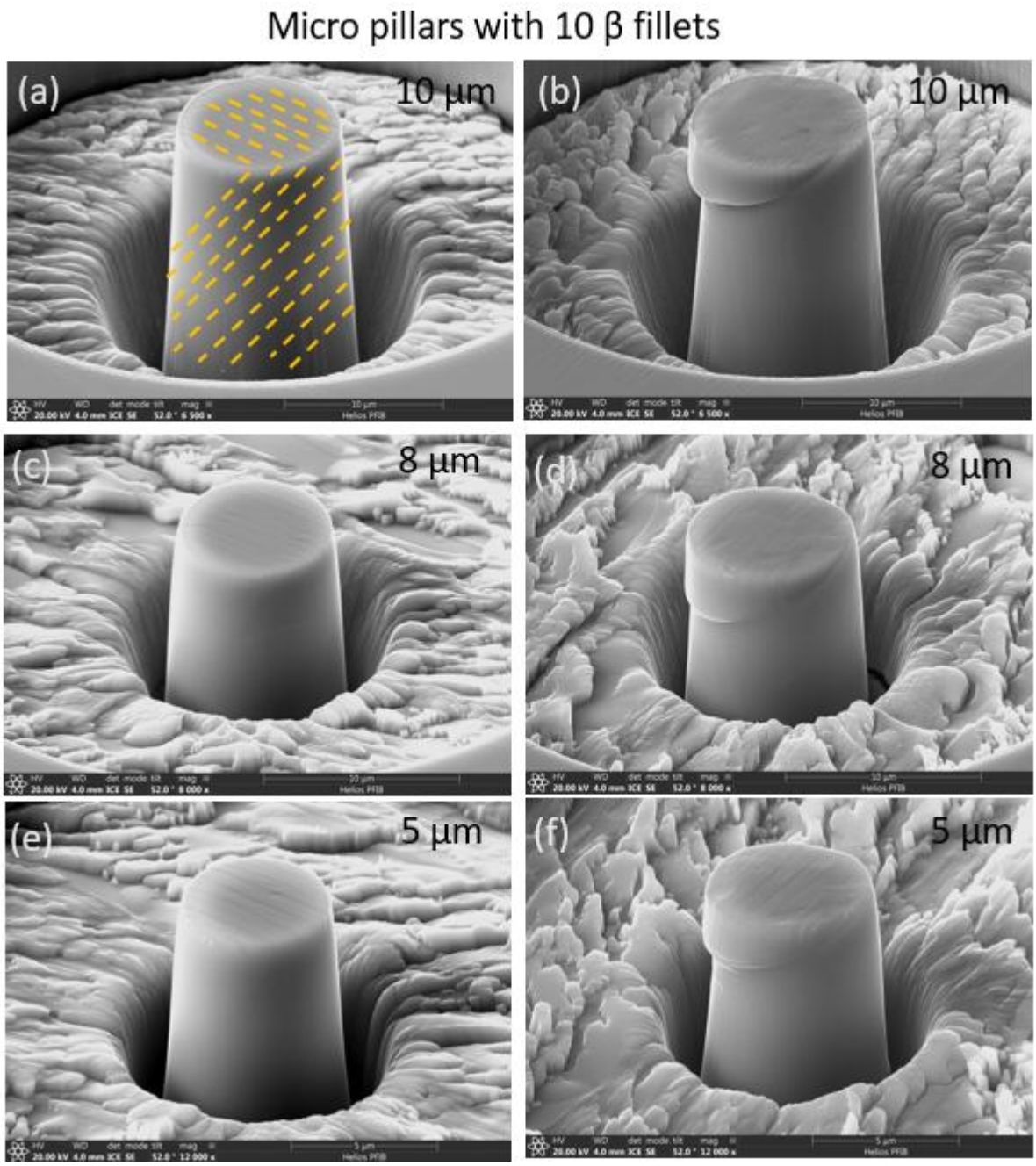

Fig. 4.8.1 SEM images of surface morphology before and after micro-compression from 10µm, 8µm and 5µm micro-pillars with 10 β phases along the direction of [$\bar{2}\bar{2}4\bar{9}$] for basal <a_3> slip (β phase is indicated by orange dash lines). (a), (c)and (e) are the micropillar image of 10µm, 8µm and 5µm pillars before compression, while (b), (d) and (f) are the images of 10µm, 8µm and 5µm pillars after compression to strain ranging from 5% to 7%. Only one significant slip band can be observed at low magnification.

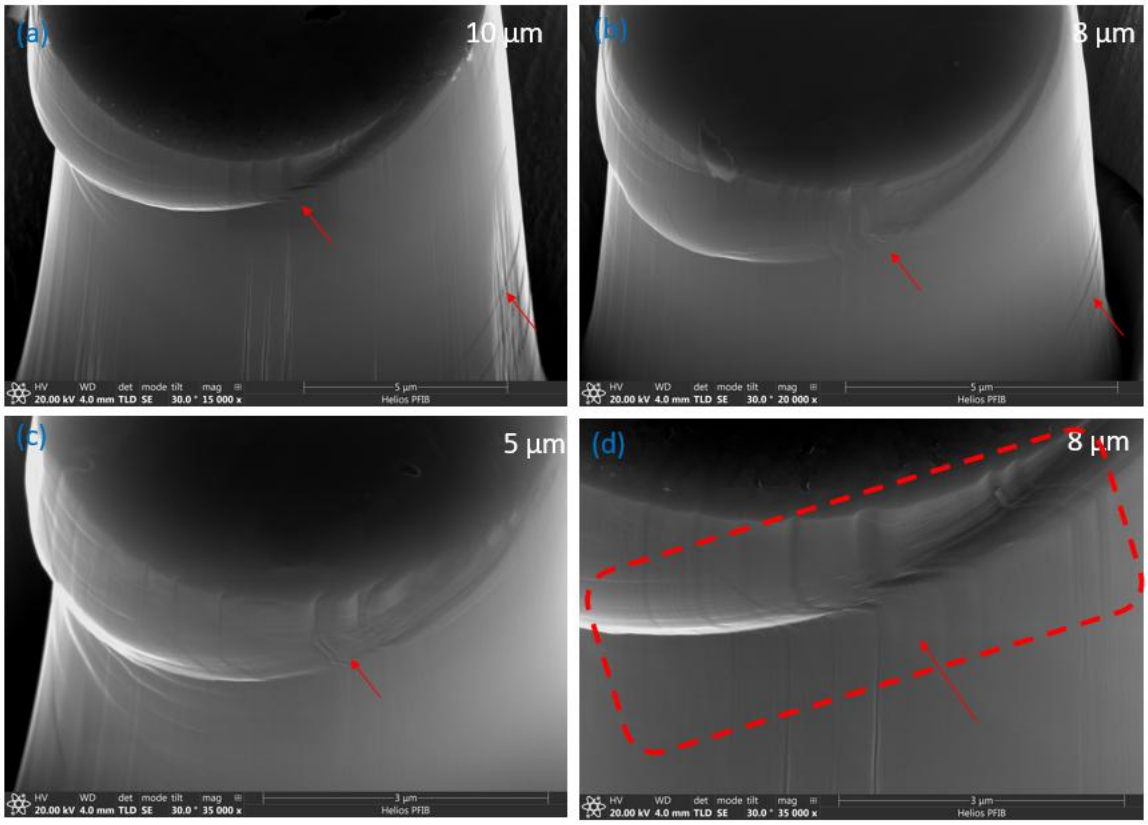

Fig. 4.8.2 SEM images at high magnifications of surface morphology after micro-compression from 10µm, 8µm and 5µm sized micro-pillars with 10 β phases along loading direction of $[\bar{2}\bar{2}49\bar{9}]$ for basal <a_3> slip. Beside one major slip band can be found, some tiny slip bands with small shearing also occur as shown in (a-c). In (d), it shows the major slip band is formed by many tiny slip bands. All imaged are taken at tilted angle of 30° and slip bands are indicated by red arrows.

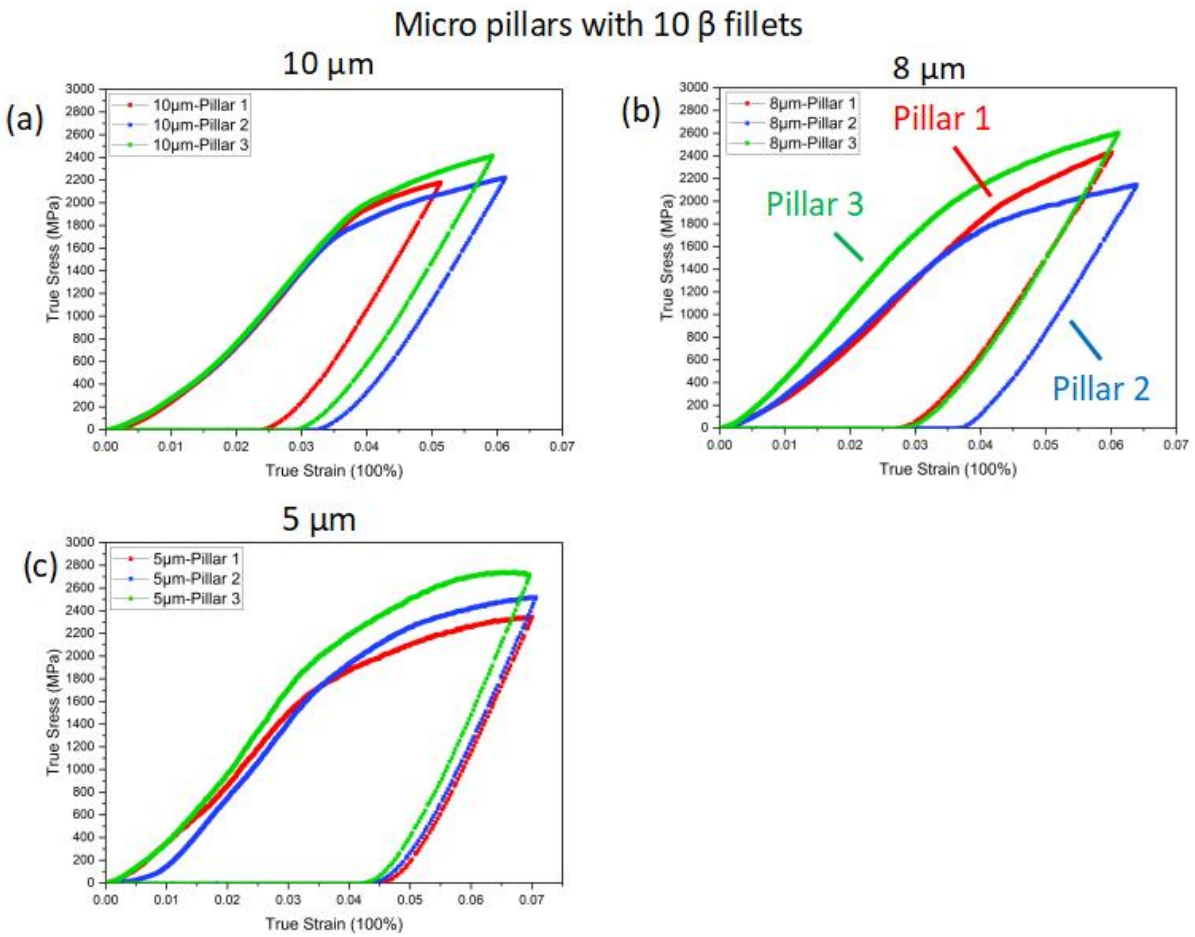

Fig. 4.8.3 Stress- strain curves after micro-compression of micro-pillars with 10 β phase fillets for basal <a_3> slip: (a) 10 µm in diameter; (b) 8 µm in diameter; (c) 5 µm in diameter.

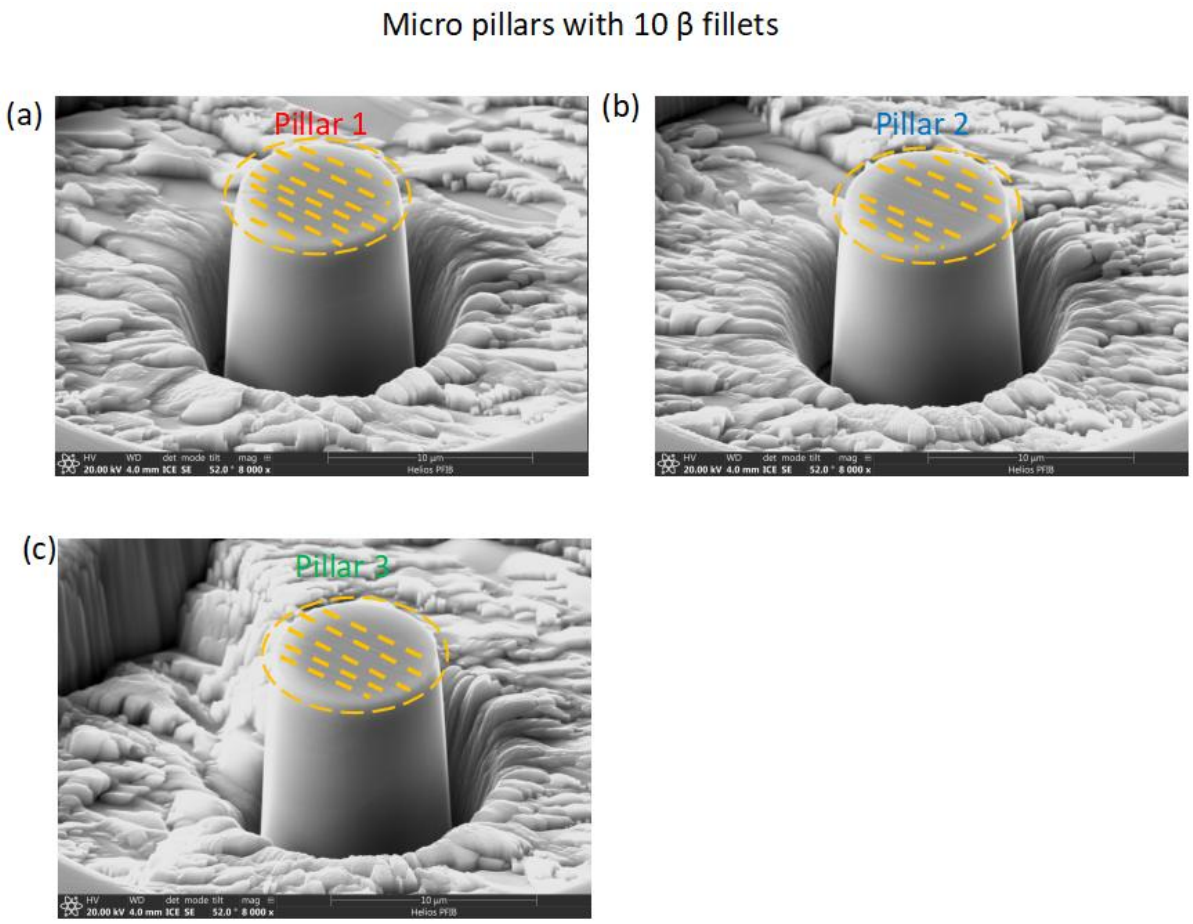

Fig. 4.8.4 SEM images of micro-pillars corresponding to stress-strain curves in Figure 4.8.3 (a) for Pillar 1-3. The micro-structure indicated by yellow dashed circles differs.

Table 4.8.1. Summary of 0.2 proof stress ($R_{p0.2}$) and the critical resolved shear stress (τ_{CRSS}) for basal <a_3> slip with different sizes of micro-pillars.

No.	Primary slip	M_{max}	$R_{p0.2}$ (MPa)			τ_{CRSS} (MPa)		
			10 μm	8 μm	5 μm	10 μm	8 μm	5 μm
10 β	<a_1> Basal	0.361	1870(±117)	1913(±131)	1936(±116)	675(±42)	691(±47)	699(±42)

4.8.2 Slip System Analysis Using the TEM

TEM is used to analyse slip systems after deformation, the morphology of slip steps for the deformed micro-pillars containing 10 β fillets for basal <a_3> slip. The TEM foil is extracted from 8μm-sized micro-pillars with a strain of about 6%.

In Fig. 4.8.5, visibility and invisibility criteria are achieved to identify the dislocation type. Dislocations and β phase are indicated by blue arrows. As is shown in Fig. 4.8.5 (a), a two-beam condition with BD~ $[1\bar{1}00]$ and g vector of $\bar{1}\bar{1}20$ is selected, where dislocations are visible. However, under conditions with g = 0002, BD~ $[1\bar{1}00]$ and g = $1\bar{1}0\bar{4}$, BD~ $[2\bar{2}01]$, dislocations are out of contrast. The dislocations are identified as <a_3> a/3 $[\bar{1}\bar{1}20]$. Additionally, the slip band in Fig. 4.8.5 is the narrowest, which is edge-on. So, the slip plane can be identified as basal plane (0002), and the slip system can be determined as basal <a_3> a/3$[\bar{1}\bar{1}20]$ (0002). The visibility and invisibility criteria for different two-beam conditions are summarized in Table 4.8.2.

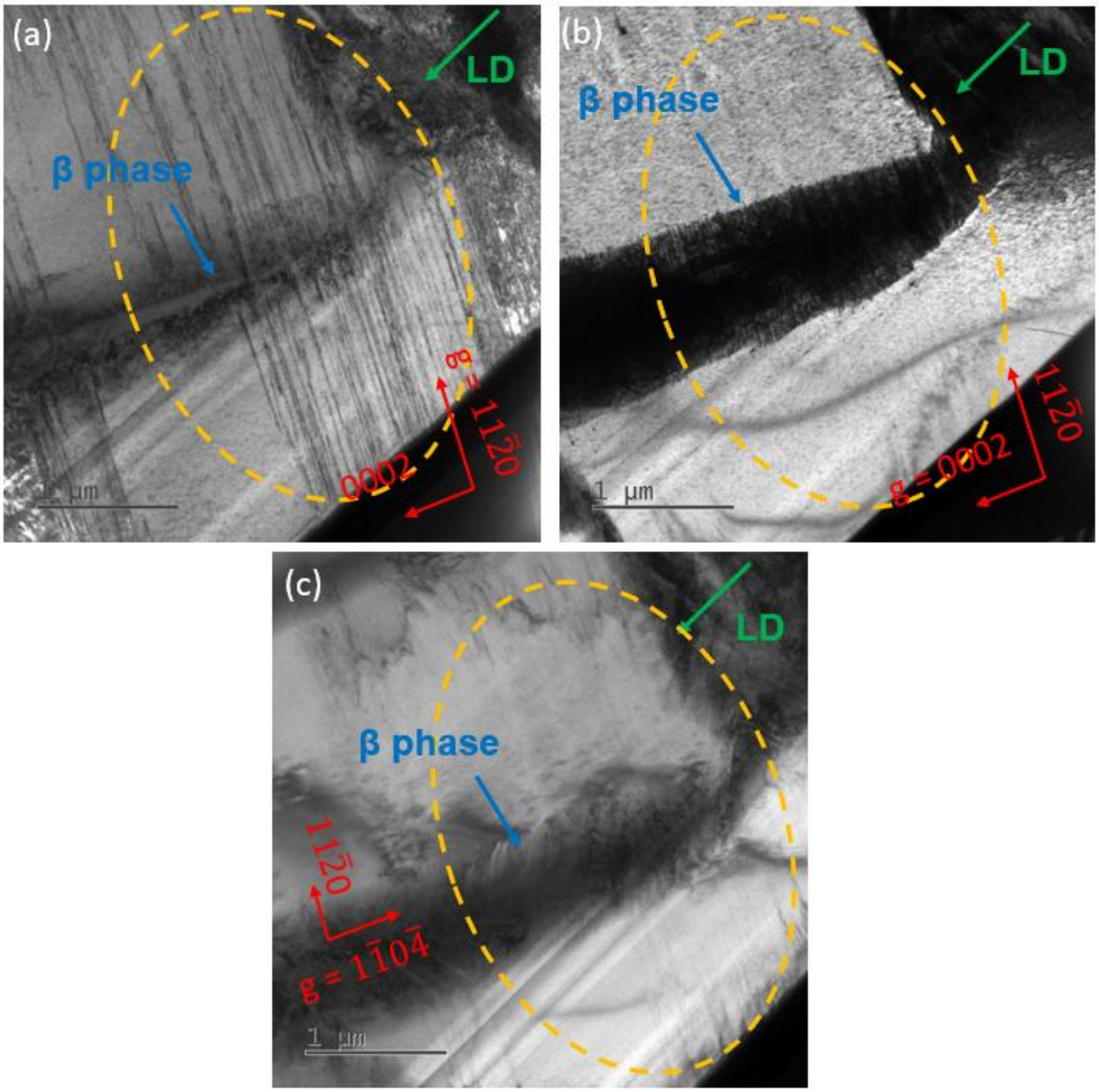

Fig. 4.8.5 Analysis of basal <a_3> slip from TEM bright field images of the micro-pillars (10 β fillets inside) with a diameter of 8 μm under two-beam conditions after deformed to a strain of about 6%. Basal <a_3> slip is highlighted by orange dash circles, and the loading directions are indicated by green arrows. (a) g = $\bar{1}\bar{1}20$, and BD~ *[*$1\bar{1}00$*]*, which are visible; *(b) g = 0002*, and BD~ *[*$1\bar{1}00$*]*, which are invisible; *(c) g =* $1\bar{1}0\bar{4}$, and BD~ *[*$2\bar{2}01$*]*, which are invisible.

Table 4.8.2. Summary of diffraction condition for basal <a_3> slip.

Beam direction	g	basal <a_3> slip system a/3[$\bar{1}\bar{1}20$] (0001)
[$1\bar{1}00$]	$\bar{1}\bar{1}20$	Visible (edge on)
[$1\bar{1}00$]	0002	Invisible
[$2\bar{2}01$]	$1\bar{1}0\bar{4}$	Invisible

4.8.3 Summary

The deformation of compressed micro-pillars containing 10 β fillets with different sizes, namely 10µm, 8µm and 5µm in diameter, is studied for basal <a_3> slip. The deformation behaviour of micro-pillars is released through true stress-strain curves with strains ranging from 5% to 7%, SEM and TEM characterizations.

The mean yield stresses (0.2% proof stress) and CRSS are determined based on stress-strain curves. A high yield stress and CRSS are obtained. Also, the strain hardening rate is very high. Stress-strain curves are very smooth without any load drop.

Mean yield stress increases gradually while reducing the pillar size from 10µm to 5µm. The mean yield stresses are 1870 (±117) MPa, 1913 (±131) MPa and 1936 (±116) MPa, respectively corresponding to CRSS values of 675 (±42) MPa, 691 (±47) MPa and 699 (±42) MPa. The mean yield stress and CRSS increase by 3.5% when the pillar size reduces from 10µm to 5µm.

Based on a slip system analysis according to TEM results, only basal <a_3> slips are activated. The distribution of shear bands is homogeneous, but accumulate together to form a big shear band and curved big step that is not as sharp as those with few β fillets. Additionally, some tiny shear bands are formed.

4.9 β Phase Volume Fraction in Micro-pillars

The volume fraction of β phase plays a significant role on the strength of dual-phase Ti-6Al-4V, since the individual strength of α and β phase differs. Normally, α phase is stronger than β phase. Thus, the yield stress and CRSS must reduce as introducing β phase in larger volume fraction into the micro-pillars.

Due to the unpredictable and inhomogeneous distribution of β phase inside pillars, the area fraction of β phase from cross-section instead of top surface is calculated using image J software to represent the volume fraction of β phase. In Fig. 4.9.1, it is obvious that the distribution of β phase inside pillars is very hard to predict from top surface, as is indicated by red areas. So, it is essential to use the cross-section for estimation. As is summarized in Table 4.9.1, the volume fractions of β phase for prismatic <a_3> slip with 0, 1 and 2 β fillets are 0, 1.56% and 9.46% respectively. For prismatic <a_2> slip of micro-pillars containing 2 β fillets, the volume fraction of β phase is 6.89%. As to the micro-pillars for pyramidal <a_3>, basal <a_1> and basal <a_3> slip containing 10 β fillets, the volume fractions of β phase are 47.79%, 38.48% and 34.39% respectively. Those pillars with more β fillets apparently have larger β phase volume fractions.

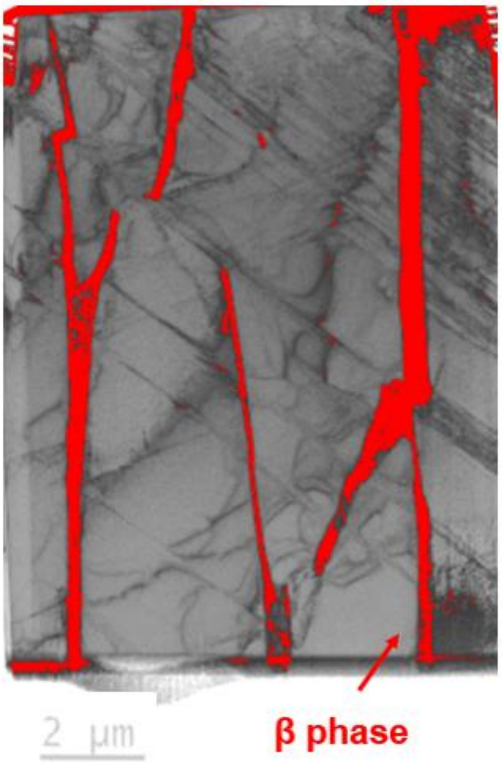

Fig. 4.9.1 The cross-section of micro-pillars for estimating the volume fraction of β phase. The distribution of β phase inside pillars is unpredictable from the top surface.

Table 4.9.1. Summary of volume fraction of β phase in micro-pillars for different amount of β fillets and slip systems.

No. of β fillets	0	1	2	2	10	10	10
Slip system	Prismatic <a_3>	Prismatic <a_3>	Prismatic <a_3>	Prismatic <a_2>	Pyramidal <a_3>	Basal <a_1>	Basal <a_3>
Volume fraction	0	1.56%	9.46%	6.89%	47.79%	38.48%	34.39%

Chapter 5 Discussion

5.1 Summary of Yield Stress and CRSS

In order to have a better understanding of the effect of α/β interfaces on strengthening, results of all yield stresses and CRSS presented in Chapter 5 for different pillar sizes, different numbers of β fillets and different slip systems are summarized in Table 5.1.1.

There is an obvious trend that the CRSS of micropillars increases with an increasing number of β fillets or α/β interfaces for the same prismatic $<a_3>$ slip. Additionally, with the same number of β fillets, which is 2, the CRSS for prismatic $<a_3>$ slip is larger than that of prismatic $<a_2>$ slip. Furthermore, with the same number of β fillets, which is 10, the CRSS of basal $<a_3>$ slip is larger than that of basal $<a_1>$ and pyramidal $<a_3>$ slip.

Table 5.1.1. Summary of yield stress and CRSS for different pillar sizes, different numbers of of β fillets and different slip systems

No. of β fillets	0	1	2	2	10	10	10
Slip system	$<a_3>$ Prism	$<a_3>$ Prism	$<a_3>$ Prism	$<a_2>$ Prism	$<a_3>$ Pyramidal	$<a_1>$ basal	$<a_3>$ basal

Volume fraction of β phase		0	1.56%	9.46%	6.89%	47.79%	38.48%	34.39%
M_{max}		0.460	0.460	0.460	0.455	0.490	0.441	0.361
$R_{p0.2}$ (MPa)	10 μm	-	840 (±24)	941 (±21)	888 (±18)	1131 (±28)	1273 (±42)	1870 (±117)
	8 μm	923 (±14)	895 (±61)	967 (±14)	-	1164 (±18)	1288 (±32)	1913 (±131)
	5 μm	837 (±41)	960 (±14)	992 (±33)	923 (±14)	1170 (±11)	1441 (±15)	1936 (±116)
	2 μm	-	-	-	970 (±35)	-	-	-
τ_{CRSS} (MPa)	10 μm	-	387 (±11)	433 (±9)	404 (±8)	554 (±14)	561 (±19)	675 (±42)
	8 μm	424 (±7)	412 (±28)	445 (±6)		570 (±9)	568 (±14)	691 (±47)
	5 μm	385 (±19)	442 (±34)	456 (±15)	420 (±6)	573 (±5)	635 (±7)	699 (±42)
	2 μm				441 (±16)			

5.2 Calculation of α/β Interface Strengthening

According to the above literature review in section 2.4.3, the total strength of dual-phase Ti-6Al-4V micropillars is contributed by the strength of α and β phase, as well as the strengthening mechanism of interfaces. Volume fraction of α and β phase, together with the number of β fillets, are taken into consideration. Thus, the total strength can be expressed as Equation 6-1. As for the quantitative calculation of interface strengthening, four components are involved, which are shown in Equation 6-2. However, the chemical interaction caused by the stacking fault mismatch is not considered, because it is difficult to identify the accurate value of stacking fault energy.

$$\tau_{total} = \tau_{\alpha} V_{\alpha} + \tau_{\beta} V_{\beta} + m\tau_{int} \qquad (6\text{-}1)$$

$$\tau_{int} = \tau_{misfit} + \tau_{k} + \tau_{f} + \tau_{w} \quad (6\text{-}2)$$

Where τ_{α} and τ_{β} refer to the CRSS of pure α and β phase, V_{α} and V_{β} refer to the phase volume fraction, m is the efficient number of interfaces, τ_{int} is the strength of interfaces; τ_{misfit} is determined by lattice parameter mismatch; τ_{k} is the Koehler stress caused by shear modulus mismatch; τ_{f} is the interface stress related to the interface energy and interface strain tensor; and τ_{w} is *w* interaction based on the changes of slip systems for one phase to another.

For each component contributing to interface strengthening, more details are shown as follows:

$$\tau_{misfit} = 0.3\overline{G}\sqrt{\frac{2b(\delta-\varepsilon)}{\lambda}} \qquad (2\text{-}10)$$

Where $\overline{G}$ is the average shear modulus, b is the Burgers vector magnitude, δ is the misfit of lattice parameters, ε = 0.76 δ is the residual elastic strain of major heterointerfaces[98], and λ is the layer thickness.

$$\tau_k = \frac{G_A(G_B - G_A)}{4\pi(G_B + G_A)} \times \frac{b}{h} \qquad (2\text{-}11)$$

Where G_A and G_B are the shear moduli of two phases, b is the Burgers vector magnitude, and h is the distance between the interfaces and dislocations, whose minimum distance is estimated to be 10b.

$$\tau_f = f/h \qquad (2\text{-}13)$$

Where f is the interface energy, and h is the interface strain.

$$\tau_w = \tau_A - \tau_B \qquad (2\text{-}14)$$

τ_A and τ_B refer to the Peierls stress on the slips in two phases. The Peierls stress is,

$$\tau = \frac{2\mu}{1-v}\exp[-\frac{2\pi d}{b(1-v)}] \qquad (2\text{-}3)$$

Where σ_p is the critical stress, μ is the shear modulus, d is the interplanar spacing, v is the Poisson's ratio, and b is the Burgers vector magnitude.

All parameters required for calculating the interface strengthening are summarized in Table 5.2.1, involving shear modulus for different phases and slip planes, Poisson's ratio for different phases, Burgers vector magnitude for different phases, the misfit of lattice parameters, the residual elastic strain, layer thickness, interface energy, CRSS for different slip systems, and interplanar spacing for different planes. In addition, Table 5.2.2 shows a summary of calculation results of different slip systems, different β phase volume fractions, as well as different numbers of β fillets. Some parameters in Table 5.2.2 are referred from

literatures[96, 97, 101, 116-123], such as shear modulus, Poisson's ratio, Burger's vector magnitude, CRSS values for different phases and slip systems.

For the prismatic <a_3> slip, the α/β interface strength is 46 MPa through calculation, close to the 49 MPa estimated from experimental results. The experimental CRSS values for micropillars with a size of 5μm in experiments are 442 MPa and 456 MPa, respectively corresponding to micropillars with 1 and 2 β fillets. Meanwhile, when taking β phase volume fraction into consideration, the calculated values are 430 MPa and 469 MPa correspondingly. There is no big difference between the results of experiments and calculations, which means that the theoretical calculation matches the experiments well.

Similarly, for the prismatic <a_2> slip, the α/β interface strength is 18 MPa through the calculation, almost the same as the 20 MPa estimated from experimental results. Interface strengthening for prismatic <a_2> slip is lower than the value of prismatic <a_3> slip, since there is no corresponding slip in β phase for prismatic <a_3> dislocations but to cross slip onto {112} plane in β phase. Whereas the corresponding slip system in β phase for prismatic <a_2> slip in α phase is {110}. It is easier for interfaces to be transferred from <a_2> dislocations, resulting in weaker *w* interactions with a smaller value of τ_w and τ_{int}. The CRSS value of 5μm-sized micropillars with 2 β fillets in experiments is 420 MPa, which is close to the estimated value of 415 MPa. Again, it demonstrates that there is an agreement between the calculations and the experiments.

For the pyramidal <a_3> slip, the α/β interface strengthening and CRSS value are 13 MPa and 485 MPa through the calculation. Compared to the CRSS values in experiments ranging from 554 MPa to 573 MPa for different sized pillars, the calculated value is smaller, which means that the α/β interface strengthening of 13 MPa is underestimated. The reason needs to be further studied.

For the basal <a_1> slip, the α/β interface strengthening and CRSS value are 25 MPa and 576 MPa through the calculation, during which the size effect is not considered. Compared to the CRSS values in experiments ranging from 561 MPa to 635 MPa for pillars of different sizes, the calculated value is located in this range, which has an agreement with experiments.

Moreover, for the basal <a_3> slip, the calculated α/β interface strengthening and CRSS value are estimated to be 32 MPa and 657 MPa. The CRSS values obtained from experiments range from 675 MPa to 699 MPa for pillars of different sizes, which are close to the calculated value. Apparently, the α/β interface strength and CRSS value of basal <a_3> slips are larger than those of basal <a_1> slip, possibly because the basal <a_3> slip in α phase have no corresponding slip in β phase compared to <a_1> slip.

Obviously, <a_3> slip has a higher interface resistance than <a_1> slip. Also, the number of interfaces or β fillets has a strong effect on the CRSS values of micropillars, meanwhile more interfaces or β fillets lead to a higher CRSS.

Table 5.2.1. Summary of parameters for interface strengthening calculation, including Young's modulus and shear modulus for different phases and slip planes, Poisson's ratio, Burgers vector magnitude, the misfit of lattice parameters, the residual elastic strain, layer thickness, interface energy, CRSS for different slip systems, and interplanar spacing for different planes. Parameters are referred from the following literatures[96, 97, 101, 116-123].

	phase	Slip plane	value		phase	Slip plane	value
Young's modulus E/GPa	α+β		129	Shear modulus G/GPa	α+β		49
	α	$(1\bar{1}00)$	121		α	$(1\bar{1}00)$	46
		(0001)	142			(0001)	54
		$(\bar{1}\bar{1}20)$	121			$(\bar{1}\bar{1}20)$	46
		$(1\bar{1}01)$	130			$(1\bar{1}01)$	49
		$(\bar{1}\bar{1}21)$	127			$(\bar{1}\bar{1}21)$	48
	β		81		β		31
Poisson's ratio	α+β		0.33	Burger vector magnitude b/nm	$[\bar{1}\bar{1}20]$ a type in α		0.295
	α		0.32		[111] in β		0.284

	β	0.33	Interface energy f/(J/m^2)			-1
the misfit of lattice parameter δ		0.06	Interface strain h/nm			4-12
ε the residual elastic strain ε		0.76 δ				
layer thickness λ/nm		~500				
interplanar spacing d/nm	α	$(1\bar{1}00)$	0.255	CRSS/MPa	α	Prismatic <a> 385
		(0001)	0.468			
		$(10\bar{1}1)$	0.224			Basal <a> 353
	β	(110)	0.235			Pyramidal <a> 404
		(112)	0.192		β	302

Table 5.2.2. Summary of interface strength and the total strength of micropillars. Slip systems, the amount of β fillets, volume fraction of β phase, τ_{misfit} lattice parameter mismatch, τ_k Koehler stress caused by shear modulus mismatch, τ_f interface stress, and τ_w w interaction are taken into consideration.

Slip system	No. of β fillets	β phase volume fraction	τ_{misfit} (MPa)	τ_k (MPa)	τ_f (MPa)	τ_w (MPa)	τ_{int} (MPa)	τ_{total} (MPa)
Prismatic <a_3>	0	0	0	0	0	0	0	385
Prismatic <a_3>	1	1.56%	47	48	-167	118	46	430
Prismatic <a_3>	2	9.46%	47	48	-167	118	46	469
Prismatic <a_2>	2	6.89%	47	48	-83	5	18	415
Pyramidal <a_3>	10	47.79%	49	56	-182	90	13	485
Basal <a_1>	10	38.48%	52	67	-133	39	25	576
Basal <a_3>	10	34.39%	52	67	-250	163	32	657

5.3 The Comparison of Theoretical Calculation and Experimental Results

Based on the calculation results summarized in Table 5.2.2, the comparison of interface strengthening between experimental and theoretical calculated values for different slip systems are listed in Table 5.3.1. Results are based on the deformed 5μm sized pillars. Experimentally, the values of strengthening for each interface are 49 MPa, 20 MPa, 21 MPa, 31 MPa, and 36 MPa for prismatic $<a_3>$, prismatic $<a_2>$, pyramidal $<a_3>$, basal $<a_1>$, and basal $<a_3>$ slips, respectively. For the theoretically calculated values, they are 46 MPa, 18 MPa, 13 MPa, 25 MPa, and 32 MPa, correspondingly. Experimental values generally have an agreement with theoretical calculations. Typically, the differences of interface strengthening between experiments and calculations for prismatic $<a_3>$, prismatic $<a_2>$, and basal $<a_3>$ slips are only 3 MPa, 2 MPa and 4 MPa.

Furthermore, the experimental and calculated CRSS values for different slips are listed in Table 5.3.2. Experimental CRSS values for prismatic $<a_3>$ (1 β), prismatic $<a_3>$ (2 β), prismatic $<a_2>$, pyramidal $<a_3>$, basal $<a_1>$, and basal $<a_3>$ slips are 442 (±34) MPa, 456 (±15) MPa, 420 (±6) MPa, 573 (±5) MPa, 635 (±7) MPa, and 699 (±42) MPa. Correspondingly, calculated values are 430 MPa, 469 MPa, 415 MPa, 485 MPa, 576 MPa, and 657 MPa. Similarly, there are only limited differences between experimental and calculated CRSS values for prismatic $<a_3>$ (1 β), prismatic $<a_3>$ (2 β), prismatic $<a_2>$, and basal $<a_3>$ slips.

In summary, theoretical calculations match well with experimental results.

Table 5.3.1. The comparison of interface strength between experimental and theoretical calculated values based on CRSS values of deformed 5μm sized pillars.

Slip system	Prismatic <a_3>	Prismatic <a_2>	Pyramidal <a_3>	Basal <a_1>	Basal <a_3>
Experimental (MPa)	49	20	21	31	36
Calculated (MPa)	46	18	13	25	32

Table 5.3.2. The comparison of CRSS values from experiments and theoretical calculation based on deformed 5μm sized pillars.

No. of β fillets	1	2	2	10	10	10
Slip system	Prismatic <a_3>	Prismatic <a_3>	Prismatic <a_2>	Pyramidal <a_3>	Basal <a_1>	Basal <a_3>
Experimental (MPa)	442 (±34)	456 (±15)	420 (±6)	573 (±5)	635 (±7)	699 (±42)
Calculated (MPa)	430	469	415	485	576	657

5.4 The Effect of the Number of α/β Interfaces on Shear Bands

As is shown in the Chapter 5, the number of α/β interfaces has an effect on the shear bands, in terms of nucleation, formation and distribution. As is shown in Fig. 4.4.4, micropillars with the same size of 8μm and along the same loading direction of [18 $\bar{8}$ $\overline{10}$ 1] for prismatic <a_3> slip are compressed to the same strain of 6%. The same size means that the size effect on shear bands can be ignored; the same loading direction keeps activated slip systems unchangeable; and the same strain provides the same displacement for all micropillars. The only difference among those pillars is the number of β fillets inside, which is the key factor influencing the shear bands.

From Fig. 4.4.4 and Fig. 4.4.9, the dominating slip system is prismatic <a_3>. With the number of β fillets changing from 0 to 2, the quantity of shear bands becomes larger, and their distribution is more homogeneous across the whole pillar. In Fig. 4.4.16, the step size reduces dramatically with an increasing number of β fillets or interfaces. In order to explain it, strain localization is introduced. Firstly, for the micro-compression without β phase in a single α phase, strain is homogeneous before compression. After compression, there are few and limited shear bands forming due to the persistent slip band (PSB) mechanism [71, 72] on which the strain highly concentrates on limited shear bands. After the deformation starts, subsequent deformation must happen in the regions with strain concentration because the stress for a continuous deformation is lower. In this case, it is difficult to nucleate more shear bands. Secondly, when introducing β phase into micropillars, strain inhomogeneity and strain localization exist before compression due to the micro-structural inhomogeneity caused by the β phase in Ti-6Al-4V alloys. Additionally, strain localization caused by the residual stress could be eliminated if the specimen is heat treated to relieve residual stress. However, the strain localization caused by the heterogeneous micro-structure couldn't be eliminated as it is

based on the introduction of β phase. As the strain is localized along interfaces, dislocations accumulate and pile up at interfaces so that dislocation can't easily go through all pillars along limited shear bands. Then a large strain localization via dislocation avalanche leads to shear band formation.[70] Through phase interface refinement, the number of slip bands can largely increase, leading to local strain concentration reduction. Therefore, more shear bands are formed, which are more homogeneous while adding more β fillets or interfaces. Since the total strain or displacement of different pillars is the same, more shear bands lead to smaller step sizes, as is shown in Fig. 4.4.16, which can even be nano-scale. It is apparent that β phase is less sheared in micropillars with more β fillets in Fig. 4.4.17, which is also related to the nucleation and formation of shear bands.

Furthermore, for micro-compression of pillars with 10 β fillets oriented for pyramidal $<a_3>$, basal $<a_1>$ and $<a_3>$ slips, lots of shear bands formed after deformation and homogeneously distributed through the whole pillar. β phase is just slightly sheared in those pillars and no notable step size can be investigated, which strongly indicates that the number of α/β-interfaces can largely influence the nucleation, formation and distribution of shear bands, and the step size as well as morphology of β phase after deformation.

5.5 The Effect of the Number of α/β Interfaces on Prismatic $<a_3>$ slip CRSS

After a micropillar compression for the prismatic $<a_3>$ slip, α/β-interfaces have a significant effect on CRSS, as shown in Fig. 5.5.1, which can strengthen micropillars by introducing β phase.

For 10μm-sized micropillars, the CRSS value increases from 387 MPa to 433 MPa by 12%, when the number of β phases changes from 1 to 2. For the compression of micropillars with 8μm in diameter, the CRSS value increases from 412 MPa to 445 MPa by 8%, when increasing the number of β phases from 1 to 2. As for the micro-compression of pillars with 5μm in diameter, the CRSS value increases from 385 MPa to 456 MPa by 18%, when increasing the number of β phases from 0 to 2. Thus, the average increasement from experiments by introducing one β fillet is 49 MPa, which increased by 13% compared to micropillars in a single α phase. 49 MPa is the phase interface strengthening or resistance, which is close to the theoretically estimated value of 46 MPa.

This enhancement is significant as interfaces are regarded as strong barriers for dislocation movement. As is shown in Fig. 4.4.1, the gliding of $<a_3>$ dislocations on prismatic plane is obviously suppressed by the α/β-phase interface. Additionally, dislocations are accumulated and piled up at interfaces, leading to strain and stress concentration. Hence, it can be investigated that prismatic $<a_2>$ slip with a lower Schmid factor is activated due to the stress and strain concentration. CRSS is the stress for dislocations to go through the whole material, so the strong impeding of dislocation gliding by the α/β-interfaces can significantly increase the strength of Ti-6Al-4V micropillars. This increasement should be linear if ignoring the contribution of β phase on CRSS, because the enhancement is only caused by the nature of interfaces themselves, which is only related to lattice parameter mismatch on both sides of interfaces, shear modulus mismatch, interface stress, stacking fault energy difference and *w* interaction based on the changes of slip direction and slip plane from one phase to another.

It should be pointed out that the abnormal phenomenon of size effect on the CRSS values of single α phase micro-pillars, as shown in Fig.5.5.1. It remains unknown to explain this

abnormal phenomenon. Furthermore, more well controlled compression tests would be needed to reassure the results.

In Fig. 5.5.1, the deviations of the mean CRSS values for various size and number of β fillets differ. Most of deviations are acceptable but two of them are too large, which are deviations of CRSS values of 8 μm sized pillars containing 1 β fillet and 10 μm sized pillars containing 2 β fillet. It is possibly because the difference in microstructure inside pillars that affect the mechanical properties. The micro-structural difference is hard to be avoided, but it should be controlled and minimized.

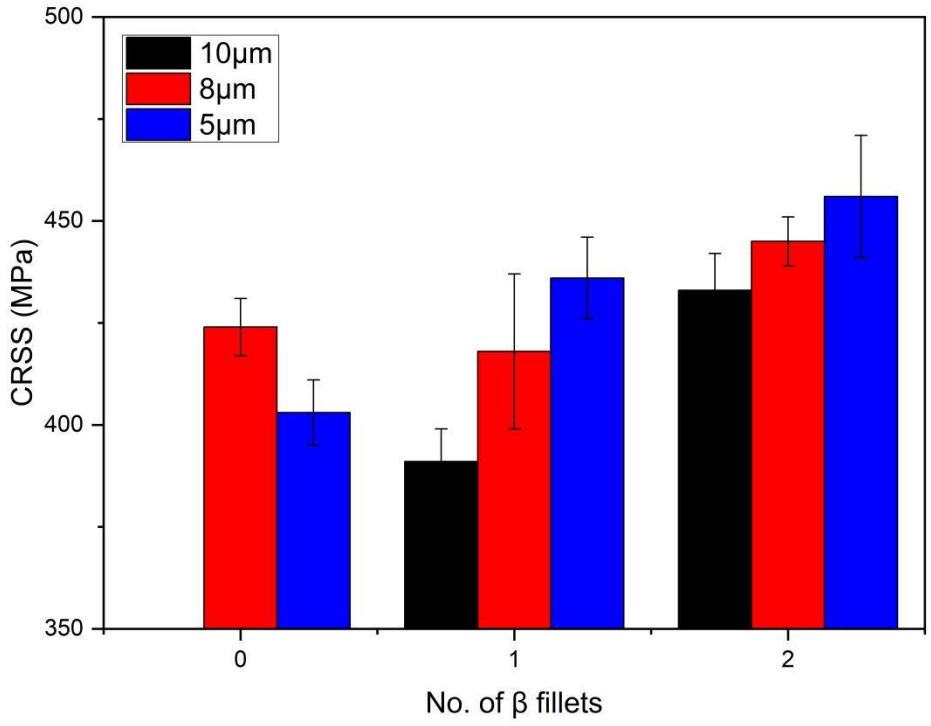

Figure 5.5.1 A comparison of CRSS values for prismatic <a_3> slip with various numbers of β fillets and pillar sizes.

5.6 CRSS of β-containing Micro-pillars Oriented for Prismatic <a_2> and <a_3> Slips

When taking CRSS values of the prismatic <a_2> and prismatic <a_3> slip into comparison, it is apparent that the enhancement of α/β-interfaces in CRSS differs, as shown in Fig. 5.6.1. The α/β-interfaces for the prismatic <a_3> slip have a stronger effect on CRSS than for the prismatic <a_2> slip, when keeping the number of β fillets inside pillars as 2.

In the case of a micro-compression for 10μm-sized pillars, the CRSS value of the prismatic <a_3> slip is 433 MPa, which is 7% higher than that of 404 MPa for the prismatic <a_2> slip. In another case of micro-compression for 5μm-sized pillars, the CRSS value of the prismatic <a_2> and <a_3> slip is respectively 420 MPa and 456 MPa. The CRSS value of prismatic <a_3> slip is 9% higher than that of prismatic <a_2> slip. The experimental interface strengthening for prismatic <a_2> and <a_3> slip is 20 MPa and 49 MPa respectively. Interfaces for prismatic <a_3> slip contribute an extra 29 MPa to CRSS compared with prismatic <a_2> slip.

In Fig. 4.4.5, <a_3> dislocations on prismatic plane in α phase glide through α/β interface and into β phase. <a_3> dislocations segregate to <b_1> and <b_2> dislocations in β phase, as there are no corresponding dislocations. Additionally, dislocations cross slip onto (112) plane rather than (110) plane in β phase[1]. Differently, <a_2> dislocations on prismatic plane in α phase have corresponding <b_2> dislocations in β phase. The angle between <a_2> and <b_2> is as small as about 11°, as is shown in Fig. 4.4.18. Also, prismatic <a_2> slip in α phase has the corresponding plane (110) in β phase. Thus, it is tougher for prismatic <a_3> dislocations to overcome interface barriers from α phase into β phase, compared to prismatic <a_2> dislocations. In the components of interface strengthening τ_{int}, lattice parameter mismatch τ_{misfit} and shear modulus mismatch τ_k have the same contribution, and the main difference is from the *w* interaction τ_w. *w* interaction τ_w is the difference between Peierls stresses of slips

in α phase and β phase. For prismatic <a_2> and prismatic <a_3> slips in α phase, interplanar spacing *d* and Burgers magnitude *b* for both have the same values, leading to the same Peierls stresses of slips. The corresponding slip systems in β phase for prismatic <a_2> and prismatic <a_3> slips are [111] $(1\bar{1}0)$ and [111] $(11\bar{2})$, respectively. Burgers vector magnitudes of these two kinds of slips in β phase are the same, but interplanar spacings differ. The interplanar spacing for {110} is 0.235 nm, higher than that of 0.192 nm for {112} plane. Therefore, Peierls stress for [111] {110} slip is smaller than that for [111] {112} slip. Furthermore, τ_w ($\tau_w = \tau_\beta - \tau_\alpha$) for prismatic <$a_2$> slip is lower than that for prismatic <a_3> slip. So, the α/β interfaces for prismatic <a_3> slip have a stronger effect on CRSS than the prismatic <a_2> slip, by contributing an extra 29 MPa to CRSS values.

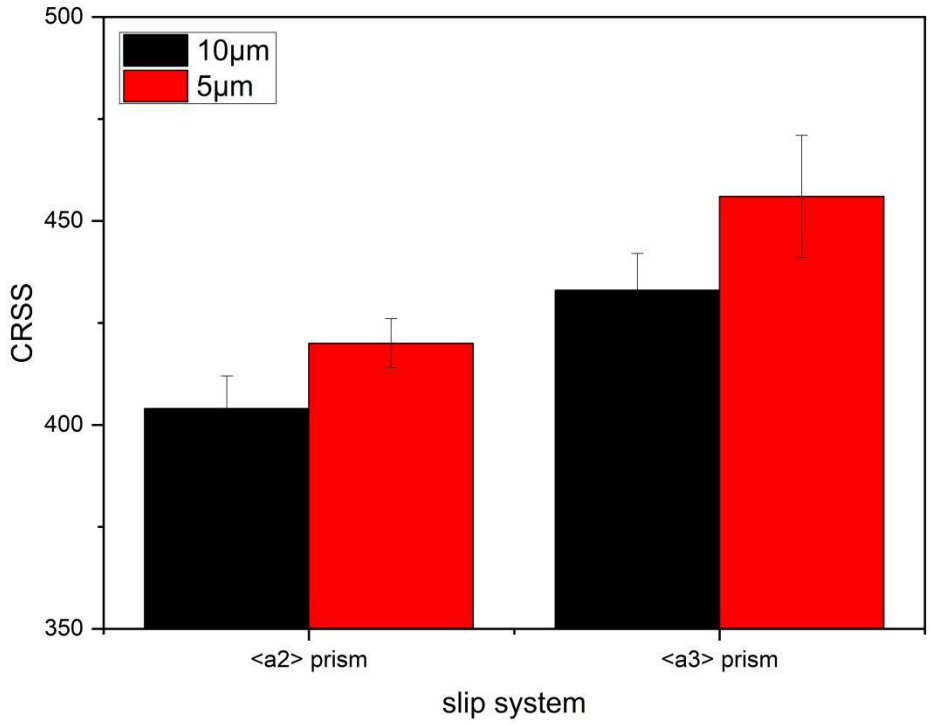

Figure 5.6.1 A comparison of the CRSS value of the compressed pillars with the same number of β fillets, which is 2. For 10μm and 5μm-sized pillars, the CRSS value of prismatic <a_3> slip is higher than that of prismatic <a_2> slip.

5.7 CRSS of β-containing Micro-pillars Oriented for Pyramidal <a_3> Slip, Basal <a_1> and Basal <a_3> slips

Micropillars with about 10 β fillets inside are compressed for pyramidal <a_3>, basal <a_1> and <a_3> slip, whose CRSS values are very high, which is more than 550 MPa, indicating that α/β interfaces with a large amount play an important role in strengthening. Generally, the CRSS values for basal <a_3> slip is the highest, whereas that for pyramidal <a_3> and basal <a_1> slip is slightly lower, as is shown in Fig. 5.7.1.

For pyramidal <a_3> slip, 10μm, 8μm and 5μm-sized micropillars provide CRSS values of 554 MPa, 570 MPa and 573 MPa respectively. For basal <a_1> slip, 10μm, 8μm and 5μm-sized micropillars provide CRSS values of 561 MPa, 568 MPa and 635 MPa respectively. For basal <a_3> slip, 10μm, 8μm and 5μm-sized micropillars provide CRSS values of 675 MPa, 691 MPa and 699 MPa respectively. These CRSS values are much higher than reported values [40] [43, 47] : pyramidal <a> slip has a CRSS of 404 MPa, basal <a> has a CRSS of 353 MPa, without the presence of β phase. It demonstrates that the CRSS value of Ti-6Al-4V significantly increase when introducing a large number of β fillets or α/β interfaces. In micropillars containing 10 β fillets, the β phase volume fractions for pyramidal <a_3>, basal <a_1> and basal <a_3> slips are respectively 47.79%, 38.48% and 34.39%, which can largely lower the CRSS of dual-phase pillars since β phase is softer than α phase. Hence, the effect of α/β interfaces on CRSS is even stronger.

Comparing the CRSS values of basal <a_1> and <a_3> slip from micropillars with 10 β fillets, as is shown in Fig. 5.7.1, the CRSS value of basal <a_3> slip is higher than that of basal <a_1> slip, which is consistent with the trend in literatures: basal <a_3> slip has a higher CRSS value of 366 MPa than basal <a_1> slip with a CRSS of 341 MPa. As is discussed above, because <a_3> slip has no corresponding slip in β phase, whereas <a_1> slip in α phase has a corresponding slip <b_1> in β phase (<a_1> and <b_1> have the same direction), dislocations can transmit interfaces very easily. However, the situation changes when taking pyramidal <a_3> and basal <a_3> slip into comparison. According to literatures[40], [43], [47], pyramidal <a> slip has a higher CRSS of 404 MPa than basal <a_3> slip with a CRSS of 366 MPa. But Fig. 5.7.1 suggests that the CRSS value of pyramidal <a_3> slip is apparently lower than that of basal <a_3> slip in the condition of 10 β fillets in micropillars. This phenomenon is required to be studied further.

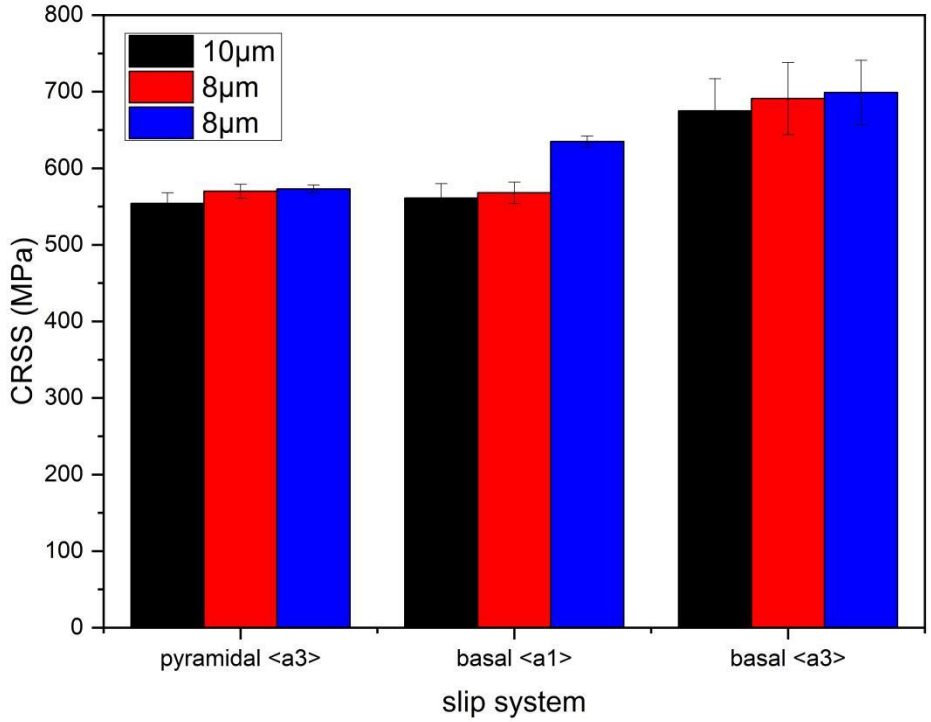

Figure 5.7.1 A comparison of the CRSS value of various slip systems and different pillar sizes with the same number of β fillets, which is 10, from the air-cooled heat-treated samples.

5.8 Pillar Size Effect Dependence on the Number of α/β Interfaces (β Fillets)

It is discussed in this section that the number of α/β interfaces or β fillets has an influence on the sensitivity of pillar size effect on CRSS values. It is found that with the number of α/β interfaces or β fillets increasing in micropillars, the size effect on CRSS becomes less sensitive, as is shown in Fig. 5.8.1.

In order to study the size effect sensitivity, the CRSS values of 10μm and 5μm-sized pillars with various numbers of β fillets are summarized in Table 5.8.1. Then $\Delta\tau_{CRSS}$ and CRSS percentage increments are obtained. For micropillars with only 1 β fillet, the CRSS of prismatic $<a_3>$ slip increases by 14.2%, when reducing the pillar size from 10μm to 5μm. For micropillars with 2 β fillets, the CRSS of prismatic $<a_3>$ slip increases by 5.3%, and that of prismatic $<a_2>$ slip increases by 4.0%, when reducing the pillar size from 10μm to 5μm. Moreover, in pillars containing about 10 β fillets, the CRSS of pyramidal $<a_3>$ and basal $<a_3>$ slip increases by 3.4% and 3.5%, when reducing the pillar size from 10μm to 5μm. In Fig. 5.8.1, it obviously suggests that percentage increment of CRSS drops down with increasing the number of β fillets from 1 to 10, indicating that the size effect on CRSS becomes weaker and less sensitive. Thus, with α/β interfaces or the number of β fillets increasing, α/β interfaces play more significant role on CRSS than size effect.

To explain this phenomenon, extrinsic size effect on CRSS and dislocation source mechanism are discussed. In a micro-scale compression, extrinsic size effect on CRSS is dominated by the single-arm dislocation source truncation[65-68]. The CRSS of micro-compression means the critical stress for first dislocation to go through the whole pillar[124], which is dependent on the initiation of dislocations from the double-pinned Frank-Read source[125]. In the finite dimension of micropillars, double-pinned Frank-Read sources can't form whole dislocation loops, which end up with an interaction with pillar surfaces. Therefore, truncated single-arm dislocations with one end at free surfaces and the other pins are formed, due to the limited dimensions of micropillars. By reducing the micropillar size, the dimensions become more limited, making it more difficult to initiate and bow Frank-Read sources. So, CRSS can be increased. However, when introducing interfaces, dislocations will first interact with interfaces rather than free surfaces to form single-arm dislocation sources.

Hence, by adding more and more interfaces, the interaction between dislocations and interfaces dominates CRSS, and size effect is less sensitive.

Table 5.8.1. A summary of CRSS value increment from 10μm to 5μm-sized pillars nad percentage increment. Results of different slip systems and different numbers of β fillets are involved.

No. of β fillets	1	2	2	10	10
Slip system	$<a_3>$ Prism	$<a_3>$ Prism	$<a_2>$ Prism	$<a_3>$ Pyramidal	$<a_3>$ basal
τ_{CRSS} (MPa) of 10 μm	387	433	404	554	675
τ_{CRSS} (MPa) of 5 μm	442	456	420	573	699
$\Delta\tau_{CRSS}$ (MPa)	55	23	16	19	24
Relative increment	14.2%	5.3%	4.0%	3.4%	3.5%

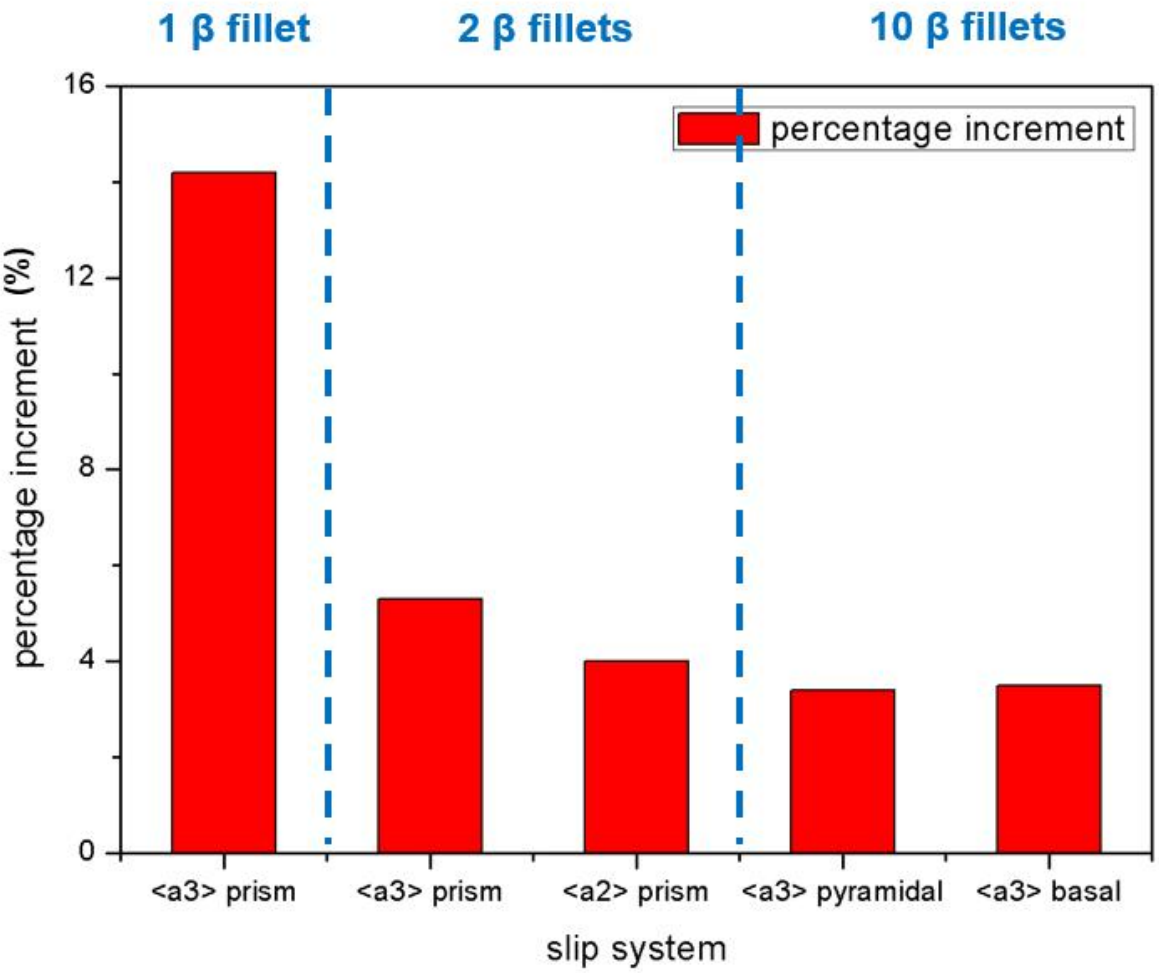

Figure 5.8.1 A comparison of CRSS percentage increment with various β fillets involved in micropillars. The percentage of CRSS increment is obtained by comparing the CRSS value of 10μm and 5μm-sized pillars. With the increase of the number of β fillets, the percentage of increment of CRSS drops dramatically, indicating that size effect becomes weaker.

5.9 Experimental Challenges Encountered

Nowadays, micro-compression test is popular to be applied for the measurement of mechanical properties due to its high precised control of load and displacement. A sharp Berkovich tip is used to measure the hardness and Young's modulus at the nano- or micro-scale in the conventional indentation test. However, in the micro-compression of this project,

a flat ended tip is used to compress the pillar to study the size effects on the mechanical properties[126, 127]. The fabrication of cylinders by using focused ion beam (FIB) is to achieve the micro-scale dimension with ease. There are several factors that can affect the experimental results of micro-compression, such as shape of the pillar, aspect ratio, taper angle, friction, and misalignment.

5.9.1 Shape of the Pillar

Normally, cylindrical or cuboidal posts[128, 129] are used for micro-compression tests. Cuboidal post has the significant issue of concentrated stress on the sharp edges, resulting in ununiform stress and strain distribution. It makes the analysis of mechanical properties more difficult. The advantages of the cuboidal post are the elimination of the taper angle and better investigation of slip traces. Differently, the cylindrical post is obtained by the circular milling method. In this way, sharp edges disappear, and stress and strain distributions become more homogeneous.

5.9.2 Aspect Ratio and Height Measurement

Aspect ratio is another significant geometric factor that has an effect on the accuracy of the micro-compression. Firstly, the c/a ratio of Ti-6Al-4V alloy is 1.59, in order to activate all possible slips, the aspect ratio must be larger than 1.59. Additionally, if the aspect ratio is less than 2, the constraints from the matrix may occur, leading to the strain hardening. It is because the deformation of the matrix always exists, which also leads to the underestimation of the elastic modulus. If the aspect ratio is too large, the buckling should be considered. For

micro-compression tests, the buckling is a common concern. When the aspect ratio is 5, the severe buckling can be observed[130]. As decreasing the aspect ratio to 3, there is a dramatic stress reduction compared to aspect ratio of 2.2. Thus, the aspect ratio in this project is selected as 2[130].

In order to achieve the aspect ratio of 2, the height and diameter of pillars should be accurately measured. The diameter can be measured with ease, but the height is more difficult to be gotten due to the milling method. In Figure 6.8.2, the clear and uniform bottom side can be observed at the tilting angle of 20˚. Firstly, the top and bottom diameters can be easily measured. Then the distance between two parallel diameters is the pillar height, as shown in Figure 6.8.2. Consequently, the expected aspect ratio of 2 was obtained.

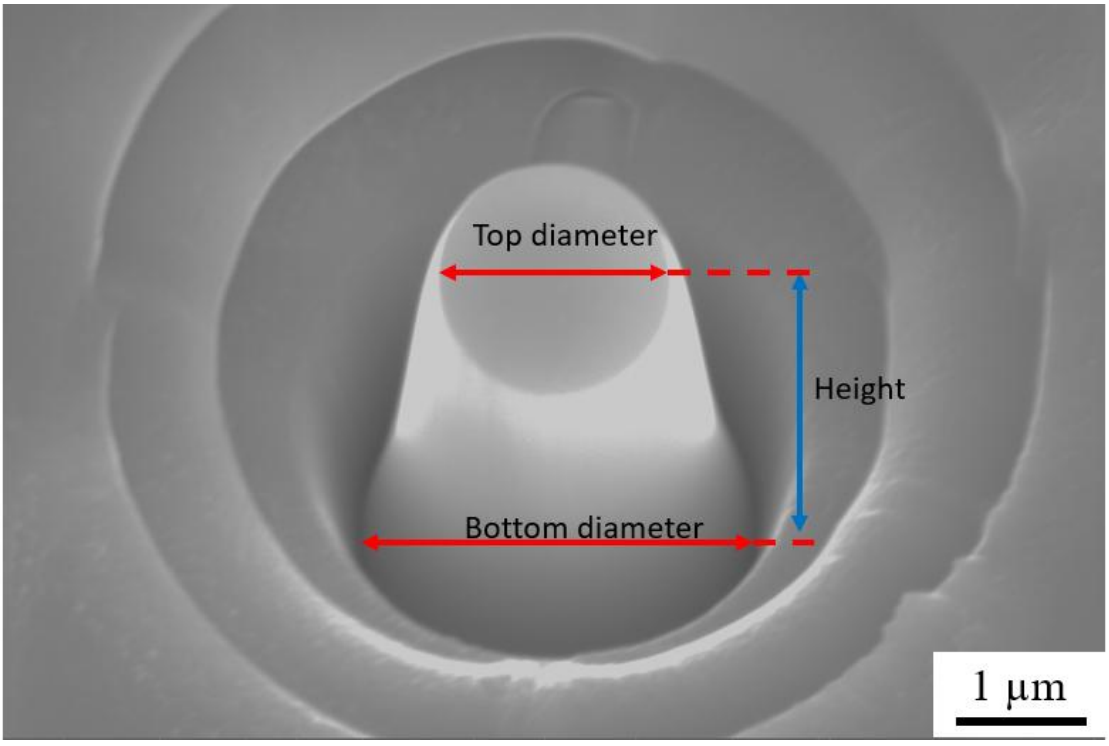

Figure 6.8.2 The accurate measurement of top and bottom diameter as well as height. Top and bottom diameters are indicated by red arrows and the height is refered by the blue arrow.

5.9.3 Taper

Due to the inaccuracies of the current fabrication method of circular milling, the taper angle of micropillars exist. Normally, the top diameter is smaller than the bottom diameter and the taper angle is defined by the pillar axis and the pillar wall. During the deformation, stress mainly concentrates on the top as it has smaller area and slip possibly starts from the top. Furtherly, the taper can produce an artificial work hardening[130] as the flow stress slowly increases after the yield point. Also, the taper can increase the yield point[130]. Thus, the taper has deleterious effects on the deformation, which should be avoided or reduced by optimizing the fabrication method.

5.9.4 Misalignment

The misalignment is defined by the angle θ between micro-pillar top surface and the flat punch surface should be considered, which will significantly affect the accuracy of micro-compression. When the θ is 0, the compression system is perfectly aligned, and the flat tip will fully contact the pillar from the beginning. However, in the practical case, the misalignment always exists which means the angle θ is not 0. Therefore, the tip would contact the pillar from a point and then fully contact gradually. This results in the deviation of the elastic process of the stress-strain curve. Thus, the elastic modulus is underestimated. With the angle θ of the misalignment becomes larger, the underestimation of elastic modulus is more severe[130]. By the way, even if the alignment is perfect, the measured elastic

modulus is still underestimated due to the compliance of the matrix. Aiming to get more reliable data, the misalignment should be reduced as small as possible.

5.9.5 Friction

Usually, the micro-compression tests are performed without lubrication between the flat punch and the pillar top surface. The friction between the flat punch and the pillar top surface tends to restrict the plasticity hence leading to the stress concentration. This is consistent with the fact that the top of the pillar tends to be heavily deformed after the compression. Zhang and co-authors [130] found that with the friction can suppress the buckling when the aspect ratio is larger than 2. However, the aspect ratio in this project is not larger than 2. Thus, the effect of friction during the compression tests.

5.9.6 Pre-stress

As the initial part from the stress-strain curves of micro-compression is non-linear mainly due to the misalignment of flat punch and pillar top surface. This often makes slope of the stress-strain curve significantly deviated from the otherwise elastic behaviour expected. This could be solved by applying a small pre-stress to the pillar top surface to keep both the flat punch and pillar top surface fully in contacted. Such small stress is sufficient to locally deform the pillar (i.e. being flattened) but the majority of the pillar would be left untouched. In this project, the micro-compressions were not carried out under the pre-stress, resulting the deviation of stress-strain curves. This should be avoided in the future.

5.9.7 Summary for Micro-compression

In a summary, for the improvement of micro-compression and potential application for the modelers, some suggestions can be raised here:

cylindrical post is better than cuboidal posts since the stress and strain are more uniform during the deformation, the pillar height should be measured accurately to achieve the aspect ratio of 2, the taper should be avoided to reduce the artificial work hardening, the misalignment should be reduced to decrease the deviation of elastic process, and occurring friction is necessary to get rid of the buckling. Since several factors can affect the elastic modulus during the loading process, the elastic modulus was derived from the unloading part of the graph.

5.9.8 Comparison among Micro-tension, Micro-compression and Micro-bending

Besides the micro-compression tests for the investigation of deformation mechanisms, there are other methods, such as tension and bending tests, can be carried out to study deformation mechanisms.

Micro-tension[131], micro-compression[132] and micro-bending[12] tests have been used to study the mechanical properties at small scales and each has difference challenges associated.

Micro-tension test can be used to study the ductility of materials. For tension test, the strain could be large enough to fracture. The specimen geometries for micro-tension normally include central hole, notched or dogbone-shapes[133, 134]. Micro-tension test samples are more difficult to prepare and it is critical (and also challenging) to maintain the sample/grip alignment during the tensile test.

Micro-compression is much simpler in sample preparation and hence has been widely used to evaluate the strength (e.g. yield stress) of materials. Observation of the slip trace is also relative straightforward. However precautions must be undertaken to mitigate the challenges associated with compression tests such as the tapering angle of the sample prepared and the alignment of the small samples with regards to the loading axis.

The micro-bending test is another method where samples can be readily prepared. However, the resultant load-deflection data often needs to be used together with computer modelling in order to derive the parameters useful, e.g. yield stress.

Chapter 6 Conclusions and Future Work

6.1 Conclusions

The main conclusions from the current study are:

i. The α/β interface in Ti-6Al-4V alloy has a significant strengthening effect on the CRSS measured, viz. 49 MPa, 20 MPa, 21 MPa, 31 MPa, and 36 MPa, for prismatic $<a_3>$, prismatic $<a_2>$, pyramidal $<a_3>$, basal $<a_1>$ and basal $<a_3>$ slips, respectively, which are close to the values of 46 MPa, 18 MPa, 13 MPa, 25 MPa, and 32 MPa estimated theoretically. In other words, the interface strengthening is slip system dependent. Moreover, the measured strengthening effect of α/β interfaces increases with the number of α/β interfaces in micropillars.

ii. The α/β interfaces in Ti-6Al-4V can impede dislocation slip, resulting in stress and strain localization, increasing the CRSS.

iii. Shear band nucleation, formation, and distribution are influenced by the number of α/β interfaces in the micro-pillars. The distribution of slip traces becomes more homogeneous, with reduced slip step size.

iv. For pillars oriented for prismatic $<a_3>$ slip, the CRSS increases by 18% when the number of β fillets increased from 0 to 2. The average α/β interface strengthening is measured to be 49 MPa, almost the same as the calculated value of 46 MPa. Stress and strain localization at the interfaces may have resulted in the second set of prismatic $<a_2>$ slip in the same pillars.

v. In the micro-pillars containing two same β fillets, the CRSS for prismatic $<a_3>$ slip is 7-9% higher than that for prismatic $<a_2>$ slip. Experimentally, the interface strengthening to the CRSS amounts to 49 MPa for prismatic $<a_3>$ slip contributes,

higher than that of 20 MPa for prismatic <a_2> slip, due to the specific crystallography relationship anisotropy of the alloy. In contrast the theoretical estimation suggests that interface strengthening on prismatic <a_3> slip is 46 MPa while18 MPa on prismatic <a_2> slip.

vi. The CRSS values measured from the micro-pillars containing 10 β fillets are 573 MPa, 635 MPa and 699 MPa for pyramidal <a_3>, basal <a_1> and <a_3> slips, much higher than the reported values of 404 MPa for pyramidal <a> slip, and 353 MPa for basal <a> slip without the presence of α/β interface, respectively.

vii. The pillar size effect on the measured CRSS reduces with the increasing number of α/β interfaces contained in the micro-pillars.

6.2 Future Work

According to the present work in this project, several suggestions for future works are come up with as follows:

i. Chemical interaction τ_{ch}, by the stacking fault mismatch from chemical difference, also contributes to the interface strength. However, in this project, it is not considered since it cannot be easily obtained. So, it is of interest to further study the chemical interaction of different slips.

ii. From the results presented, stress-strain curves with 10 β fillets have a remarkably high strain hardening rate, whereas those with 1 or 2 β fillets have no obvious strain hardening. This is required to be further studied by understanding how the interaction between dislocations and interfaces contributes to strain hardening.

iii. For the micro-compression of pillars with 10 β fillets, the CRSS of basal <a_3> slip is higher than the value of pyramidal <a_3> slip, which is inverse to the literatures. The

reason needs to be found. Possibly, it is caused by the large number of interfaces introduced into micropillars.

iv. More micro-compressions for prismatic <a_3> slip with more β fillets, such as 3-10, can be done to enrich the theories related to the effect of interfaces on micro-compression behaviour. Similarly, it is also valuable to carry out micro-compressions for basal <a_1> and <a_3> slip with fewer β fillets.

Appendix: Publications

1. M. K. Dash, L. Shi, **Z. Wu**, Y. Chiu. Stress field analysis near a grain boundary of a Ni-base superalloy during the micropillar compression. Modern Practice in Stress and Vibration Analysis (MPSVA 2022), 12-14th July 2022, St Anne's College, Oxford.

2. Y. Lu, M. Wang, **Z. Wu**, I. P. Jones, M. Wickins, N. R. Green, H. C. Basoalto. Three-dimensional analysis of dendrites via automated serial sectioning using a Robo-Met. 3D. MRS Communications (2020), 10, 461–466

3. M. K. Dash, L. Shi, **Z. Wu**, Y. Chiu. Role of grain boundary on the deformation of micropillars. Nanomechanical Testing in Materials Research and Development VIII An ECI Conference Series, 2-7th October 2022, Le Méridien Lav Split, Split, Croatia

References

[1] M. Savage, J. Tatalovich, M. Mills, Anisotropy in the room-temperature deformation of α–β colonies in titanium alloys: role of the α–β interface, Philosophical Magazine 84(11) (2004) 1127-1154.

[2] H. Gao, Y. Huang, Geometrically necessary dislocation and size-dependent plasticity, Scripta Materialia 48(2) (2003) 113-118.

[3] W. Burgers, On the process of transition of the cubic-body-centered modification into the hexagonal-close-packed modification of zirconium, Physica 1(7-12) (1934) 561-586.

[4] T. Ahmed, H. Rack, Phase transformations during cooling in α+ β titanium alloys, Materials Science and Engineering: A 243(1-2) (1998) 206-211.

[5] S. Banerjee, P. Mukhopadhyay, Phase transformations: examples from titanium and zirconium alloys, Elsevier2010.

[6] F. Dunne, D. Rugg, On the mechanisms of fatigue facet nucleation in titanium alloys, Fatigue & Fracture of Engineering Materials & Structures 31(11) (2008) 949-958.

[7] G. Sun, C. Wang, X. Wei, D. Shang, S. Chen, Study on small fatigue crack initiation and growth for friction stir welded joints, Materials Science and Engineering: A 739 (2019) 71-85.

[8] J. Newman, X. Wu, M. Swain, W. Zhao, E. Phillips, C. Ding, Small-crack growth and fatigue life predictions for high-strength aluminium alloys. Part II: crack closure and fatigue analyses, Fatigue & fracture of engineering materials & structures (Print) 23(1) (2000) 59-72.

[9] X. Zhang, J.-C. Stinville, T.M. Pollock, F.P. Dunne, Crystallography and elastic anisotropy in fatigue crack nucleation at nickel alloy twin boundaries, Journal of the Mechanics and Physics of Solids 155 (2021) 104538.

[10] J.Z. Zhang, J.Z. Zhang, Z.X. Meng, Direct high resolution in situ SEM observations of very small fatigue crack growth in the ultra-fine grain aluminium alloy IN 9052, Scripta Materialia 50(6) (2004) 825-828.

[11] J. Gong, A.J. Wilkinson, A microcantilever investigation of size effect, solid-solution strengthening

and second-phase strengthening for< a> prism slip in alpha-Ti, Acta Materialia 59(15) (2011) 5970-5981.

[12] J. Gong, A.J. Wilkinson, Anisotropy in the plastic flow properties of single-crystal α titanium determined from micro-cantilever beams, Acta Materialia 57(19) (2009) 5693-5705.

[13] J. Williams, R. Baggerly, N. Paton, Deformation behavior of HCP Ti-Al alloy single crystals, Metallurgical and Materials Transactions A 33(3) (2002) 837-850.

[14] J. Qiu, Y. Ma, J. Lei, Y. Liu, A. Huang, D. Rugg, R. Yang, A comparative study on dwell fatigue of Ti-6Al-2Sn-4Zr-xMo (x= 2 to 6) alloys on a microstructure-normalized basis, Metallurgical and Materials Transactions A 45(13) (2014) 6075-6087.

[15] K. Chan, C. Wojcik, D. Koss, Deformation of an alloy with a lamellar microstructure: experimental behavior of individual widmanstatten colonies of an α-β titanium alloy, Metallurgical Transactions A 12(11) (1981) 1899-1907.

[16] S. Suri, G. Viswanathan, T. Neeraj, D.-H. Hou, M. Mills, Room temperature deformation and mechanisms of slip transmission in oriented single-colony crystals of an α/β titanium alloy, Acta Materialia 47(3) (1999) 1019-1034.

[17] T.-S. Jun, G. Sernicola, F.P. Dunne, T.B. Britton, Local deformation mechanisms of two-phase Ti alloy, Materials Science and Engineering: A 649 (2016) 39-47.

[18] P.J. Ashton, T.-S. Jun, Z. Zhang, T.B. Britton, A.M. Harte, S.B. Leen, F.P. Dunne, The effect of the beta phase on the micromechanical response of dual-phase titanium alloys, International Journal of Fatigue 100 (2017) 377-387.

[19] V.A. Joshi, Titanium alloys: an atlas of structures and fracture features, Crc Press2006.

[20] G. Welsch, R. Boyer, E. Collings, Materials properties handbook: titanium alloys, ASM international1993.

[21] X. Liu, P.K. Chu, C. Ding, Surface modification of titanium, titanium alloys, and related materials for biomedical applications, Materials Science and Engineering: R: Reports 47(3-4) (2004) 49-121.

[22] K.-T. Rie, T. Lampe, Thermochemical surface treatment of titanium and titanium alloy Ti 6Al 4V

by low energy nitrogen ion bombardment, Materials Science and Engineering 69(2) (1985) 473-481.

[23] J. Albrecht, G. Lütjering, Microstructure and mechanical properties of titanium alloys, Titanium'99: Science and Technology (2000) 363-374.

[24] M.-S. Yeh, J.-H. Huang, Hydrogen-induced subcritical crack growth in Ti–6Al–4V alloy, Materials Science and Engineering: A 242(1-2) (1998) 96-107.

[25] J. Peters, R. Ritchie, Foreign-object damage and high-cycle fatigue of Ti–6Al–4V, Materials Science and Engineering: A 319 (2001) 597-601.

[26] M.J. Donachie, Titanium and Titanium alloys: source book: a collection of outstanding articles from the technical literature, ASM international1982.

[27] X. Lu, In-situ transmission electron microscopy study of dislocation in TI-6AL-4V, University of Birmingham, 2017.

[28] S. Kampe, P. Sadler, L. Christodoulou, D. Larsen, Room-Temperature strength and deformation of Tib 2-reinforced near-γ titanium aluminides, Metallurgical and Materials Transactions A 25(10) (1994) 2181-2197.

[29] G. Lütjering, J.C. Williams, Special Properties and Applications of Titanium, Titanium (2007) 383-415.

[30] J. Mayeur, D. McDowell, A three-dimensional crystal plasticity model for duplex Ti–6Al–4V, International journal of plasticity 23(9) (2007) 1457-1485.

[31] T. Sakai, M. Fine, Plastic deformation of Ti-Al single crystals in prismatic slip, Acta Metallurgica 22(11) (1974) 1359-1372.

[32] F. Bridier, P. Villechaise, J. Mendez, Analysis of the different slip systems activated by tension in a α/β titanium alloy in relation with local crystallographic orientation, Acta Materialia 53(3) (2005) 555-567.

[33] A.C. Lewis, S.M. Qidwai, A.B. Geltmacher, Slip systems and initiation of plasticity in a body-centered-cubic titanium alloy, Metallurgical and materials transactions A 41(10) (2010) 2522-2531.

[34] P. Kwaśniak, P. Śpiewak, H. Garbacz, K.J. Kurzydłowski, Plasticity of hexagonal systems: Split slip modes and inverse Peierls relation in α-Ti, Physical Review B 89(14) (2014) 144105.

[35] M. MUZVIDZIWA, Fatigue Resistance Relevant to Locally Developed Microstructures in Friction Stir Welded Light Metal Joints, (2016).

[36] G. Lütjering, J.C. Williams, Titanium, Springer Science & Business Media2007.

[37] G. Singh, I. Sen, K. Gopinath, U. Ramamurty, Influence of minor addition of boron on tensile and fatigue properties of wrought Ti–6Al–4V alloy, Materials Science and Engineering: A 540 (2012) 142-151.

[38] A. Salem, S. Semiatin, Anisotropy of the hot plastic deformation of Ti–6Al–4V single-colony samples, Materials Science and Engineering: A 508(1-2) (2009) 114-120.

[39] M. Savage, J. Tatalovich, M. Zupan, K. Hemker, M. Mills, Deformation mechanisms and microtensile behavior of single colony Ti–6242Si, Materials Science and Engineering: A 319 (2001) 398-403.

[40] J.R. Mayeur, Three dimensional modeling of Ti-Al alloys with application to attachment fatigue, Georgia Institute of Technology, 2004.

[41] N. Paton, The deformation of α-phase titanium, Titanium science and technology (1973).

[42] J.M. Perilla, J.G. Sevillano, Two-dimensional sections of the yield locus of a Ti 6% Al 4% V alloy with a strong transverse-type crystallographic α-texture, Materials Science and Engineering: A 201(1-2) (1995) 103-110.

[43] D. Dunst, H. Mecking, Analysis of experimental and theoretical rolling textures of two-phase titanium alloys, Zeitschrift fur Metallkunde 87(6) (1996) 498-507.

[44] J. Fundenberger, M. Philippe, F. Wagner, C. Esling, Modelling and prediction of mechanical properties for materials with hexagonal symmetry (zinc, titanium and zirconium alloys), Acta materialia 45(10) (1997) 4041-4055.

[45] R. Lebensohn, G. Canova, A self-consistent approach for modelling texture development of two-phase polycrystals: application to titanium alloys, Acta Materialia 45(9) (1997) 3687-3694.

[46] S. Semiatin, T. Bieler, Effect of texture changes on flow softening during hot working of Ti-6Al-4V, Metallurgical and Materials Transactions A 32(7) (2001) 1871-1875.

[47] P.G. Partridge, The crystallography and deformation modes of hexagonal close-packed metals,

Metallurgical reviews 12(1) (1967) 169-194.

[48] J.P. Hirth, J. Lothe, T. Mura, Theory of dislocations, Journal of Applied Mechanics 50(2) (1983) 476.

[49] P.M. Anderson, J.P. Hirth, J. Lothe, Theory of dislocations, Cambridge University Press2017.

[50] E. Clouet, Ab initio models of dislocations, Handbook of Materials Modeling: Methods: Theory and Modeling (2020) 1503-1524.

[51] Z.P. Bažant, Size effect, International Journal of Solids and Structures 37(1-2) (2000) 69-80.

[52] Z.P. Bažant, Size effect on structural strength: a review, Archive of applied Mechanics 69(9) (1999) 703-725.

[53] E. Hall, The deformation and ageing of mild steel: III discussion of results, Proceedings of the Physical Society. Section B 64(9) (1951) 747.

[54] N. Petch, The cleavage strength of polycrystals, Journal of the Iron and Steel Institute 174 (1953) 25-28.

[55] P. Derlet, R. Maaß, Universal power-law strengthening in metals?, Scripta Materialia 109 (2015) 19-22.

[56] N. Hansen, Hall–Petch relation and boundary strengthening, Scripta Materialia 51(8) (2004) 801-806.

[57] J.R. Greer, J.T.M. De Hosson, Plasticity in small-sized metallic systems: Intrinsic versus extrinsic size effect, Progress in Materials Science 56(6) (2011) 654-724.

[58] H. Van Swygenhoven, P. Derlet, Grain-boundary sliding in nanocrystalline fcc metals, Physical review B 64(22) (2001) 224105.

[59] J. Gong, A.J. Wilkinson, Sample size effects on grain boundary sliding, Scripta Materialia 114 (2016) 17-20.

[60] W.D. Nix, H. Gao, Indentation size effects in crystalline materials: a law for strain gradient plasticity, Journal of the Mechanics and Physics of Solids 46(3) (1998) 411-425.

[61] E. Demir, D. Raabe, F. Roters, The mechanical size effect as a mean-field breakdown phenomenon: Example of microscale single crystal beam bending, Acta Materialia 58(5) (2010) 1876-1886.

[62] Y. Huang, F. Zhang, K. Hwang, W. Nix, G. Pharr, G. Feng, A model of size effects in nano-indentation, Journal of the Mechanics and Physics of Solids 54(8) (2006) 1668-1686.

[63] J.R. Greer, W.D. Nix, Nanoscale gold pillars strengthened through dislocation starvation, Physical Review B 73(24) (2006) 245410.

[64] W.D. Nix, J.R. Greer, G. Feng, E.T. Lilleodden, Deformation at the nanometer and micrometer length scales: Effects of strain gradients and dislocation starvation, Thin Solid Films 515(6) (2007) 3152-3157.

[65] T.A. Parthasarathy, S.I. Rao, D.M. Dimiduk, M.D. Uchic, D.R. Trinkle, Contribution to size effect of yield strength from the stochastics of dislocation source lengths in finite samples, Scripta Materialia 56(4) (2007) 313-316.

[66] S.I. Rao, D. Dimiduk, T.A. Parthasarathy, M. Uchic, M. Tang, C. Woodward, Athermal mechanisms of size-dependent crystal flow gleaned from three-dimensional discrete dislocation simulations, Acta Materialia 56(13) (2008) 3245-3259.

[67] S.-W. Lee, W.D. Nix, Size dependence of the yield strength of fcc and bcc metallic micropillars with diameters of a few micrometers, Philosophical Magazine 92(10) (2012) 1238-1260.

[68] D. Kiener, A. Minor, Source truncation and exhaustion: insights from quantitative in situ TEM tensile testing, Nano letters 11(9) (2011) 3816-3820.

[69] Z.-J. Wang, Q.-J. Li, Z.-W. Shan, J. Li, J. Sun, E. Ma, Sample size effects on the large strain bursts in submicron aluminum pillars, Applied Physics Letters 100(7) (2012) 071906.

[70] S.D. Antolovich, R.W. Armstrong, Plastic strain localization in metals: origins and consequences, Progress in Materials Science 59 (2014) 1-160.

[71] A.W. McReynolds, Plastic deformation waves in aluminum, JOM 1(1) (1949) 32-45.

[72] N. Ranc, D. Wagner, Some aspects of Portevin–Le Chatelier plastic instabilities investigated by infrared pyrometry, Materials Science and Engineering: A 394(1-2) (2005) 87-95.

[73] S. Timothy, The structure of adiabatic shear bands in metals: a critical review, Acta Metallurgica 35(2) (1987) 301-306.

[74] T.A. Book, M.D. Sangid, Strain localization in Ti-6Al-4V Widmanstätten microstructures produced by additive manufacturing, Materials Characterization 122 (2016) 104-112.

[75] W. Chen, C. Li, K. Feng, Y. Lin, X. Zhang, C. Chen, K. Zhou, Strengthening of a near β-Ti alloy through β grain refinement and stress-induced α precipitation, Materials 13(19) (2020) 4255.

[76] Y. Cao, N. Li, Y. Luo, H. Tang, Q. Xie, A. Fu, A novel ultra-high strength titanium alloy via hierarchical α/α′ precipitation strengthening, Materials Science and Engineering: A 840 (2022) 142878.

[77] N. Chen, H. Kou, Z. Wu, F. Qiang, K. Hua, C. Wang, B. Tang, J. Li, J. Molina-Aldareguia, Design of metastable β-Ti alloys with enhanced mechanical properties by coupling αS precipitation strengthening and TRIP effect, Materials Science and Engineering: A 835 (2022) 142696.

[78] Z. Zhang, J. Fan, Z. Wu, D. Zhao, Q. Gao, Q. Wang, Z. Chen, B. Tang, H. Kou, J. Li, Precipitation behavior and strengthening-toughening mechanism of hot rolled sheet of Ti65 titanium alloy during aging process, Journal of Alloys and Compounds 831 (2020) 154786.

[79] X. Yao, Q. Sun, L. Xiao, J. Sun, Effect of Ti2Cu precipitates on mechanical behavior of Ti–2.5 Cu alloy subjected to different heat treatments, Journal of Alloys and Compounds 484(1-2) (2009) 196-202.

[80] A. Hayoune, D. Hamana, Structural evolution during non-isothermal ageing of a dilute Al–Cu alloy by dilatometric analysis, Journal of Alloys and Compounds 474(1-2) (2009) 118-123.

[81] J. Colmenero, K. Akune, Discontinuous precipitation in a Zn-1.6 wt.% Al alloy, Materials characterization 37(2-3) (1996) 123-130.

[82] J.F. Nie, Effects of precipitate shape and orientation on dispersion strengthening in magnesium alloys, Scripta Materialia 48(8) (2003) 1009-1015.

[83] K. Shitara, K. Yokota, M. Yoshiya, J. Umeda, K. Kondoh, First-principles design and experimental validation of β-Ti alloys with high solid-solution strengthening and low elasticities, Materials Science and Engineering: A 843 (2022) 143053.

[84] B. Sun, S. Li, H. Imai, T. Mimoto, J. Umeda, K. Kondoh, Fabrication of high-strength Ti materials by in-process solid solution strengthening of oxygen via P/M methods, Materials Science and Engineering: A

563 (2013) 95-100.

[85] H. Rosenberg, W. Nix, Solid solution strengthening in Ti-Al alloys, Metallurgical Transactions 4(5) (1973) 1333-1338.

[86] K. Yokota, A. Bahador, K. Shitara, J. Umeda, K. Kondoh, Mechanisms of tensile strengthening and oxygen solid solution in single β-phase Ti-35 at.% Ta+ O alloys, Materials Science and Engineering: A 802 (2021) 140677.

[87] S. Kariya, M. Fukuo, J. Umeda, K. Kondoh, Quantitative analysis on light elements solution strengthening in pure titanium sintered materials by Labusch model using experimental data, Materials Transactions 60(2) (2019) 263-268.

[88] M.J. Donachie, Titanium: a technical guide, ASM international2000.

[89] R. Ding, J. Gong, A.J. Wilkinson, I.P. Jones, A study of dislocation transmission through a grain boundary in hcp Ti–6Al using micro-cantilevers, Acta Materialia 103 (2016) 416-423.

[90] J. Kacher, B. Eftink, B. Cui, I. Robertson, Dislocation interactions with grain boundaries, Current Opinion in Solid State and Materials Science 18(4) (2014) 227-243.

[91] Z. Zhang, T.-S. Jun, T.B. Britton, F.P. Dunne, Determination of Ti-6242 α and β slip properties using micro-pillar test and computational crystal plasticity, Journal of the Mechanics and Physics of Solids 95 (2016) 393-410.

[92] Z. Shen, R. Wagoner, W. Clark, Dislocation pile-up and grain boundary interactions in 304 stainless steel, Scripta metallurgica 20(6) (1986) 921-926.

[93] J. Eshelby, F. Frank, F. Nabarro, XLI. The equilibrium of linear arrays of dislocations, The London, Edinburgh, and Dublin Philosophical Magazine and Journal of Science 42(327) (1951) 351-364.

[94] I. Basu, V. Ocelík, J.T. De Hosson, BCC-FCC interfacial effects on plasticity and strengthening mechanisms in high entropy alloys, Acta Materialia 157 (2018) 83-95.

[95] S. Rao, P. Hazzledine, Atomistic simulations of dislocation–interface interactions in the Cu-Ni multilayer system, Philosophical Magazine A 80(9) (2000) 2011-2040.

[96] D. Bufford, Z. Bi, Q. Jia, H. Wang, X. Zhang, Nanotwins and stacking faults in high-strength epitaxial Ag/Al multilayer films, Applied Physics Letters 101(22) (2012) 223112.

[97] Q. Zhou, P. Huang, M. Liu, F. Wang, K. Xu, T. Lu, Grain and interface boundaries governed strengthening mechanisms in metallic multilayers, Journal of Alloys and Compounds 698 (2017) 906-912.

[98] Y. Li, G. Zhang, W. Wang, J. Tan, S. Zhu, On interface strengthening ability in metallic multilayers, Scripta materialia 57(2) (2007) 117-120.

[99] C. Tan, Q. Sun, L. Xiao, Y. Zhao, J. Sun, Slip transmission behavior across α/β interface and strength prediction with a modified rule of mixtures in TC21 titanium alloy, Journal of Alloys and Compounds 724 (2017) 112-120.

[100] S. Berger, F. Spaepen, The Ag/Cu interface stress, Nanostructured Materials 6(1-4) (1995) 201-204.

[101] Z. Liu, Plastic deformation of Ti-6Al-4V micro-pillars at room temperature, University of Birmingham, 2017.

[102] M. Mills, D. Hou, S. Suri, G. Viswanathan, Boundaries and interfaces in materials, TMS, Warrendale, PA 295 (1998).

[103] R. Ding, J. Gong, A.J. Wilkinson, I.P. Jones, < c+ a> Dislocations in deformed Ti–6Al–4V micro-cantilevers, Acta Materialia 76 (2014) 127-134.

[104] R. Ding, Y. Chiu, I. Jones, N. Escalé, F. Pettinari-Sturmel, J. Douin, Application of a novel EBSD-FIB method to the transmission of c+ a dislocations through α/β interfaces Ti–6Al–4V for producing in situ tension transmission electron microscopy specimens, Journal of electron microscopy 61(1) (2011) 31-36.

[105] U. Dahmen, Orientation relationships in precipitation systems, Acta Metallurgica 30(1) (1982) 63-73.

[106] M.D. Uchic, P.A. Shade, D.M. Dimiduk, Plasticity of micrometer-scale single crystals in compression, Annual Review of Materials Research 39 (2009) 361-386.

[107] M.D. Uchic, P.A. Shade, D.M. Dimiduk, Micro-compression testing of fcc metals: A selected overview of experiments and simulations, Jom 61(3) (2009) 36-41.

[108] H. Wanzenboeck, H. Langfischer, A. Lugstein, E. Bertagnolli, U. Grabner, P. Pongratz, B. Basnar, J.

Smoliner, E. Gornik, Effects of Ga-irradiation on properties of materials processed by a focused ion beam (FIB), MRS Online Proceedings Library (OPL) 647 (2000).

[109] D. Hull, D.J. Bacon, Introduction to dislocations, Butterworth-Heinemann2001.

[110] J. Cairney, P. Munroe, Redeposition effects in transmission electron microscope specimens of FeAl–WC composites prepared using a focused ion beam, Micron 34(2) (2003) 97-107.

[111] B. Prenitzer, C. Urbanik-Shannon, L. Giannuzzi, S. Brown, R. Irwin, T. Shofner, F. Stevie, The correlation between ion beam/material interactions and practical FIB specimen preparation, Microscopy and Microanalysis 9(3) (2003) 216-236.

[112] K.A. Unocic, M.J. Mills, G. Daehn, Effect of gallium focused ion beam milling on preparation of aluminium thin foils, Journal of microscopy 240(3) (2010) 227-238.

[113] H. Ali, H. Ghadbeigi, K. Mumtaz, Effect of scanning strategies on residual stress and mechanical properties of Selective Laser Melted Ti6Al4V, Materials Science and Engineering: A 712 (2018) 175-187.

[114] T.A. Khraishi, H.M. Zbib, Free-surface effects in 3D dislocation dynamics: formulation and modeling, J. Eng. Mater. Technol. 124(3) (2002) 342-351.

[115] W. Zielinski, R. Keller, W.W. Gerberich, Heterogeneous dislocation loop nucleation and free surface effects on plastic deformation: an in situ transmission electron microscopy study, Fundamental Aspects of Dislocation Interactions, Elsevier1993, pp. 196-200.

[116] A. Kumar, U. Rabe, W. Arnold, Mapping of elastic stiffness in an α+ β titanium alloy using atomic force acoustic microscopy, Japanese Journal of Applied Physics 47(7S2) (2008) 6077.

[117] I. Sen, U. Ramamurty, Elastic modulus of Ti–6Al–4V–xB alloys with B up to 0.55 wt.%, Scripta materialia 62(1) (2010) 37-40.

[118] M. Ameen, R. Basheer, Plastic deformation of Ti-6Al-4V at small scale: a microstructural and mechanistic study, University of Birmingham, 2017.

[119] Y. Lee, M. Peters, G. Welsch, Elastic moduli and tensile and physical properties of heat-treated and quenched powder metallurgical Ti-6Al-4V alloy, Metallurgical Transactions A 22(3) (1991) 709-714.

[120] K. Luo, J. Lu, Q. Wang, M. Luo, H. Qi, J. Zhou, Residual stress distribution of Ti-6Al-4V alloy under different ns-LSP processing parameters, Applied surface science 285 (2013) 607-615.

[121] Z. Feng, Y. Yang, Z. Xu, Q. Shi, Effect of martensitic transformation on elastic modulus anisotropy of ti-6al-4v alloy, Materials Research 21 (2018).

[122] X. Chu, S.A. Barnett, Model of superlattice yield stress and hardness enhancements, Journal of Applied Physics 77(9) (1995) 4403-4411.

[123] R.G. Hoagland, R.J. Kurtz, C. Henager Jr, Slip resistance of interfaces and the strength of metallic multilayer composites, Scripta materialia 50(6) (2004) 775-779.

[124] J.G. Sevillano, I.O. Arizcorreta, L. Kubin, Intrinsic size effects in plasticity by dislocation glide, Materials Science and Engineering: A 309 (2001) 393-405.

[125] F. Frank, W. Read Jr, Multiplication processes for slow moving dislocations, Physical Review 79(4) (1950) 722.

[126] J.R. Greer, W.D. Nix, Size dependence of mechanical properties of gold at the sub-micron scale, Applied Physics A 80 (2005) 1625-1629.

[127] M.D. Uchic, D.M. Dimiduk, J.N. Florando, W.D. Nix, Exploring specimen size effects in plastic deformation of Ni3 (Al, Ta), MRS Online Proceedings Library (OPL) 753 (2002) BB1. 4.

[128] W. Shi, J. Shen, A. Muhammad, C. Wang, Y. Li, Dramatic strain rate sensitivity loss of the< a> prismatic slip in titanium from oxygen doping, Materials Science and Engineering: A 845 (2022) 143258.

[129] J. Wu, S. Lu, R. Chen, Y.-L. Chiu, In-situ deformation and the size-dependent yielding behaviour of Mg24Y5, Materials Science and Engineering: A 835 (2022) 142633.

[130] H. Zhang, B.E. Schuster, Q. Wei, K.T. Ramesh, The design of accurate micro-compression experiments, Scripta Materialia 54(2) (2006) 181-186.

[131] M. Haque, M. Saif, In-situ tensile testing of nano-scale specimens in SEM and TEM, Experimental mechanics 42 (2002) 123-128.

[132] P.J. Imrich, C. Kirchlechner, D. Kiener, G. Dehm, In situ TEM microcompression of single and

bicrystalline samples: insights and limitations, Jom 67 (2015) 1704-1712.

[133] Y. Bao, T. Wierzbicki, On fracture locus in the equivalent strain and stress triaxiality space, International Journal of Mechanical Sciences 46(1) (2004) 81-98.

[134] M. Dunand, D. Mohr, Hybrid experimental–numerical analysis of basic ductile fracture experiments for sheet metals, International journal of solids and structures 47(9) (2010) 1130-1143.